UNIVERSITÀ DEGLI STUDI DI PADOVA

Dipartimento di Fisica e Astronomia "Galileo Galilei"

Master Degree in Physics

Final Dissertation

A novel cosmic-ray neutron detector for soil moisture estimation over large areas

Thesis supervisor

Prof. Luca Stevanato

Thesis co-supervisor

Prof. Marcello Lunardon

Candidate

Luca Morselli

Academic Year 2018/2019

Contents

Abstract

Water scarcity and droughts problems in several parts of the world highlight the necessity of new solutions for better management of water resources. The prerequisite is reliable soil moisture data, measured over large-scales and in real-time. Due to this crucial role, many devices have been developed to measure soil moisture at different spatial and temporal scales. Available technologies range from point-scale invasive approaches as for instances Time Domain Reflectometry (TDR) probes to remote sensing approaches, like satellite remote methods. Nevertheless, practical problems arise when using these techniques: point-scale probe are invasive and their estimate difficult to scale up to field level, on the other hand, remote sensing exhibit unsuitable temporal resolution and, most importantly, they are sensitive only to a thin part of the soil and land surface. In the last decade, to overcome operational challenges of the aforementioned techniques, a proximal geophysical method has been developed, in order to fill the gap between point scale and remote sensing approaches: the Cosmic-ray Neutron Sensing (CRNS). CRNS is a valid and robust alternative, offering many advantages: it is contactless, allows quantification of soil moisture averaged over large areas with only one probe, and is not invasive for agricultural field operations. The significant advantages of the CRNS are its large horizontal footprint (up to tens of hectares) and the penetration depth of tens of centimeters, enough to reach typical roots depth. State-of-the-art probes used in CRNS are based on ^{3}He proportional counter tubes. ^{3}He is a nuclide produced almost entirely in artificial contexts as sub-product of the tritium decay, the current storage is depleting, and the price is high and rising, as it comes mainly from the production or dismantling of the nuclear weapons of the past decades. In the thesis, a new solution was studied. This new probe is based on a composite detector made of commercial scintillation detectors: EJ-276 and EJ-420(6) both manufactured by Eljen Technology (USA). In this kind of detectors, particles are identified and discriminated according to the generated signals, with an algorithm based on Pulse Shape Discrimination (PSD) which exploits the different processes activated by different particles interacting in the scintillator. PSD parameters were optimized with the aim of ensuring optimal discrimination capabilities. The readout is made of a flat panel photomultiplier H8500 from Hamamatsu, a fast digitizer DT5725 from CAEN, a low-cost, low-power, embedded computer Beaglebone black from Beagleboard and a low cost High Voltage power supply A7505 from CAEN. The digitizer is interfaced with the embedded computer, which hosts the acquisition and the analysis software. The online analysis software was developed as a distributed system where each task is handled by an independent server always running. Each server is implemented following the finite state machine pattern and communications between each of them are dispatched via TCP sockets. Finally, the probe was installed in a recent orchard with walnut trees for four months. Results showed that the reconstructed soil moisture is well correlated with precipitations, and it shows the limit of standard mea-

surement, that can be influenced by the heterogeneity of the soil and the irrigation distribution. Overall, the new probe uses non-toxic and non-carcinogenic plastic materials, easily recyclable and whose availability does not present scalability problems. Furthermore our probe, respect to ^{3}He tubes, offers more measured quantities, like gamma-rays and fast neutrons, which could provides useful information e.g. gamma-rays were found to be also correlated to soil moisture but with a smaller footprint.

In the first chapter, a brief review on soil moisture and biomass is given, highlighting their role in agriculture, hydrology and climate science together with the available estimation techniques. The second chapter deals with the cosmic-rays neutron sensing technique reviewing results from the literature.The third chapter deals with neutrons detection techniques giving a review of the well established experimental procedures. The fourth chapter shows the achieved results estimating soil moisture using a novel cosmic-ray neutron detector. The fifth chapter analyzes the upgrade of the latter probe and the achieved results.

Chapter 1

Introduction

1.1 The role of water sensing

Nowadays, water sensing is still a challenge in many applications. A precise knowledge of the soil moisture content and the knowledge of water storage in the biomass of plants is a fundamental prerequisite for many applications, from meteorological forecast to flood prediction, drought, agriculture and, in general, water accounting and management. Soil moisture is a small portion of the liquid water on Earth, it plays a crucial role in the hydrologic context. It represents a critical variable which regulates different processes within the climate system. Furthermore, the recent droughts in several parts of the world highlighted the necessity for new solutions for the careful use of water resources.

1.1.1 Water sensing in agriculture

FAO calculates that 70% of the employed water resources are dedicated to agriculture, on a global scale. Agriculture that maximizes the production of the crops with less waste of water is called precision agriculture, and two pillars of such agriculture are the precise knowledge of the soil moisture content and the knowledge of water storage in the biomass of plants. The water in the soil is essential for plants growth, whereas the biomass is a good indicator of the health of the vegetable organism. The continuous biomass monitoring on a daily basis can provide significant advantages in agriculture, but today is still a challenge. Such interest arises from the correlation typically found between the canopy size and plant needs in terms of water and nutrients as well as with the yield and quality. To highlight the importance of the biomass, we divide crops into two main categories:

- Annual intensive cultivations (such as cereals or oilseeds)

- Perennial crops (such as orchards or vineyards).

The plant growth for the first category is essentially linear during the spring/summer period and stabilizes during the last phases when the vegetation or the grain starts to dry and harvesting operations are carried out. The ratio between fresh biomass and dry matter is almost constant in the growing season. The measurement of the biomass trend allows the farmer to estimate the current nutritional needs, thus supporting the decision making process, in particular for the optimization of agrochemicals (treatments and fertilizers) in agreement with precision farming approaches [Lee and Ehsani, 2009]. In addition, the possibility of continuously measuring the biomass is of great importance in order to allow a continuous monitoring of the dry matter [Arnó, 2013, Rufat et al., 2014] and to allow forecast on final yields. The farmer can plan the company's work and answer the make-or-buy question if he knows the amount of yield in advance. He can buy earlier and at a lower price if the harvest forecast is not satisfactory. Finally, the biomass drop or missed growth following extreme weather events pests or diseases, provides an effective indication of the crop damage level. On perennial crops, as vineyards or orchards, the biomass might have a more irregular behavior. There are three main factors contributing to the overall growth of such parameter:

1. Wood, which has a very slow and linear growth and increases over the whole life of the plant;
2. Leaves, which continuously grow during the spring/summer period
3. Fruits, which starts growing after flowering with a maximum in correspondence of the harvesting time.

The estimation of leaf biomass at the beginning of the season is important to make pruning decision or to support plant treatments scheduling [Rosell and Sanz, 2012]. At the same time, a too rapid growth of the fruits biomass can allow the farmer to make a preventive fruit pruning to safeguard quality and comply with the production regulations, especially in the case of vines [Nuske et al., 2014]. As in case of annual intensive cultivations the measurement of the biomass trend for perennial crops allows the farmer to estimate the current nutritional need in particular for the optimization of agrochemicals treatments and fertilizers. This aspect is very important, especially for the vineyards, which treatments cost is very high compared to other crops.

1.1.2 Soil moisture in hydrology

Soil moisture is of fundamental importance in the hydrological context. As reported in [Brocca et al., 2017], soil moisture data can be helpful for improving the efficiency of certain applications such as drought monitoring, runoff modelling and flood risk. Moreover, soil moisture data can be used for calibrating mesoscale hydrological models.

Ideal candidate for such a task are data coming from Cosmic-Ray Neutron Sensing (CRNS) probes due to their ideal spatial footprint; recent studies have proposed the use of such data for the validation and calibration of hydrological models (See Figure 1.1).

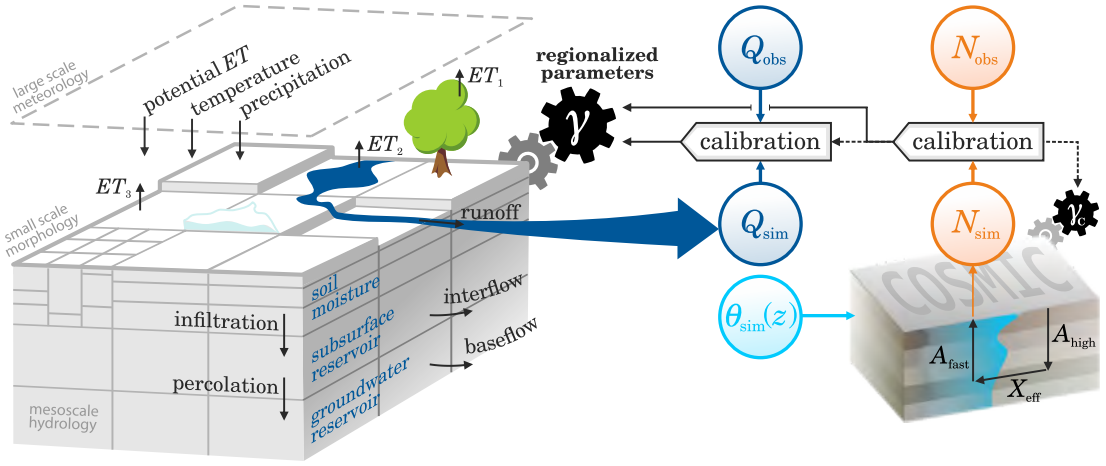

Figure 1.1: mHM mesoscale model and the proposed integration with CRNS data for simultaneous calibration. From [Schrön, 2017]

1.1.3 Soil moisture in climate science

As reported in different works soil moisture plays an active role in the balance between land energy and water via its coupling with evapotranspiration [Seneviratne et al., 2010]. The hydrologic balance (fig. 1.2) can be express based on the conservation of mass as:

$$\frac{dS}{dt} = P - E - R_g - R_s \tag{1.1}$$

where dS/dt is the absolute water change in time, P is the precipitation, R_s is the surface runoff and R_g the ground runoff. The land energy cycle (fig. 1.3) is express as:

$$\frac{dH}{dt} = R_n - \lambda E - SH - G \tag{1.2}$$

where dH/dt is the change of energy within the sample layer, R_n is the net radiation[1], λE is the latent heat flux, SH is the sensible heat flux and G is the ground heat flux to deeper layer. From equation 1.1 and 1.2 can be seen the coupling between energy and water cycle through the evapotranspiration terms (E, λE).

[1]The net radiation is usually defined as: $R_n = SW_{in} - SW_{out} + LW_{in} - LW_{out}$

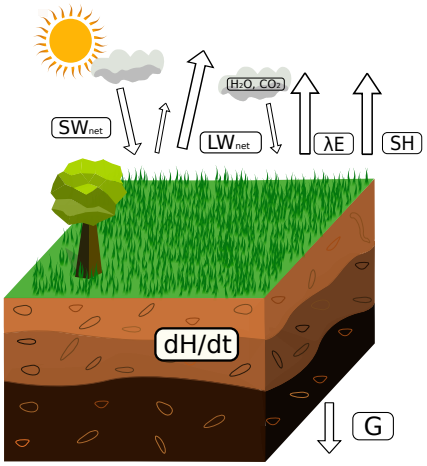

Figure 1.2: Energy cycle.

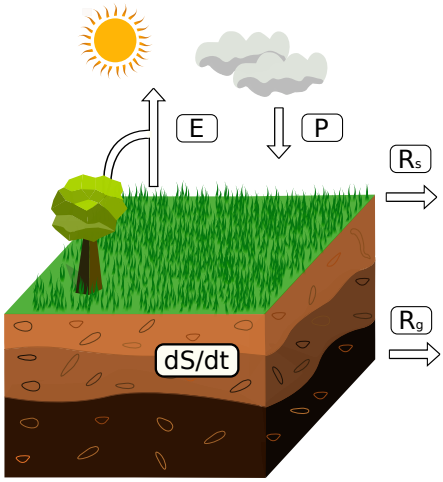

Figure 1.3: Water cycle.

1.2 Definitions

The definition of soil moisture varies according to the different fields of studies, but generally, we can define it as the water contained in the unsaturated soil component and is usually expressed as mass or volume ratios [Hillel, 1998]. The **volumetric soil moisture** is defined as:

$$\theta = \frac{V_w}{V_t} = \frac{V_w}{V_a + V_s + V_w} \tag{1.3}$$

where V_t is the sum of the sample volume i.e. the air (V_a), the water (V_w) and the soil (V_s) ones. The **gravimetric soil moisture** instead:

$$\theta_g = \frac{m_w}{m} \tag{1.4}$$

where m_w is the water mass and m is the sample mass. These two definition are linked by the following relation:

$$\theta = \theta_g \cdot SG \tag{1.5}$$

where SG is the **specific gravity** which is defined as:

$$SG = \frac{\rho_{sample}}{\rho_{H_2O}} \tag{1.6}$$

Since the maximum amount of water within a given soil volume is upper bounded (i.e. porosity of the soil matrix), it can be useful to express it relative to the saturation soil

moisture value:

$$\theta_s = \frac{\theta}{\theta_{SAT}} \tag{1.7}$$

where θ_s varying between 0 (no water) and 1 (saturated soil).

Another possibility is that of expressing soil moisture in absolute term:

$$S = \theta \cdot d \tag{1.8}$$

where d is the considered soil depth.

1.3 Soil Moisture Estimation methods

The importance of soil moisture in these contexts has triggered the development of different methods for estimating it [Verstraeten et al., 2008,Robinson et al., 2008,Petropoulos, 2013]. The estimation of the soil moisture is, however, a challenging task due to its high spatial and temporal variability [Famiglietti et al., 2008]; furthermore, there are non linear processes which depends on it. This highly variable behaviour introduces a scaling problem when using soil moisture data to predict a system at a different scale. As reported in [Western et al., 2002], the scale properties of measurement are associated with a triplet of characteristics (see Fig. 1.4): support, spacing and extent.

The support (also called footprint) is the area over which a measurement averages the underlying variation, indeed, when support increases the averaging act as low-pass filter ruling out small-scale variations. Spacing is, as the name suggests, the distance between different measurements points. Increasing spacing leads to an up-sampling that highlight small-scale patterns; on the other hand, reducing it, lead to a down-sample highlighting only larger-scale patterns. The last one is the extent which refers to the total coverage of the measurements, increasing it leads to larger-scale features and both the variability and the average size of the features tend to increase. When using different estimation methods, this triplet has to be considered to distil the underlying soil moisture amount successfully. There are three main classes of estimation methods: ground-based, remote sensing, and proximal geophysical methods; in Fig 1.5 each method is plotted showing its footprint, and the maximum reached depth.

1.3.1 Ground-based methods

Regarding the triplet described above, these methods share low support characteristics (from 1cm to 10 cm), which is a problem when covering large areas. In fact, in order to reach a reasonable extent using low support probe, a large number of sensors have to be employed. The needed probe number scales quickly due to spacing constraint needed to

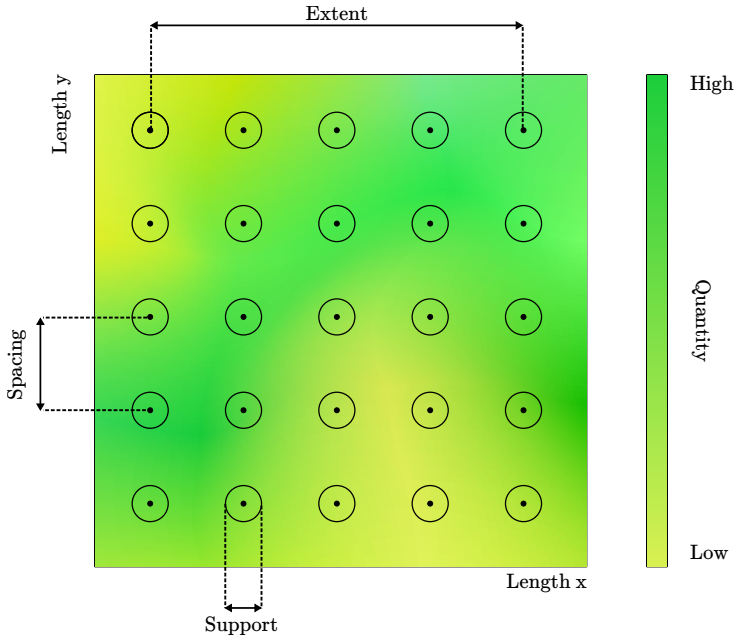

Figure 1.4: Scale triplet visualized. The underlying colours represent the value of a 2D function which represents the quantity of interest.

avoid misinterpretation of hydrological scenarios caused by soil heterogeneity. On the other hand, this class of techniques has a good temporal resolution which allows routine monitoring at different points. Moreover, can estimates soil moisture at different depths, suitable for hydrology applications, with respect to remote sensing.

Gravimetric Methods

A soil sample is left to dry and sieved using fine-grained, and weigh, then is oven-dry at 105°C and reweigh. The difference in weight represents the water content of the original sample. Moreover, this method is also lithology dependent which means that soil bulk densities are required to convert between gravimetric and volumetric soil moisture. Usually, this method is used as a starting point to validate indirect measurements.

Methods based on the dielectric constant

Due to its molecular structure, water has a high permanent dipole moment with respect to soil ($\sim$5) and air ($\sim$1). Thus the amount of water in the non-saturated zone acts on the soil bulk permittivity. Debye showed that composite materials showed a frequency dependence, which is the foundations of these sensors. Through calibration against gravimetric measurements is possible to retrieve the soil moisture information.

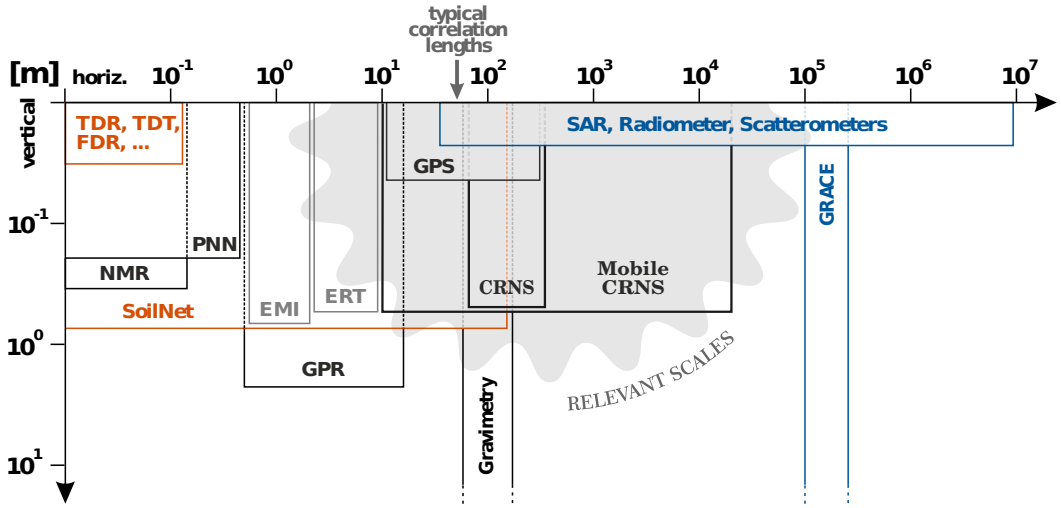

Figure 1.5: Scales of soil moisture measurement covering invasive (brown), non-invasive (black), and remote-sensing(blue) methods. Credit: [Schrön, 2017].

Most widely used methods exploiting this phenomenon are capacitive and reflectometry probes. Capacitive probes measure the capacitance between two electrodes inserted in the soil (usually rings). By measuring the capacitance of the media between the two electrodes is possible to retrieve the soil moisture content [Harris and Stonard, 2018]. An example of reflectometry probe is the time-domain reflectometer (TDR) which determines the dielectric constantly measuring the propagation time of electromagnetic waves, sent from a pulse generator of a cable tester immersed in the soil matrix. Electromagnetic waves propagate through a coaxial cable to a TDR probe, which is usually a rod, made of stainless steel or brass. Part of an incident electromagnetic wave is reflected at the beginning of the probe because of the impedance difference between the cable and the probe. The remainder of the wave propagates through the probe until it reaches the end of the probe, where the wave is reflected. A sampling oscilloscope can measure the round-trip time of the wave, from the beginning to the end of the probe on the cable tester [Noborio, 2001]. In addition to the disadvantages presented by other methods, the detectors are invasive (burred in the soil or snow), and they require high maintenance making them not suitable for covering heterogeneous and impervious sites (mountains and cropped fields) and for long-term monitoring observatories.

Nuclear methods

There are three main methods which exploit nuclear properties in order to estimates soil moisture: gamma-ray attenuation, neutron scattering and nuclear magnetic resonance.

The idea of using gamma-ray in order to estimate soil moisture is rather old [Reginato and Van Bavel, 1964]. When photons interact with matter, the attenuation factor is related to the density of the material. One possible detector geometry consists of two cylinders: one is provided with the radioactive source, and the other is instrumented with a detector measuring primary photons. Although this method provides, non-destructive, average measurement of the water content of the examined profile the permanent presence of an active source make this method difficult to apply due to potential radiation hazard.

1.3.2 Remote sensing

Compared with point scale methods, satellite remote sensing provides soil moisture observations globally and at larger footprints, so it is more suitable for hydrological usages [Zhuo and Han, 2016]. Temporal resolution (e.g., weekly) is however not always ideal for many applications and, more important, they are sensitive only to a thin part of the soil and land surface (few centimeters) [Petropoulos et al., 2015]. Furthermore, their accuracy varies across time and meteorological conditions (e.g., wind speed, air temperature and humidity). Large-scale satellite remote sensing methods have other limitations [Entekhabi et al., 2004], including the limited capability to penetrate vegetation or snow, inability to measure soil ice, sensitivity to surface roughness and short life span of satellite missions.

1.3.3 Proximal geophysical methods

In the last decade, several proximal geophysical methods have been developed to try to fill the gap between point scale and remote sensing approaches. These techniques allow for continuous non-invasive and contactless measurements of soil moisture dynamics at the field to basin-scale [Bogena et al., 2015] filling the gap between point-scale and remote sensing estimation (Fig . 1.6). Remarkably, two approaches emerged. The first approach is based on gamma-ray spectrometer [Loijens, 1980]. This detector has been used for snow measurements [Smith, 2017] and soil mapping [Rossel, 2007] in many applications. More recently, it shows also promising applications for soil moisture detection in cropped fields [Baldoncini, 2019, 2018]. Its developing is still however at the beginning and no specific detectors, electronics and software have been designed for this particular application. The second approach is based on the detection of environmental slow neutrons; its acronym is Cosmic Ray Neutron Sensing (CRNS). Since it is the

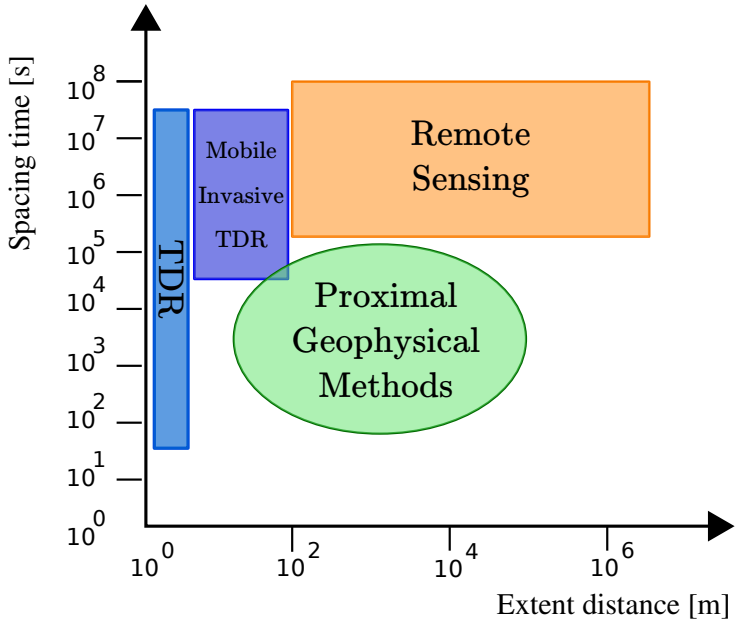

Figure 1.6: Spatial and temporal characteristics of current detectors for soil moisture measurements. Adapted from [Robinson et al., 2008]

estimation methods used in this work its operation will be the subject of the next chapter.

1.4 Biomass estimation methods

Currently there are many methods to estimate the biomass; they take advantage of the availability of miniaturized low cost sensors and of an increased speed in data processing [Arnó, 2013, Marinello et al., 2014, Pajares et al., 2013]. Available technologies can be referred mainly to ultrasonic and laser sensors [Su and Zhang, 2010]. Ultrasonic technology is a low cost solution [Palleja and Landers, 2017] but its performance is influenced by ultrasound propagation, which often exhibits parasitic signals or losses especially in the cases of thin targets or high reflection angles as in the case of small branches or in the case of badly oriented leaves. Laser based techniques include an interesting group of sensors, which take advantage of coherent light sources shined into the scene, its main limitations are ascribable to distortions and noise mainly caused by sunlight exposure and to high computational complexity [Marinello et al., 2014, Su and Zhang, 2010]. Recently new optical methods are under development [Marinello et al., 2017], but they suffer from shadows created by the leaves. As will be shown in the next chapter Cosmic-Rays Neutron Sensing can be used in order to retrieve information on biomass dynamics at field scale allowing for a simultaneous monitoring of both soil moisture and above ground biomass with a single probe.

Chapter 2

Cosmic Rays Neutron Sensing

Cosmic-rays neutrons sensing is a recent proximal geophysical methods firstly introduced by [Zreda et al., 2008] and [Desilets et al., 2010]. This method allows for a field-scale estimation of hydrogen pools e.g. soil water content, aboveground biomass and snow water equivalent thorugh the measurement of epithermal neutrons intensity above ground. These epithermal neutrons are the product of primary cosmic rays interaction with the atmosphere. In this Chapter a brief review of the technique is given highlighting the underlying physical processes behind it and its footprint (both vertical and horizontal).

2.1 The discovery of cosmic rays

At the beginning of the 20th century, one of the open questions was to discover which was the source of air ionization (refer to [Dorman and Dorman, 2014] for a more exhaustive report). This question arises after an experiment by Coulomb in 1785, which showed that a charged metallic sphere left alone in the air gradually loses its charge. After the discovery of natural radioactivity, physicists thought that all ionization of atmospheric air was caused by sources of radioactive origin below the ground. Since the alpha and beta radiation are rapidly absorbed in the air, gamma radiation was the favourite candidate as the ionization source. Between 1911 and 1912 Heiss, with the aim of study the height at which gamma radiation propagates from the ground level, took several flights on ballons which led to the observation of increasing ionization rates with increasing altitude. Heiss reported that between 4 and 5 km, the ionization rate became much higher than at sea level, concluding that the source of ionization might be of extraterrestrial origin. These results were confirmed in 1913-1914 by Kolhörster, who reached altitudes of 9 km, where the ionization rate was even higher. In the early 20s, Millikan proposed the name cosmic rays driven by some erroneous interpretation of his measurements on

the ionization at different height due to this new radiation. Further studies carried out by J. Clay had found evidence that cosmic rays intensity increase with longitude, pointing out that the geomagnetic field deflects particles from cosmic rays. In the 1930 B. Rossi predicted a difference between the intensities of cosmic rays arriving from different latitudes, the "east-west effect", further studies confirmed that primary cosmic rays particles are mainly protons and α while electrons, muons and photons are produced by secondary radiation.

2.2 Flux spectrum and composition

By looking at the primary cosmic-ray particles spectrum is possible to retrieve useful information about their behaviour (Fig.2.1). The spectrum is more or less featureless following a constant power law:

$$\frac{dN}{dE} \propto E^{-\beta} \tag{2.1}$$

which holds across a wide energy range that spans 13 decades, corresponding to a decreasing in intensity over more than 30 decades. An essential characteristic of the flux spectrum is that became steeper at energy near 10^{15} eV, this region where the exponent change from -2.7 to -3.1 is called the *knee*. There is evidence that the chemical composition of CRs changes across the knee region with a trend to become increasingly more dominated by heavy nuclei at high energy. This change in composition added to the presence of a knee have led to the idea that bulk CRs are indeed produced within our Galaxy [Blasi, 2014].

The presence of a knee and the change of chemical composition around it have stimulated the idea that the bulk of CRs originates within our Galaxy. The knee could, for instance, result from the superposition of cutoffs in the spectra of the different chemicals as due to the fact that most acceleration processes are rigidity dependent [Blasi, 2013]. The other important feature of the spectra is the so-called ankle at ultra high energy (10^{19} eV) where the slope change to -2.8 the authors suggest that this feature signals the transition from Galactic to extra-galactic CRs.

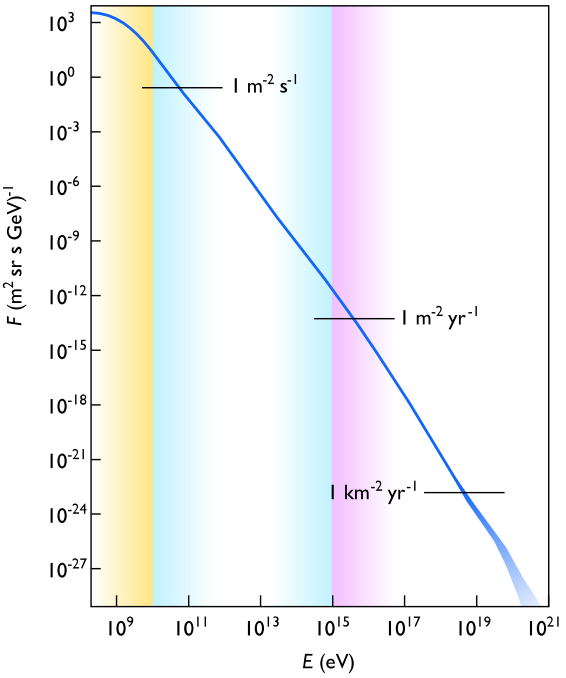

Figure 2.1: Cosmic flux versus particle energy. From https://en.wikipedia.org/wiki/Cosmic_ray

2.3 Cosmic rays sources and propagation

Recent experiments point out different possible sources of cosmic rays: supernova remnants, gamma-ray burst and active galactic nuclei (AGN). To explain the observed spectrum, different models of particles acceleration were proposed: the first idea of a possible acceleration mechanism is due to Enrico Fermi, which proposed a model in which particles gains energy through interaction with interstellar clouds (Figure 2.2).

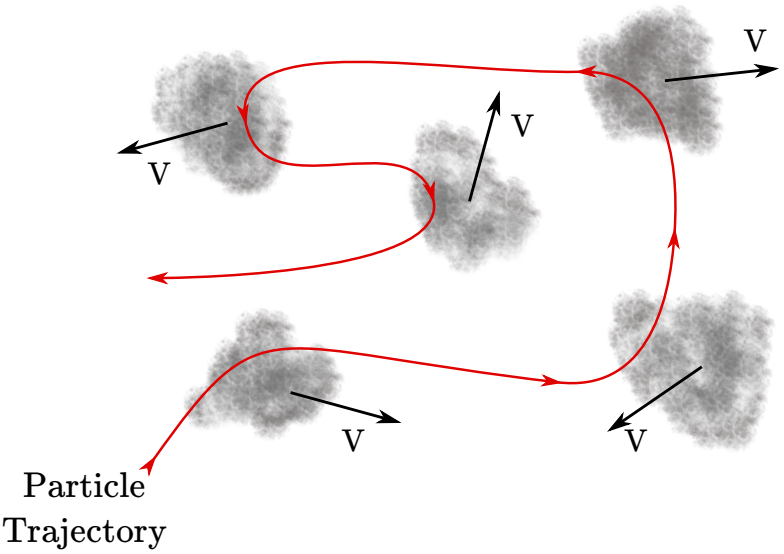

Figure 2.2: Interaction between charged particle and interstellar clouds.

Fermi found that the average increase in energy during a collision averaged over all angles is proportional to the square of β. The fundamental aspect here is that the energy of the particle may increase or decrease depending on whether the reaction was head-on or tail-on. The fact that there is a mean energy increase is because head-on collision are more likely with respect to trailing collisions. Nevertheless, random clouds velocities are rather small ($\beta \leq 10^{-4}$) and together with the fact that the fractional energy increase is a second order function of β makes this model unable to explain the high acceleration mechanics. Moreover, the mean free path for the scattering of cosmic rays in the interstellar medium is of the order of 0.1 parsec and so the number of collisions would amount to about a few per year, resulting in a very slow gain of energy by the particles [Longair, 2011]. In order to overcome these issues a new model, based on the so-called *diffusive shock acceleration*, was proposed. The idea is a speed decrease between the shocked medium and the unshocked one, thus, from each side of the shock the other is moving towards it. Thus, unlike the *second-order* Fermi acceleration, all

collisions are head-on resulting in a gain of energy. For a complete cycle from upstream to downstream the shock there is an energy gain which is in average a first order function of β [Longair, 2011]. When the particle reach a sufficient amount of energy it can leave the local structure.

Inside the interstellar medium, cosmic rays undergo different processes, furthermore charged magnetic fields also influence charged particles trajectories, the aftermath of the various process can be modeled as a random walk regulated by diffusion. Simulations show that this diffusion process is almost isotropic on the scale of the Milky-way; the incoming radiation is almost uniform and isotropic with variations of less than 0.1%.

When approaching the solar system, charged cosmic rays particles have to overcome the magnetic field that is carried by the solar wind. At distances of ∼94 AU from the Sun, the solar wind undergoes a transition, called the termination shocks, from supersonic to subsonic speeds. The region between the termination shock and the heliopause acts as a barrier to cosmic rays, decreasing the flux at lower energies (<1 GeV) by about 90%. Furthermore, since solar activity is not constant over time, the cosmic flux is correlated with it. This modulation carried by the solar activity was first observed as an anti-correlation of the neutron monitors data with the sunspot numbers on the Sun 2.3), which measures the number of active regions on the Sun, has roughly an 11-year cycle, 1/2 of the magnetic cycle on the Sun. Recent theoretical models found that the solar wind causes significant decreases on incoming galactic cosmic ray flux at≈1 AU in accordance with the observed anti-correlation.

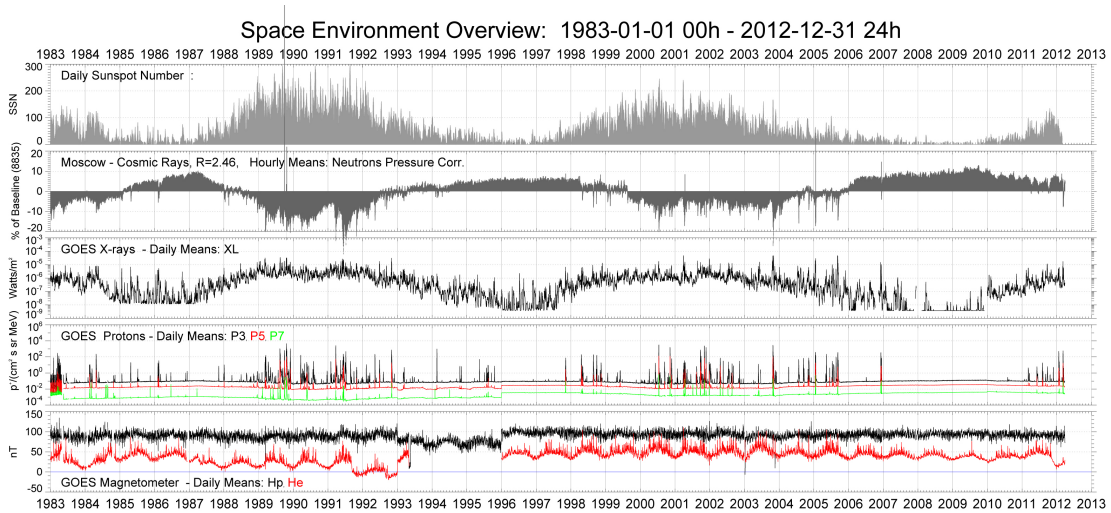

Figure 2.3: Anti-correlation between solar sunspot and cosmic rays neutrons.

When primary cosmic rays reach the Earth are spread slightly anisotropically by the geomagnetic field which lead to the previously mentioned East-West effect. Primary cosmic-rays are charged particles then are subject to the Lorentz force which can lead to a rejection since this force strongly depends on the angle between the particles velocity and the local magnetic fields. This can explain why Cosmic-Rays are more abundant at lower latitudes: due to the geomagnetic field dipole structure at the poles (low latitudes) the angle between the magnetic field and the particle velocity is zero and then the rejection force is null. Particles below a certain threshold in the rigidity, R_{cut} namely *cutoff rigidity*, are rejected, in Fig.2.5 is shown a map of calculated cutoff rigidities). This modulation is constantly measured using neutrons monitor networks spreaded around the Earth surface. These integral detectors are able to measure secondary cosmic-rays particles, mainly neutrons. For a neutron monitor placed at cutoff rigidity R_{cut} the measured intensity is given by [Krüger et al., 2008]:

$$N(R > R_{cut}) = \int_{R_{cut}}^{\infty} \frac{dN}{dR} dR \tag{2.2}$$

where $R = \frac{m\vec{v}}{q\vec{B}}$ is the magnetic rigidity and $\frac{dN}{dR}$ is called *differential response function* which is related to the primary cosmic rays intensity above the atmosphere $j(R,t)$ and the yield $S(R,x)$ of secondary cosmic-rays at a given depth x, through:

$$-\frac{dN}{dR} = S(R,x)j(R,t) \tag{2.3}$$

Subsequent studies on the estimation of this function have led to an approximation of it that relates the incident neutrons based on their vertical cutoff on rigidity [Schrön, 2017] (Fig.2.4):

$$N = N_0 \left(1 - e^{-\alpha R_{cut}^{-k}}\right) \qquad \alpha \approx 9.021 \quad k \approx 1.05 \quad N_0 \approx 5.17 \cdot 10^4 cph \tag{2.4}$$

where the parameters are calculated by fitting the curve against neutron monitor data.This account for the intensity reduction below 50% at the equator ($R_{cut} > 10GV$).

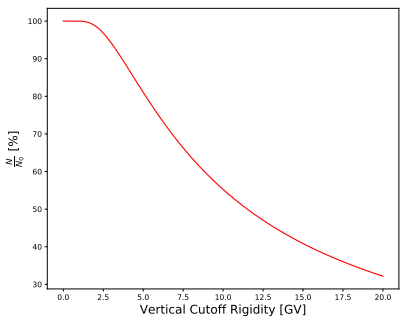

Figure 2.4: Neutrons monitors expected intensity as a function of vertical cutoff rigidity.

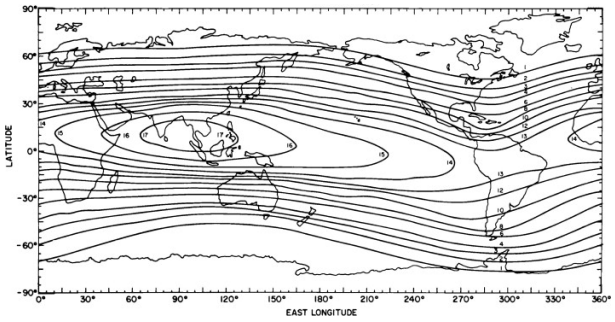

Figure 2.5: Map of cutoff rigidities calculated for January 2016. From [Schrön, 2017].

2.4 Reactions in the atmosphere

Once in the upper part the atmosphere, protons interact with atomic nuclei (mainly nitrogen and oxygen) producing secondary cosmic-rays particles by electromagnetic and nuclear interactions. These secondary particles reach their intensity peak at 50-100 g/cm^2 atmospheric depth (called Pfotzer depth). In [Sato and Niita, 2006], using Monte Carlo simulations found that neutron spectra below 15 MeV is almost independent on global conditions, i.e. cutoff rigidities and atmospheric depths for all neutrons below Pfotzer depth. In Figure 2.6 the neutron spectra at ground level is plotted in which

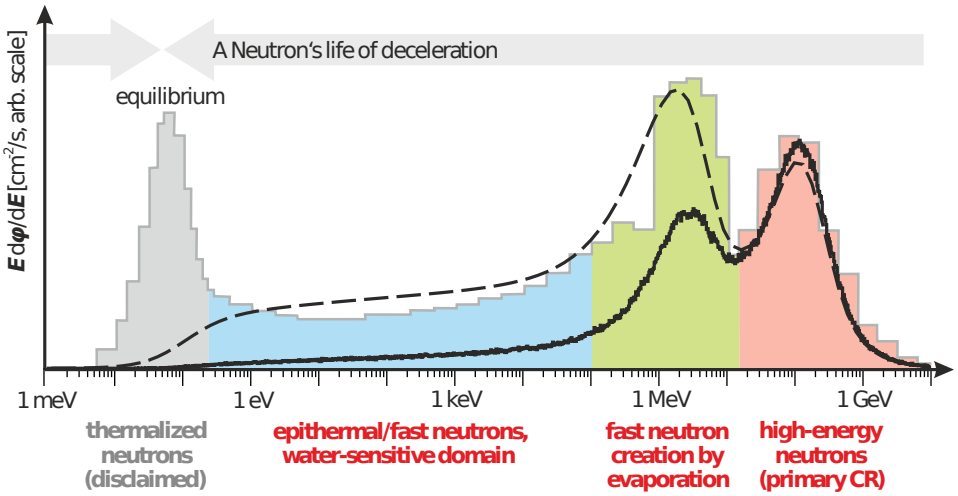

Figure 2.6: Neutron energy spectra at the Earth surface. From [Köhli et al., 2015]

three peaks emerge:

- Between 100 and 200 MeV (red area) there are high-energy neutrons produced mainly by intranuclear cascades and pre-equilibrium processes.
- Between 1-10 MeV (green area) there is the fast neutrons peak produced by evaporation processes of excited nuclei.
- At 0.025 eV (grey area) there are neutrons which have reached the thermal equilibrium.

Between 0.025 eV and 1 MeV, there is the so-called epithermal neutron region which contains neutrons that have undergone different collisions but that have not yet reached the thermal equilibrium. The black dashed line in Figure 2.6 is the simulated spectra obtained by [Sato and Niita, 2006]. The black line, instead is obtained by subtracting the ground reflected component over pure water.

2.5 Neutrons interactions with matter

Neutrons can interact only through strong nuclear force between them and the target atomic nucleus of the absorber material, which results in the particle deviation through elastic or inelastic scattering. Another interaction that neutrons can undergo is the capture process which results in a secondary radiation emission; this reaction mechanics is often the core idea behind thermal neutrons detection. Interaction type probability is strongly dependent on the energy of the neutrons, for thermal/slow neutrons capture processes are dominant while when increasing the energy scattering processes become more and more probable.

2.5.1 Neutron moderation

Neutrons can be moderated through elastic scattering processes with other elements. This is the process on which CRNS is based upon. Let's analyze the elastic scattering processes of a nucleus with atomic mass A with a neutron:

$$n + {}^{A}_{Z}X \longrightarrow n + {}^{A}_{Z}X \tag{2.5}$$

moreover, by imposing the conservation of quadri-impulse is possible to retrieve the energy in the final state, E_f, as a function of the scattering angle, θ, which is the angle between the neutron direction and the diffusion angle:

$$E_f(\theta) = E_i \cdot \frac{4A}{(1+A)^2} \cos^2\theta \tag{2.6}$$

The maximum energy transfer is when the target nucleus is scattered at $\theta = 0$. Since hydrogen is the lightest atom it allows for the maximum energy transfer, in general, the more the absorber material is light, the more neutrons are moderated. In Figure 2.7 it is plotted the neutron elastic scattering cross-section for different target nuclei showing the dependence on the energy and the atomic number of target nuclei. As an example, a fast neutron requires on average only 26 collisions with hydrogen nuclei to decrease its energy from 2 MeV (fast neutron) to 0.025 eV (thermal neutron), compared to other common elements such as Carbon (119 collisions), Oxygen (155 collisions), Nitrogen (137 collisions). Due to this, hydrogen in water molecules becomes the dominant factor for moderating fast neutron. Before being thermalized, fast neutrons travel through the soil-air continuum creating an equilibrium concentration which depends on two factors:

- Production rate of fast neutrons.
- Soil stopping power, which is dominated by hydrogen content of soil.

This equilibrium is shifted in response to changes in the water present above and below

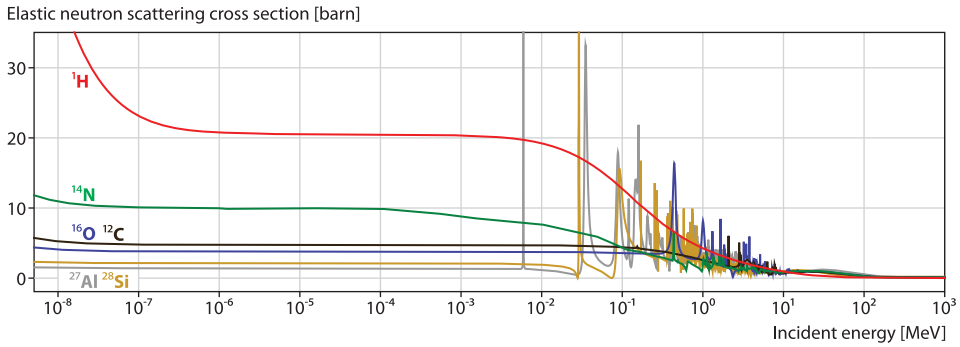

Figure 2.7: Neutron elastic scattering cross-section for different target nuclei. From [Köhli et al., 2015]

the land surface. For example, a drier soil, having a lower moderation capacity, reflects a greater number of neutrons, unlike a wetter soil, which absorbs them more easily, thus increasing the slow component of the spectrum. As shown in [Köhli et al., 2015], the ground response to the incoming flux of neutrons produced by cosmic-rays is energy-dependent. In the two plots of Figure 2.8 it can be seen how different parts of the spectrum react in response to changes in the soil water content. From these two plots is clearly visible that the epithermal region is the most sensible part of the spectrum to soil moisture variations. Exploiting the inverse proportionality between epithermal neutrons flux above ground level and soil moisture is the key concept of CRNS.

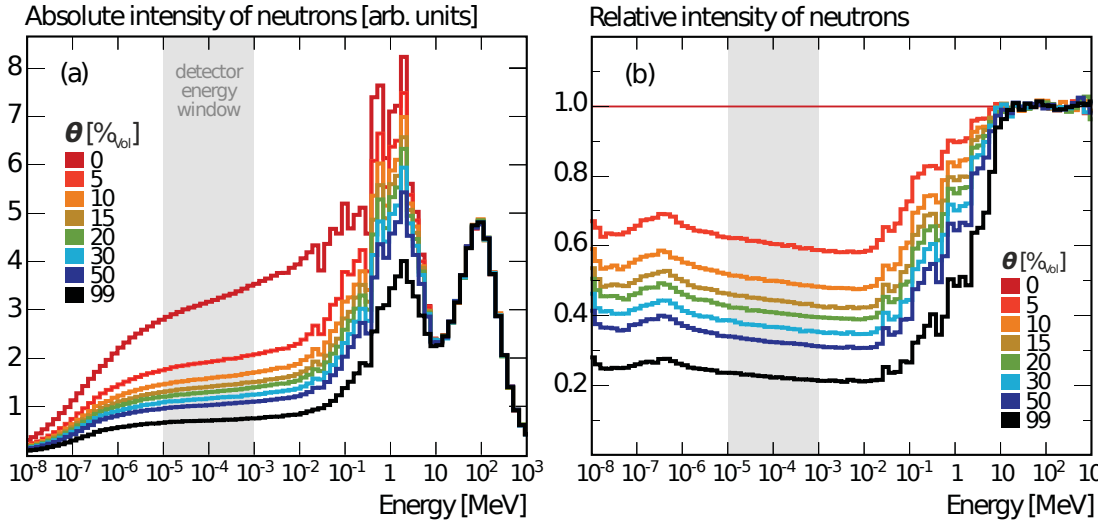

Figure 2.8: Calculated neutron spectra above ground with ^{3}He proportional counter detection energy window. From [Köhli et al., 2015]

2.5.2 Other processes

Neutrons may undergo other types of processes. Below, there is a brief review of the key aspect of each of them.

Neutron Capture

In these reactions, the incident neutron is absorbed by the atomic nuclei. The aftermath of the absorption is secondary radiation emission which is usually a charged particle which can be detected. This is the reaction that proportional counters exploit for detecting neutrons and/or gamma-rays.

Unelastic scattering

For high-energy neutrons inelastic scattering can take place yielding the recoil nucleus in an excited state which de-excite quickly emitting a gamma-ray. With respect to the elastic scattering the incoming neutrons loses a larger fraction of its energy. This phenomena is fundamental in the shielding of neutrons with high-energy, on the other hand, this lead to complication in fast neutron detectors response which relies on elastic scattering [Knoll, 2010].

Spallation

This is the analogue to the proton-induced spallation. High-energy neutrons can break a target nucleus in different fragments, but this reaction is relevant only for neutrons with energies higher than 100 MeV.

2.6 Atmospheric variations

Since CRNS wants to exploit the inverse proportionality between neutrons flux above land surface and soil water content, it is of fundamental importance to rule out all the possible effects which might influence this observable but which are not dependent on soil moisture. There are three factors which dominate among the others:

1. Air pressure, p.
2. Variations of incoming cosmic rays in the upper part of the atmosphere, I.
3. Air humidity, h.

each of them is associated with a **correction function**: C_h, C_p, C_I, respectively, which is used in order to correct the neutron signal from CRNS probes as follow:

$$N = N_{\text{raw}} \cdot C_h \cdot C_p \cdot C_I \tag{2.7}$$

2.6.1 Air pressure

Since incoming neutrons are moderated by air molecules the number of neutrons that reach the Earth surface changes when air mass changes. As shown in Figure 2.9 cosmic-rays neutrons intensity is inverse correlated with air pressure.Thus, air pressure can be used as a proxy for this mass change leading to the following correction function:

$$C_p = e^{\beta(p-p_{ref})} \quad p_{ref} = 1013.25 \text{ hPa} \qquad \text{at sea level.} \tag{2.8}$$

where β is the barometric attenuation coefficient which is inverse proportional to the attenuation length.

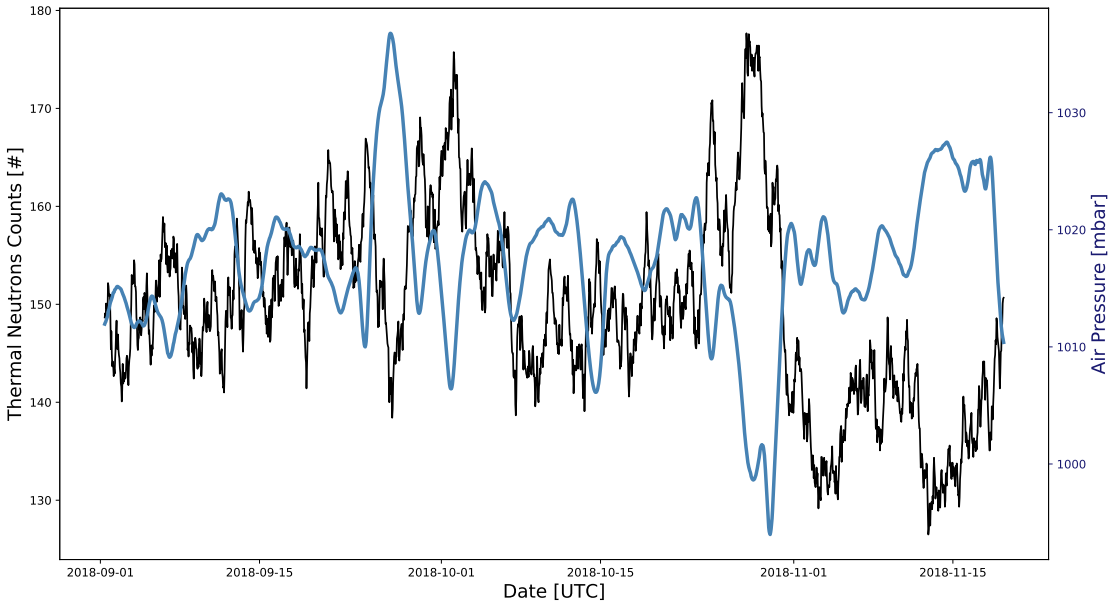

Figure 2.9: Data showing the anti-correlation between air pressure and thermal neutrons counts. Data are from the experimental campaign described in Chapter 4.

2.6.2 Primary cosmic-rays incoming

As stated above primary cosmic-rays incoming is not constant but shows dependence on solar activity and other temporal effects which need to be ruled out. The most widely used correction function was proposed in [Zreda et al., 2012] exploiting neutron monitors data as a proxy for the primary incoming fluctuations:

$$C_I = \frac{I_{\text{ref}}}{I} \tag{2.9}$$

This simple approach, nevertheless, is not able to correct all cosmic-ray variability as can be seen in Figure 2.10 where residual features of the incoming radiation are still present in the corrected signal.

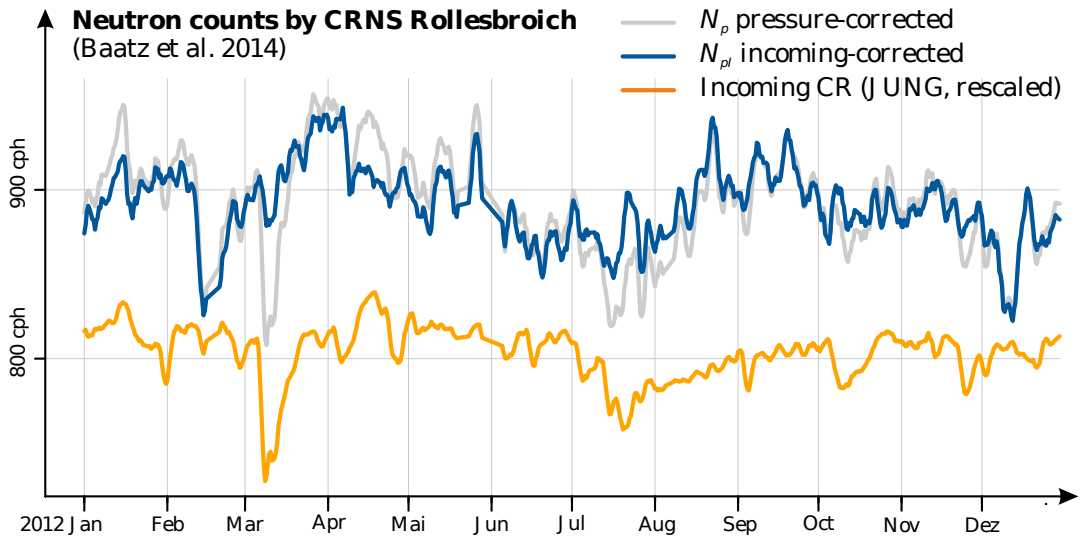

Figure 2.10: Remaining features after cosmic-rays correction. From [Schrön, 2017].

A more general form for the correction function is given by:

$$C_I = 1 + \gamma \left(\frac{I_{ref}}{I} - 1 \right) \tag{2.10}$$

where γ regulates the scaling of primary cosmic-rays variation. Recent studies have tried to account for geomagnetic rigidity effects but results are still preliminary, thus, is widely accepted to use $\gamma = 1$.

2.6.3 Atmospheric water vapor

This correction is small but, as described in Section 2.7 is relevant for neutrons far away from the probe. The fast neutron sensitivity on atmospheric water vapor was first studied in [Rosolem et al., 2013] which proposed the following correction function:

$$C_h = 1 + \alpha(h - h_{ref}) \qquad \alpha = 0.0054, \quad h_{ref} \equiv h(50\%, 25°C) = 12\text{g/cm}^3 \tag{2.11}$$

2.6.4 Estimating soil moisture

The CRNS probe above ground will receive two main signal components:

- Neutrons which have not interacted with the soil.
- Neutrons scattered from the soil and air.

which can be written as:

$$N_d = a_{\text{incoming}} \cdot N_0 + a_{\text{reflected}}(\theta) \cdot N_0 \tag{2.12}$$

where N_0 is a calibration parameter which represent the neutron counting in dry soil condition. As reported in [Schrön, 2017] the result from [Desilets et al., 2010] can be interpreted as an inverse relation between the reflected neutrons and gravimetric soil moisture:

$$a_{\text{reflected}} \equiv \frac{a_0}{a_2 + \theta_g} \ , \ a_{\text{incoming}} = a_1 \tag{2.13}$$

which gives:

$$\theta_g(N) = \frac{a_0}{\frac{N_d}{N_0} - a_1} - a_2 \tag{2.14}$$

where a_1, a_2, a_3 are used as fitting parameters. Parameters value were obtained by fitting the function against simulated neutrons fluxes at ground level. For a generic silica soil matrix the following parameters were obtained [Desilets et al., 2010]:

$$\begin{cases} a_0 = 0.0808 \\ a_1 = 0.372 \\ a_2 = 0.115 \end{cases}$$

2.7 CRNS Footprint

Footprint refers to the area in which it is possible to obtain information about a given observable with a given geophysical instrument. In this section is presented a brief summary of the results obtained in [Köhli et al., 2015] aimed to a precise characterization of such footprint through sophisticated Monte Carlo simulation using URANOS software [Köhli et al., 2018].

In air fast neutrons can travel tens of meters between each collision forming a well-mixed reservoir of neutrons [Desilets et al., 2010]. Since the interaction cross-section is almost isotropic the neutrons diffuse through a random walk process, therefore, our detector will receive signals isotropically within a circular area of radius R. Usually the footprint radius is called *travel distance* and is defined as the distance between the point of detection and

the point of the first interaction between the neutron and the ground. This distance, depending on the initial energy of the neutron and the number of collisions, can reach a maximum of 1 kilometer. Following [Zreda et al., 2008] and [Desilets et al., 2010] define the sensitivity area as 86% quantile or in other words, two e-folding. Defined with $W_r(\theta, h)$ the radial intensity of neutrons, the distance at which 86% of neutrons were detected was obtained solving the following equation:

$$\int_0^{R_{86}} W_r(\theta, h)\ dr = 0.86 \int_0^{\infty} W_r(\theta, h)\ dr \tag{2.15}$$

In Figure 2.11, is possible to distinguish three different regimes concerning the simulated neutron flux in different soil moisture and air humidity conditions. At distances of less than 10 meters, there is a peak relative to neutrons that emerge directly from the ground and are therefore more likely to be detected. For longer distances, up to 50 meters, we are within the average free path of most environmental neutrons. When exceeding 50 m, there are neutrons that have interacted with the ground several times. The simulated neutrons intensity distribution were then fitted using the following analytical function:

$$W_r(\theta, h) \sim \begin{cases} F_1(\theta, h)e^{-F_2(\theta,h)r} + F_3(\theta, h)e^{-F_4(\theta,h)r} & 0.5\ m < r \leq 50\ m \\ F_5(\theta, h)e^{-F_6(\theta,h)r} + F_7(\theta, h)e^{-F_8(\theta,h)r} & 50\ m < r \leq 600\ m \end{cases} \tag{2.16}$$

where $F_i(\theta, h)$ are functions of air humidity and soil moisture. In order to obtain $R_{86}(\theta, h)$ equation (2.15) was integrated numerically. Figure 2.12 shows the variations of this footprint for different air humidity and soil moisture conditions. Footprint variations are relevant in humid climate condition (from $10\%_{Vol}$ up to $40\%_{Vol}$) and dry soil condition ($\leq 3\%_{Vol}$). Footprint response to air humidity variations, instead, sees a decrease of ten meters for each change of about 4-6 g/m^3. This function is an essential tool when averaging point-scale probe measurements at different distances.

2.8 CRNS Depth

The second important parameter is the vertical sensitivity of the instrument, i.e. which is the effective depth which can be probed using cosmic ray soil moisture. It is useful comparing the soil moisture from neutron flux above ground with measurements from point-scale probes. The procedure followed in this thesis is explained in [Franz et al., 2012] and is briefly described in this section.

Franz assumes that the only hydrogen pools are from water on the surface of the soil, in liquid phase infiltrated into the soil and water in the mineral structure (lattice water), thus ignoring any variations in hydrogen from biomass and organic components within the soil. As described in the footprint characterization, vertical sensitivity is chosen as

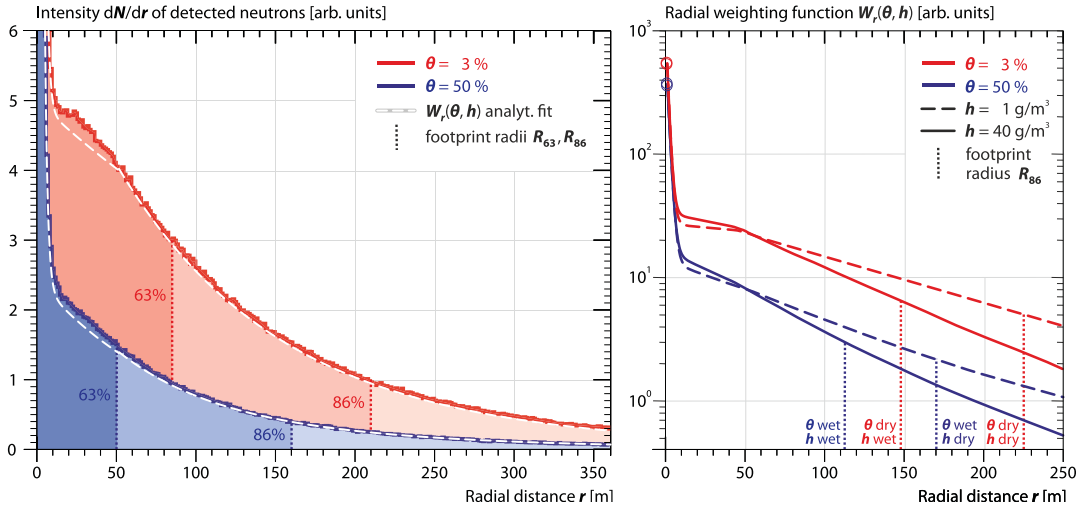

Figure 2.11: (Left) Detected neutron intensity dN/dr over distance r between origin and detection. (Right) Comparison of W_r and the corresponding percentile for four extreme cases of soil moisture and humidity. From [Köhli et al., 2015]

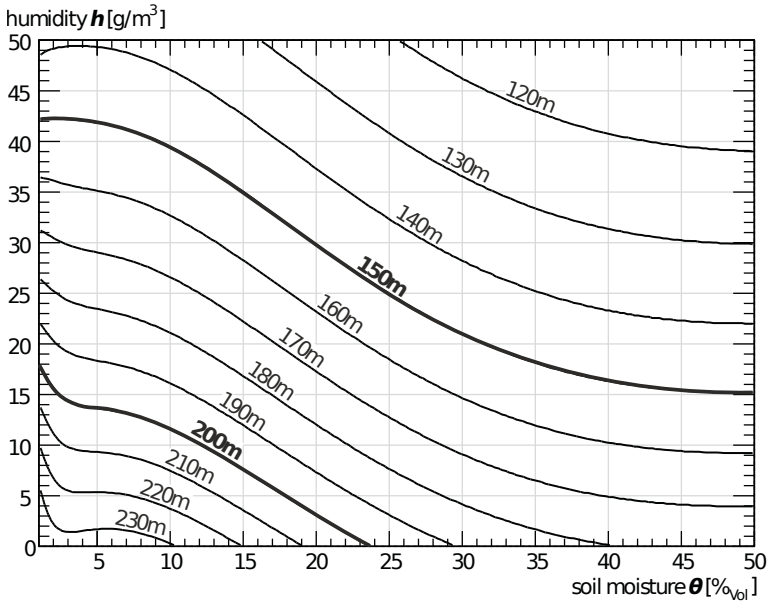

Figure 2.12: Footprint dependence on air humidity and soil moisture. Different profiles are highlighted.

the distance from which originate the 86% of detected neutrons. The proposed cumula-

tive sensitivity contour φ(cm) is defined as:

$$\varphi(z) = 5.8 - 0.0829z \qquad 0 \leq z \leq 70 \qquad \text{in cm.} \tag{2.17}$$

where z is the depth in soil which is defined positive downward. Using this contour function was possible to estimate the effective depth of different sources with different vertical distributions. The equivalent length of water for different hydrogen pools can be written as:

$$\mathrm{LW}(z) = \overbrace{W_S(z)}^{\substack{\text{Surface}\\ \text{water}}} + \underbrace{W_L(z)}_{\substack{\text{Lattice}\\ \text{water}}} + \overbrace{W_P(z)}^{\substack{\text{Pore}\\ \text{water}}} = W_S + \frac{\rho_{bd}(z)\tau(z)z}{\rho_w} + \theta(z)z \tag{2.18}$$

where ρ_{bd} is the dry soil bulk density, τ is the weight fraction of lattice water and θ is the gravimetric soil moisture. Summing over all hydrogen sources and imposing the equality with the 86% contour function:

$$\varphi(z^*) = W_S + \int_0^{z^*} \Big[\rho_{bd}(z)\tau(z) + \theta(z)\Big]\, dz \tag{2.19}$$

which can be solved for z^* obtaining the following estimate (see Figure 2.13 on the left)

$$z^* = \frac{5.8}{\rho_{bd}\tau + \theta + 0.00829} \tag{2.20}$$

Using this effective soil depth is then possible to define a weighted depth profile (see Figure 2.13 on the right):

$$wt(z) = a\left(1 - \left(\frac{z}{z^*}\right)\right) \qquad 0 \leq wt \leq z^* \tag{2.21}$$

where a is defined in order to conserve weights:

$$1 = \int_0^{z^*} a\left(1 - \left(\frac{z}{z^*}\right)^b\right) dz \tag{2.22}$$

This is the weight we will use in order to averaging between measurements coming from probes at different depths.

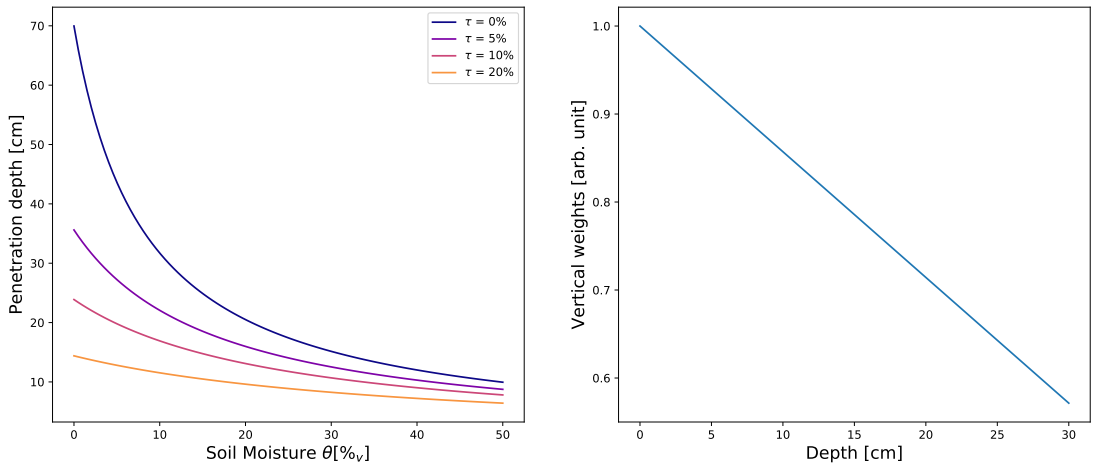

Figure 2.13: On the left, penetration depth as a function of soil moisture for different value of τ. On the right, vertical weights as a function of the depth. Dry soil condition correspond to the maximum achievable depth.

2.9 Simultaneous monitoring of soil moisture and biomass pattern

CRNS is sensible to all hydrogen pools, above and below the ground, with a certain footprint and depth sensitivity. This sensitivity to all hydrogen pools is an appealing characteristic which allows for continuous monitoring of soil moisture and biomass. Estimating directly biomass using CRNS is important either for directly correct the time-varying biomass effect on soil water content estimate; moreover, a field scale estimation of soil moisture and biomass can improve our understanding of the relationship between soil water content and plant growth [Jakobi et al., 2018]. In [Tian et al., 2016] the ratio between thermal and fast neutron intensity was proposed as a proxy for estimating aboveground biomass. This ratio was linked to biomass water equivalent through a linear relationship. In Figure 2.14 is plotted the CRNS biomass estimation togheter with direct measurements obtained by sampling on monthly basis the biomass.

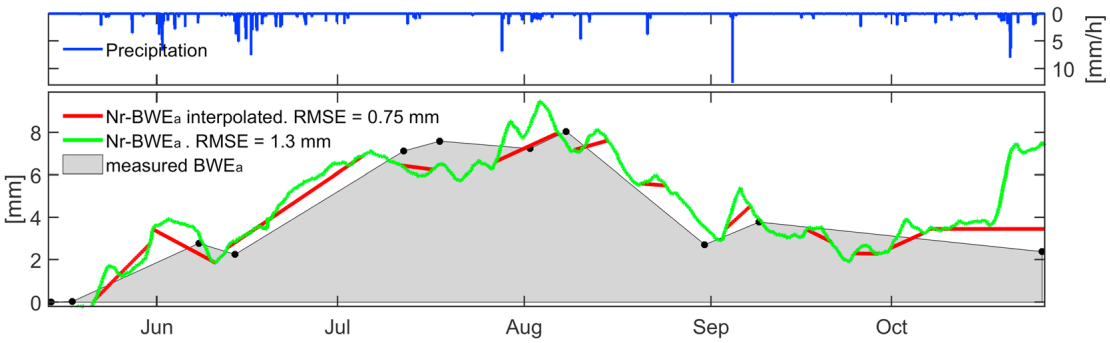

Figure 2.14: Time series of measured (gray area) and thermal to fast neutron derived (green line) aboveground biomass water equivalent. The red line show an interpolated time series of derived BWE_a. From [Jakobi et al., 2018].

Chapter 3

Neutron Detectors

In this chapter there is a review of the fundamental aspect of neutrons detection. The review follows closely the one in [Knoll, 2010].

3.1 Detecting neutrons

Neutron detection relies on the conversion of the incoming neutron into charged particles which is then detected. Usually, this conversion is done by taking advantage of a certain nuclear reaction. Since the reaction cross-section is strongly dependent on the neutron energy, usually neutron detectors are subdivided into two main class:

- Slow neutron detectors
- Fast neutron detectors

Following the established convention, all neutrons with energies below 0.5 eV are called "slow" the others are called "fast". At low energy, the dominant reaction is the neutron capture process. Neutrons detectors which exploit this reaction rely on the detection of the charged particles coming from the fragmentation of the compound nucleus formed by the neutron and the detector detection material. The most used elements are: ^{10}B, ^{6}Li, ^{3}He and ^{157}Gd. These material are chosen to maximizing the capture cross-section. These material are chosen to maximizing the capture cross-section. Moreover, when dealing with γ-rays background the reactions should also allow for the discrimination with neutrons. In order to achieve this, reactions with higher Q-value are favourites since the higher the Q-value, the greater the energy given to the reaction products and discriminating gamma events by amplitudes comparison. On the other hand, given the high Q-value, the incoming neutron energy information is completely lost since it is negligible with respect to the reaction Q-value. At higher energies, neutron capture

processes become less favorite. One possibility is represented by the moderation of neutron, which is then detected with slow neutrons detectors. These detectors suffer low efficiency since a fast neutron need to undergo different elastic scattering before being termalized and moreover the energy information is completely lost during moderation. Another possibility is to use elastic scattering processes where the kinetic energy of the incident neutron is transferred to a nucleus that then releases energy inside the detector allowing its detection. For such detector, low mass targets are preferable (H or C based) since the maximum transferred energy per collision decrease with the target atomic mass as can be seen in Eq. (2.6).

3.2 ^{3}He proportional counters

Proportional counters are gas-filled detectors which exploit the gas multiplication effects to amplify the charge from the original ionization pair. The gas multiplication effects are due to the increasing electric field in the gas, which usually needs a threshold voltage above 10^6V/m.

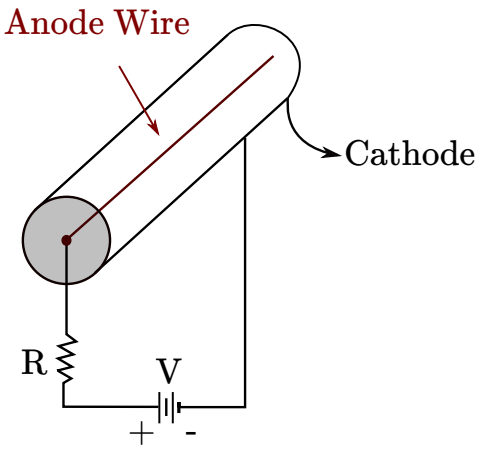

Figure 3.1: Proportional counter with a cylindrical geometry.

In Fig.3.1 there is a sketch of a possible detector configuration. The active area of the detector is filled with ^{3}He in order to take advantage of the following neutron capture reaction for converting the neutron in a charged proton:

$$\mathrm{n} + {}^3\mathrm{He} \longrightarrow \mathrm{p} + {}^3\mathrm{H} \qquad \text{Q-value} = 764 \text{ keV} \tag{3.1}$$

The reaction cross-section is 5330 barns which is higher with respect to other neutron capture reaction such as ^{10}B(n,α). The reaction products then ionize the gas, produc-

ing ion-electron pairs which start drifting toward their respective electrodes under the action of the high electric field leading to secondary ionization and avalanche formation. Typically an ^{3}He proportional counter has a diameter of few centimeters and length of tens of centimeters with internal gas pressure between 1 and 10 atm. ^{3}He proportional counter are widely used for CRNS application. Usually, they are equipped with moderating material, e.g. Polyethylene, in order to detect fast neutrons by thermalization. The popularity of this detector in CRNS application is because is nearly insensitive to the γ-background, and the gas is non-toxic and non-corrosive, can stand extreme environment and also high temperatures (up to 200°C). The drawback is that since ^{3}He is almost entirely produced in artificial context from nuclear weapon dismantling the costs are still high limiting the use of these instruments to universities and research centers, despite several opportunities have been recognized for practical applications [Kouzes, 2009].

3.3 Scintillators

Scintillator detectors rely on the emission of light produced by some material when exited for detecting ionizing radiation. A good scintillator material should have specific properties [Knoll, 2010]:

1. Convert kinetic energy of charged particles into detectable light with a good scintillation efficiency.

2. This conversion should be proportional to deposited energy and this proportionality should hold across a wide range of neutron energies.

3. The scintillation material should be transparent to its wavelength.

4. The decay time of the induced luminescence should be short so that fast signal pulses can be generated.

5. The material should be of good optical quality

6. In order to have good coupling with photomultiplier tubes the refraction index should be near that of glass (~ 1.5).

There is not a material which is able to match all the above criteria, and thus, when choosing a scintillation material, a trade-off between all these criteria should be done. There are two different categories of scintillator detectors: organic and non-organic. Usually, organics scintillators have a good timing response but lower energy resolution with respect to non-organics ones.

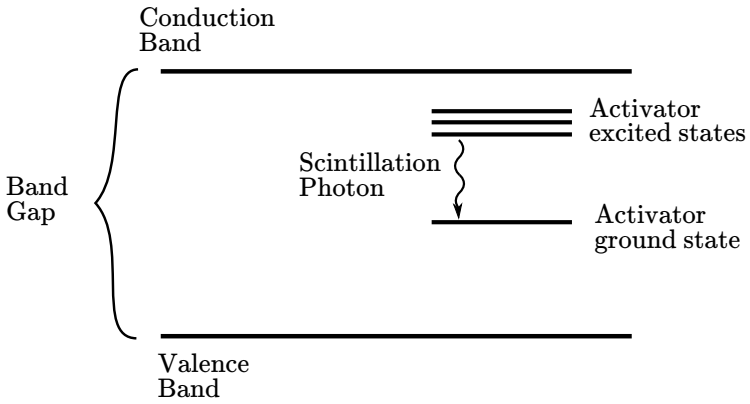

Figure 3.2: Energy band scheme of an activated inorganic scintillator crystal.

3.3.1 Inorganic scintillators

Scintillation mechanism in inorganic crystals relies on the discrete level scheme determined by the crystal structure Fig. 3.2 . These levels are grouped into energy bands. The lower one is called *valence band* and the higher one *conduction band*. Electrons in the valence band are bounded inside the crystal lattice whereas the electron within the conduction band is free to move inside the crystal. Between the two bands, there is a forbidden region called *band gap* in which electrons cannot be found in the pure crystal lattice. When an electron in the valence band is excited can be promoted to the conduction band leaving behind a hole in the valence band. When the crystal de-excite it emits a photon which represents the scintillation light. In a pure crystal, this mechanism is inefficient since the light produced would have a shorter wavelength than the visible one. To enhance the production of light in the visible region of the electromagnetic spectrum, some impurities, called activators, are added. Activators change the band structure by adding states which lie in the pure crystal forbidden energy region. Since the energy is now less then the full energy gap the transition give rise to the visible photon which could be used in scintillation process since the crystal is transparent to this light. Ionizing radiation is able to produce a large number of electron-hole pairs. The positive hole drift to the location of an activator site ionizing it since the ionization energy of the impurity will be lower than that if the pure crystal lattice. In the same time electrons migrate through the crystal until it encounters such an ionized activator in which can drop creating a neutral configuration that can have its configuration of excited states and if the activator state is created in an excited states it can de-excite through photon emission, with a characteristic time between 50 and 300 ns [Knoll, 2010]. Is important to note that there are processes which compete with the scintillation process described above, e.g. electron creating an exciting configuration whose transition to the ground state is

forbidden or when electrons are captured by an activator site leading to radiationless de-excitation process through crystal vibration (phonon excitations) called quenching.

Among inorganic scintillators there are two types which are widely used in neutron detection applications:

- Lithium Iodide activated with Europium and usually enriched with ^{6}Li.
- Zinc Sulfur activated with Silver ZnS(Ag) inserted in a compound with a high neutron capture cross-section material, e.g. ^{6}Li.

3.3.2 Organic scintillators

The scintillation process in organic scintillators relies on transitions in the energy level structure of an organic molecule and thus it is independent on the molecule physical state. Many of these detectors take advantage of specific molecules which exhibit particular symmetries which give rise to the π-electron structure, Anthracene for example is one of these molecules (Fig. 3.3). The π-electronic structure is shown in Fig. 3.4.

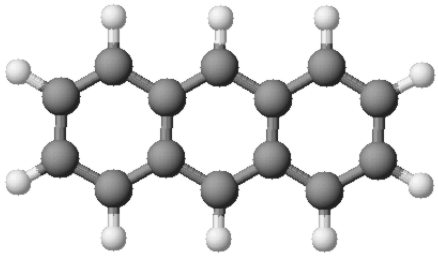

Figure 3.3: Molecular representation of the Anthracene molecule (Carbon in gray and Hydrogen in white). The symmetry of the molecule lead to the π-bond which are fundamental for the scintillation mechanism.

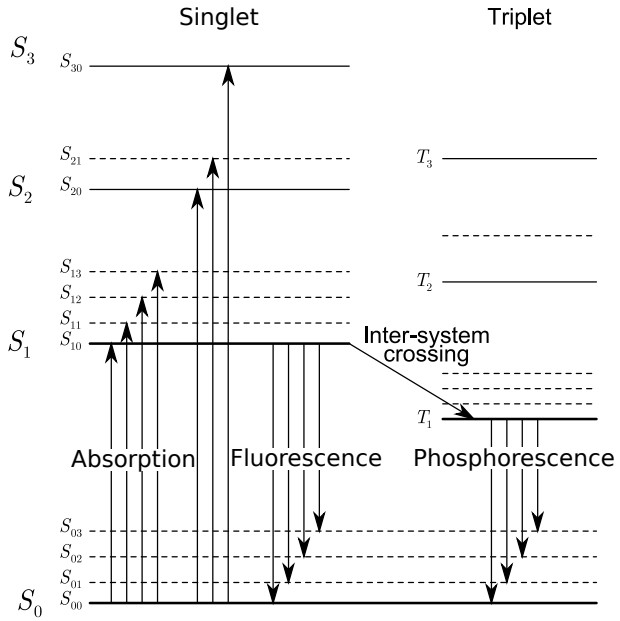

Figure 3.4: Organic scintillators molecules level scheme.

The energy level scheme has singlet states, labelled as S_i, and triplet states, labelled as T_i. Usually, the energy gap between the ground state and the first excited singlet state is about 3-4 eV unlike the spacing between higher-lying states which is smaller ($\sim$ 0.15 eV)

but still higher with respect to the thermal energy (~ 0.025 eV). Given these properties at room temperature, all molecules are in the S_{00} ground state. When a charged particle passes nearby excited electrons which can be promoted to higher-lying singlet states since the direct population of T_{ij} states from the ground state is forbidden. So right after the excitation molecule has a certain number of electrons in each S_{ij} states. All the higher singlet state de-excite with a characteristic time of the order of picosecond to the S_1 state through radiationless transitions. Moreover, all states with excess vibrational energy $(S_{i1}, S_{i2}, \dots)$ are not in thermal equilibrium with the environment leading to a loss of vibrational energy. Thus, the aftermath of the excitation process is the production, after a negligible time period, of a population of electrons in the state S_{10} [Knoll, 2010]. The scintillation light comes from the transition between this state and the ground state, which is called *fluorescence*. This prompt fluorescence intensity follows:

$$I(t) = I_0 \; e^{-t/\tau} \tag{3.2}$$

where τ is the characteristic time of the S_{10} which is usually of the order of the nanosecond. On the other hand, triplet states have a longer lifetime of the order of 10^{-3}s. Through a process called *inter-system crossing.* is possible to populate triplet state from excited singlet state. This process involves radiationless conversion between different electronic states or ionic recombination. These state can de-excite in two different way. The first is through the direct transition between T_{ij} and the ground state through the emission of *phosphorescence* light which has longer wavelength since the energy of the first triplet state is less than that of the first singlet one as can be seen in Fig.3.4. The other possible de-excitation relies on the excitation of an electron in a triplet state to a singlet ones leading to the so-called *delayed fluorescence*, the excitation energy can be given by thermal excitation or by the triplet-triplet annihilation process which is when two molecules in triplet state interacts producing one molecule in ground state and the other in the singlet state. The delayed fluorescence is of fundamental importance for particle discrimination purpose since the fraction of light that appears in the slow component often depends on the nature of the exciting particle.

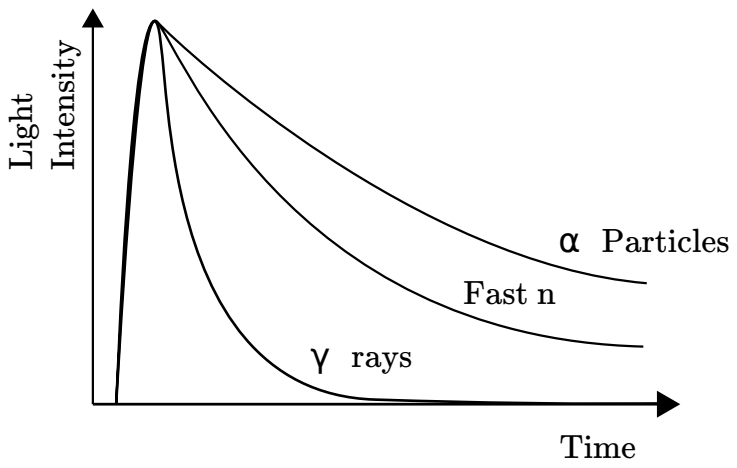

Figure 3.5: Time dependence of scintillators pulses when excited by different types of radiations.

This could be exploited to discriminate particles based on the so-called pulse shape discrimination. The slow scintillation component arise from de-excitation of previously excited triplet states along the ionizing track of the incoming particle. The slow component yield varies since triplet states density depends on the incoming radiation type. Given this, slow component fraction should depend primarily on the rate of energy loss dE/dx if exciting particle and should be greater for particles with higher dE/dx (see Fig. 3.5) [Knoll, 2010].

By looking at the energy level is also possible to understand why such molecules are transparent to it own scintillation light: the energy required for excitation is always higher than that obtained by de-excitation from S_{10} state and there is only a little overlap between optical absorption and emission spetra (see Fig. 3.6).

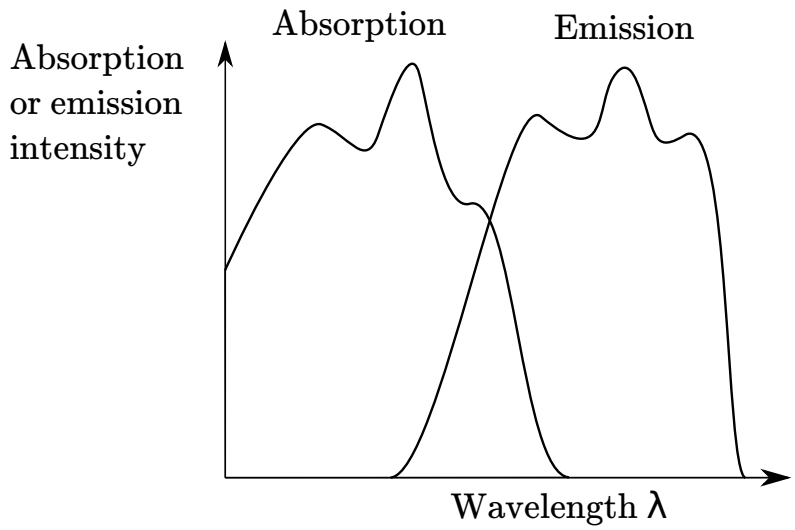

Figure 3.6: Optical absorption and emission spectra in a organic scintillator molecule.

Energy calibration

When a particle interacts with the molecules of an organic scintillator, part of its kinetic energy is converted into scintillation light and the amount of light produced depends on both the energy and the type of the interacting particle. Above 125 keV there is a linear proportionality between the light yields and the particle energy and this is due to the fact that above this energy the scintillation efficiency is energy independent [Knoll, 2010]. An important aspect to underline is that the response to heavy charged particles is less compared to that of equivalent energy electrons. This difference leads to the introduction of a special nomenclature in order to describe the absolute light yield called eVee, *eV electron equivalent*. The particle energy required in order to generate 1 eV is one eV for electrons and several eV for heavy particles due to their lower light yield per unit energy. Another fundamental aspect when dealing with organic scintillators is that the photoelectric cross section of its constituents is negligible in the energy range considered and this is due to their organic composition (C and H). Furthermore total absorption through multiple Compton scattering is negligible too, because of detector limited size. Thus, the detector response will be dominated by individual Compton interaction leading to an energy spectrum composed by a continuous distribution that corresponds to different angles of interaction (see Figure 3.7).

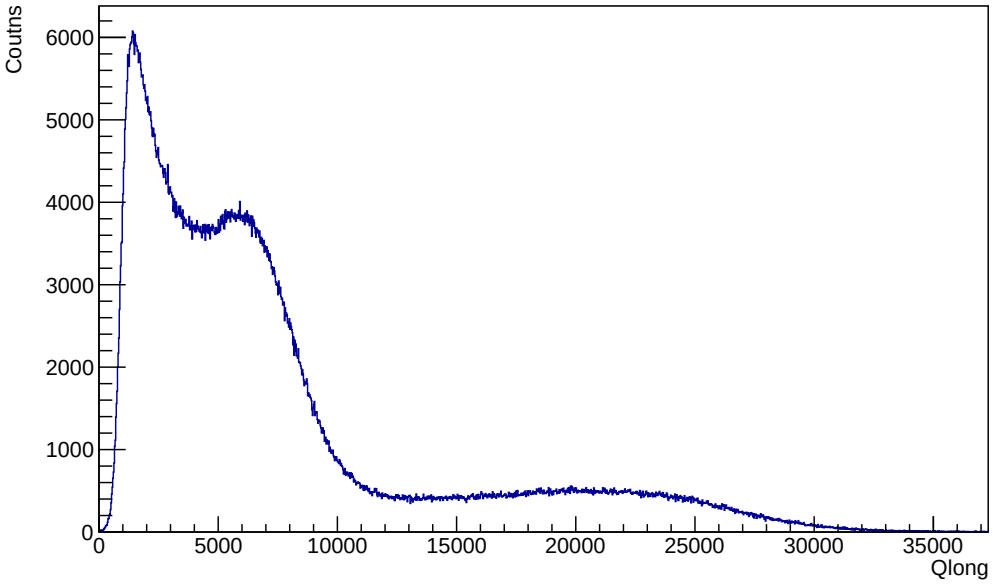

Figure 3.7: Uncalibrated energy spectra acquired with EJ-276 with an ^{22}Na source.

The maximum value is called *Compton Edge* and represent the maximum energy that can be transferred to the electron by a photon of energy E:

$$E_{CE} = \frac{2E^2}{m_e c^2 + E} \tag{3.3}$$

The calibration reference that were used during detectors characterization was provided by a ^{22}Na source. The β-decay of the ^{22}Na lead to the production of an electron neutrino and a positron:

$$^{22}\mathrm{Na} \longrightarrow {}^{22}\mathrm{Ne} + \nu_e + e^+ \tag{3.4}$$

which is followed by the emission of a 1275 keV photon, corresponding to an energy of 1062 keV for the Compton edge, from the ^{22}Ne excited state. The emitted positron can annihilate with an ambient electron leading to the emission of two gamma-ray of 511 keV correspoding to an energy of 340 keV for the Compton edge. The finite resolution the detector results in a shift towards lower energies depending on the detector resolution which can be seen in the spectra acquired with the ^{22}Na source in Fig. 3.7.

Following the procedure described in [Stevanato et al., 2011] is possible to use the Compton edges in order to calibrate the detector. The procedure use the Klein-Nishina formula in order to retrieve the differential scattering cross-section as a function of the interacting electron:

$$\frac{d\sigma}{dT} = \frac{\pi r_e^2}{m_e c^2 \alpha^2}\left(2 + \frac{s^2}{\alpha^2(1-s)^2} + \frac{s}{1-s}\left(s - \frac{2}{\alpha}\right)\right) \tag{3.5}$$

where r_e is the classical electron radius and $\alpha = h\nu/m_e c^2$ is the photon energy. Using this formula is possible to reconstruct the theoretical distribution of Compton scattering events. Starting from this theoretical result different Gaussian smearing were done varying the σ (see Figure 3.8). Summing these Gaussian lead to experimental distributions mimicking the finite resolution of the detector.

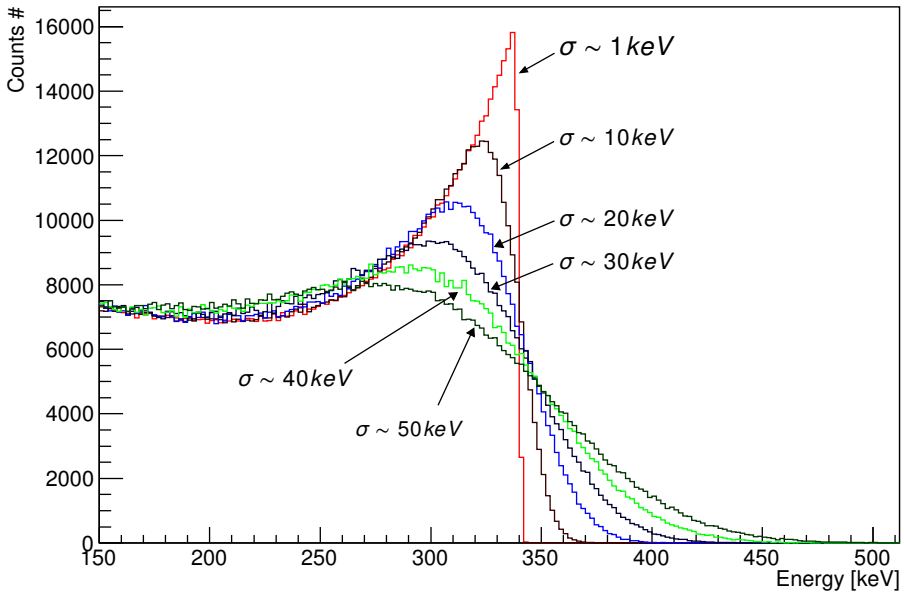

Figure 3.8: Gaussian smeared spectra at different σ generated using the Klein-Nishina Compton scattering cross section for 511 keV photon.

Chapter 4

A novel cosmic-rays neutron detector assembly

As reported in the previous chapter ^{3}He-based proportional counters are widely used in CRNS application. The interest of neutron detection for homeland security applications has triggered in the last decade the development of new detectors made up of liquid or plastic scintillation materials with low toxicity, safe and easy to use which can be used in CRNS application. In this thesis a new solution, namely Finapp, based on a composite detector made of commercial detectors is studied [Cester et al., 2016].

4.1 The detector system

In Fig. 4.1 is represented a block scheme of the measuring system which is composed by the following component:

1. The detectors assembly for γ-ray, neutrons and muons detection.
2. Pressure sensor for calibration and correction of raw neutrons counts.
3. An electronic signal digitizer.
4. High-voltage supply.
5. A single board computer for online analysis.

4.1.1 The detector assembly

The detector is built using two scintillators: EJ-299-33A, EJ-420 and EJ-426, manufactured by Eljen Technology (Sweetwater, TX, USA). EJ-420 and EJ-426 are inorganic

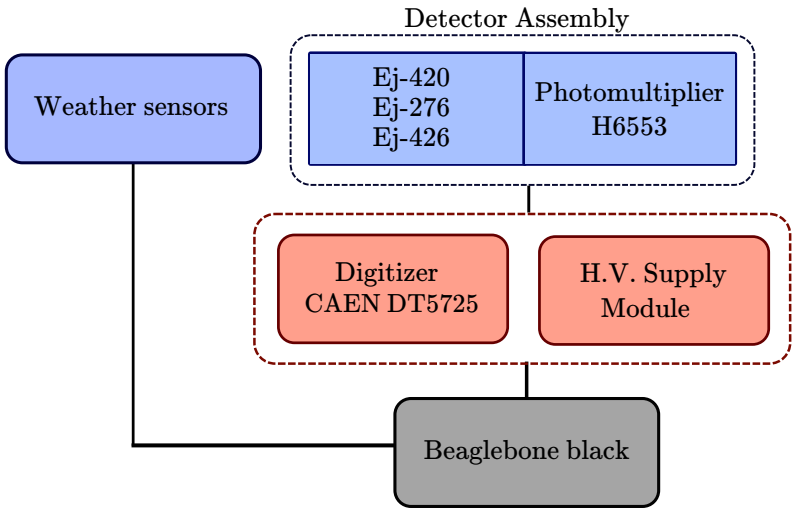

Figure 4.1: Block scheme of the portable detection system.

scintillators, that have proven to have a good response to thermal neutrons [Pino et al., 2015]. EJ-299-33A was the first plastic detector to become commercially available for gamma/fast-neutron discrimination [Cester et al., 2014]. The discrimination capability of neutrons from gamma-rays is a fundamental prerequisite, in order to discriminate neutrons from the naturally occurring gamma-ray environmental background, that is not correlated to soil moisture in the same way as neutrons [Strati et al., 2018].

EJ-420

The EJ-420 is an inorganic scintillators for thermal neutrons detection. Since its thin structure make it nearly insensitive to γ-radiation. The detector employs a lithium compound, whose Lithium content is enriched to 95% ^{6}Li dispersed in a ZnS:(Ag) matrix.

The reaction on which this detector relies is:

$$^6_3\mathrm{Li} + n \longrightarrow {}^3\mathrm{H} + \alpha \tag{4.1}$$

This reaction has a cross section of 941 barns for thermal neutrons. The Triton and alpha particle produced are then detected in the ZnS:(Ag) phosphor which is chosen for its short decay time characteristics. Detection efficiency is energy dependent and is about 30 % for neutrons under 1 eV and 60% under 0.01 eV. It may be surrounded by an

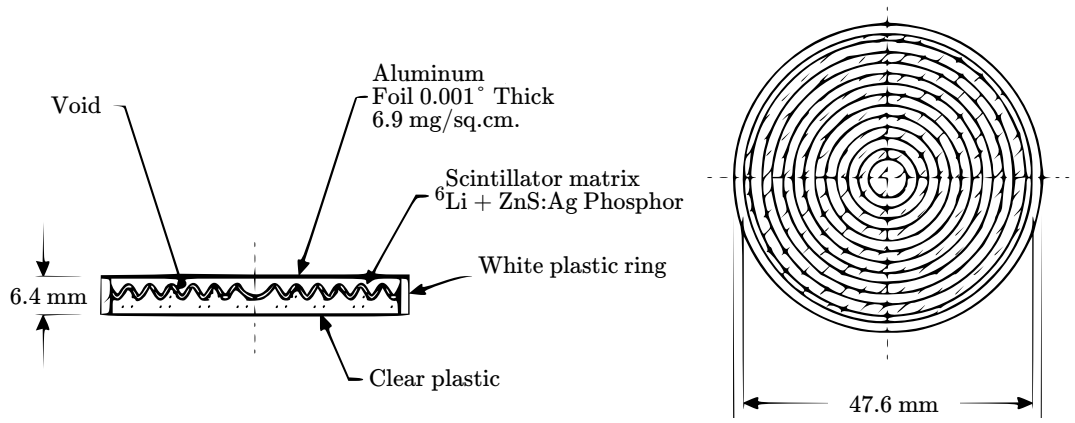

Figure 4.2: EJ-420.

appropriate quantity of hydrogenous material for neutrons thermalization. The neutron flux is determined above a desired rejection ratio of gamma radiation or photomultiplier noise by setting the pulse height analyzer or discriminator of the associated electrical equipment to an appropriate level. This is adequate for most applications, but if the flux of gamma rays is very high, pulse shape discrimination may be effectively used.

Properties	EJ-420
^{6}Li content	9 mg/cm^2
Pulse Height	120 (% NaI(Tl))
Wavelength of Maximum Emission	450 nm
Decay Time, Short component	0.2 μs

Table 4.1: EJ-420 Properties.

EJ-246

The EJ-426 detector has the form of a flat, white, thin sheet consisting of a homogeneous matrix of fine particles of lithium-6-fluoride (^{6}LiF) and zinc sulfide phosphor (ZnS:Ag) compactly dispersed in a colorless binder Fig.4.3. The EJ-426 is similar to the EJ-420 since it relies on the same reaction for thermal neutrons conversions. The decay time of the prompt scintillation component is 200 ns. The emission spectra is plotted in Fig. 4.4.

EJ-299-33A

EJ-299-33A is a plastic scintillator used for for gamma/fast-neutron discrimination. Plastic scintillators are well suited for environmental measurement since they are non-

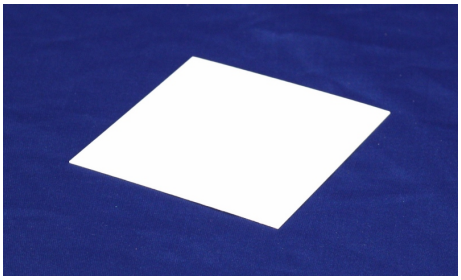

Figure 4.3: EJ-426 sheet

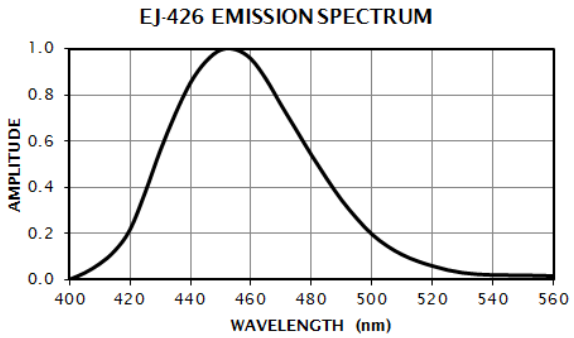

Figure 4.4: EJ-426 emission spectra

Properties	EJ-426
^{6}LiF:ZnS Mass Ratio	1:3
^{6}Li Density	8.81×10^{21} atoms/cm^3
Theoretical NTH Efficiency (0.5 mm)	0.23

Table 4.2: EJ-426 Properties.

toxic and easy to handle (see Figure 4.5). This detector was developed at the Lawrence Livermore National Laboratory using a polyviniltoluene matrix enriched with 2,5-Diphenyloxazole and was made commercially available by Eljen technology. Its temporal and energy resolution is comparable to that of liquid scintillators but at low energy the discrimination between γ-ray and fast neutrons is less efficient. The emission spectrum is shown in Figure 4.6) and its principal characteristic are reported in Table 4.3.

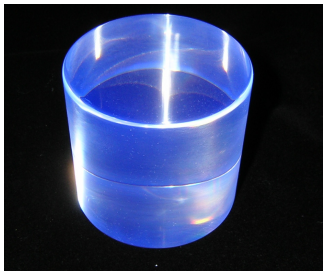

Figure 4.5: EJ-299-33A cylinder.

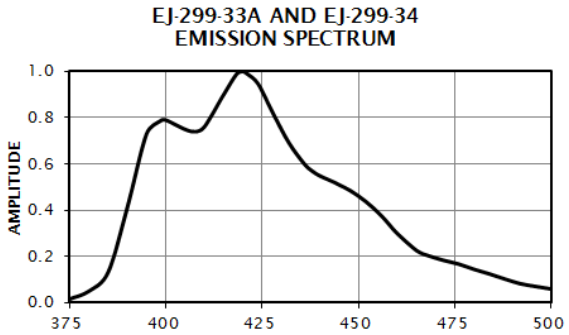

Figure 4.6: EJ-299 emission spectra

Properties	EJ-299-33A
Light output	56 (% Anthracene)
Wavelength of maximum emission	425 nm
No. of H Atoms per cm^3	4.546
No. of C Atoms per cm^3	4.906
No. of Electrons per cm^3	3.533
Density	1.096 g/cm^3
Approx. mean decay times of first 3 components	Gamma Excitation 13,35,270 ns Neutrons Excitation 13,59,460 ns

Table 4.3: EJ-299-33A Properties.

Mechanical assembly

The composite detector was assembled by wrapping the plastic scintillator for fast neutrons detection, EJ-299-33A (a cylinder of 3" × 3") with a layer of detectors for slow neutrons. An EJ-420 with the same diameter was used on the front, coupled with a special silicon pad (EJ-560). The lateral side, was wrapped with the flexible EJ-426 .This detector exhibits lower efficiency which is compensated by its excellent elastic properties that allowed it to be wound around the main detector. The free face of the central detector was coupled to the photomultiplier, Mod. H6553 (Hamamatsu Photonics, Hamamatsu, Japan), through the EJ-560 pad. An exploded view of the assembly is shown in Figure 4.7. As seen in Figure 2.8 the most sensitive part of the neutron spectrum goes from 0.025 eV up to 100 keV, to detect these neutrons, the assembled is provided with a few centimeters of polyethylene that acts as a moderator bringing the neutrons in the epithermical zone to the region of thermalization.

4.1.2 Data Acquisition system

The data acquisition system (DAQ) was composed of an electronic signal digitizer model DT5725 (CAEN Spa, Viareggio, Italy) connected to the PMT anode. This model has a 12 bit resolution with a sampling rate of 250 MS/s. The oscilloscope mimics the behaviour of a digital oscilloscope. These devices have an Analogue-to-Digital converter flash with a specific dynamic range to which the analog signal must be adapted to avoid saturation. The digitized signal is stored in a circular buffer whose size is programmable. When a particle interacts with the detector and releases scintillation light, the scintillation light is converted into an electrical pulse by the photomultiplier. Since the signal is read at the anode, what is observed is a voltage drop compared to a reference value that is called a baseline. The digitizer converts the analog signal into digital continuously overwriting the circular buffer. When there is a voltage difference between the baseline and the digital signal, higher than a preset value called the threshold, the trig-

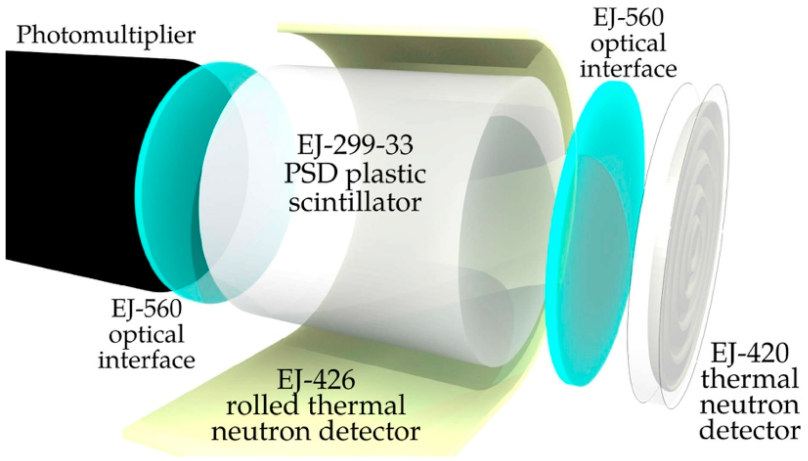

Figure 4.7: Assembly of the detector, Finapp, to employ in cosmic-ray neutron sensing (CRNS) technique. Abbreviation: PSD, pulse shape discrimination.

ger condition is verified. When the trigger signal is sent, the circular buffer is stopped and made readable while the acquisition is moved to another memory thus allowing possible trigger events close to each other eliminating, or at least reducing, the acquisition dead times. Another advantage of this type of instrument is its ability to perform a preliminary analysis of the waveform. This is possible thanks to an integrated FPGA that implements algorithms able to calculate online several parameters like total charge, short charge, baseline, timestamp etc. This can be useful to decrease the number of information that must be downloaded to the next stage of the analysis chain. This calculation requires the setting of a number of parameters : pre-gate, short gate and long gate that represent, respectively, the points of beginning of integration, and the number of samples used during the partial and total integration of the digital signal from which the baseline value is preventively subtracted. Each event is associated with a timestamp that equals the number of sample units since the acquisition was started. The parameters described above are represented in Figure 4.12. The digitizer is connected with a low-cost, low-power, embedded computer, called Beaglebone Black, which runs a Linux distribution. The software controlling the digitizer is an open-source, distributed data acquisition system, called ABCD, which is a Data Acquisition System (DAQ) with a distributed architecture [Fontana et al., 2018]. Each task related to the DAQ (acquisition, pre-process, analysis, ...) runs in a separate process. In other words, the system is composed of a set of very simple servers that exchange information through dedicated communication sockets. ABCD is employed to provide a continuous stream of data to a custom analysis system. The probe was equipped with internal temperature sensors and was configured to gather weather data from a local weather station installed near the probe.

Figure 4.8: Digitizer DT5725.

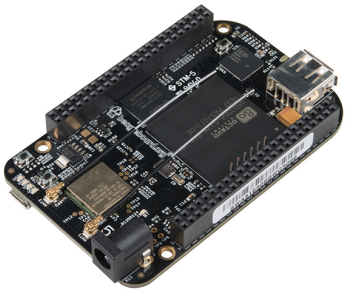

Figure 4.9: Beaglebone black.

Characteristic	Characteristic	
2 Low Voltage bias outputs for preamps driving (± 12 V, ± 24 V)	Processor	AM335x 1GHz ARM Cortex-A8
0.5 and 2 Vpp selectable input dynamic range with programmable DC offset	RAM	512 MB DDR3
14-bit at 250 MS/s Waveform Digitizer	Storage	4GB 8-bit eMMC on-board flash storage
8 channels	Connectivity	USB client for power and communication, ethernet and HDMI
Analog inputs on MCX coaxial connectors		

Figure 4.10: DT-5725

Figure 4.11: Beaglebone black

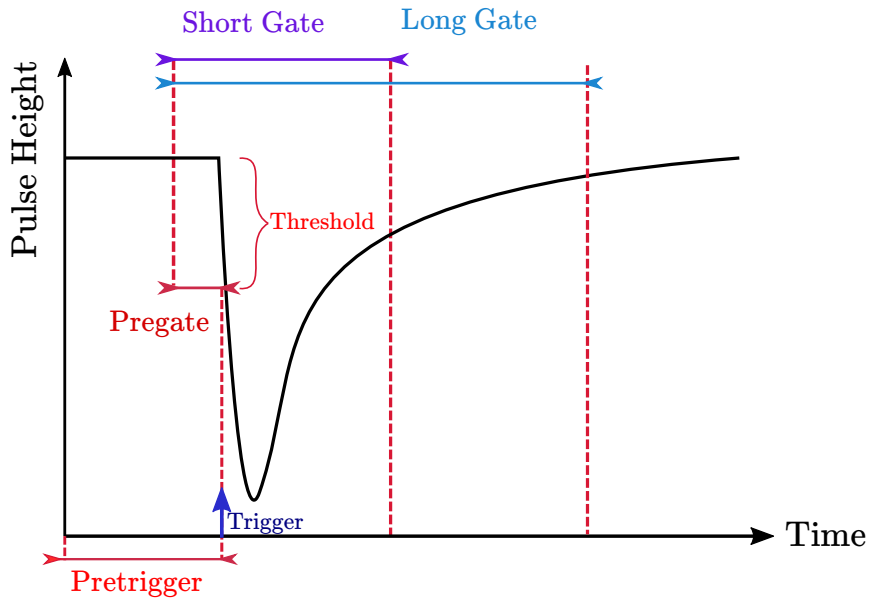

Figure 4.12: Signal integration gates.

4.2 Particle discrimination

Starting from the digitized signal the DAQ software computes a set of features which are used for discriminating among different radiation sources and deleting noise signals (see Table). It is used the PSD to discriminate among neutron, gamma and muons. As seen in the previous chapter pulse shape discrimination relies on the fact that the slow scintillation light component yield depends on the exciting radiation. Usually the Pulse Shape Discrimination (PSD) parameter is defined as follow:

$$\mathrm{PSD} = \frac{\mathrm{qlong} - \mathrm{qshort}}{\mathrm{qlong}} \tag{4.2}$$

where `qlong` and `qshort` are two parameters which represent two different integration gates (See in Fig.4.12), these two parameters need to be optimized in order to ensure optimal particle discrimination. Particles with higher PSD values have a greater slow component yield allowing discrimination between different radiation type (see Figure 4.13).

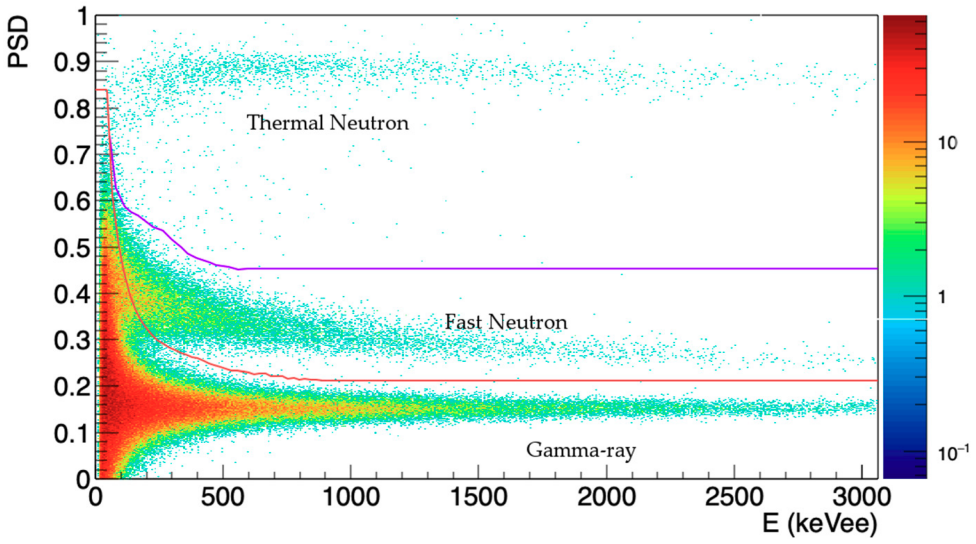

Figure 4.13: PSD parameter as a function of energy. Different radiation types are associated to different region delimited by polynomials.

4.3 Calibration

As seen in Chapter 3, when using organic scintillators is not possible to use photopeaks to calibrate the detector, due to their negligible photoelectric effect cross-section, nevertheless, is possible to use the Compton edge in order to perform an energy calibration of the instrument. The calibration spectrum was obtained using a ^{22}Na source. Following the smearing procedure seen in Section 4.3 the χ^2 between experimental spectrum and Gaussian smeared spectra was minimized looping over different σ values for both Compton edge at 340 keVee and 1062 keVee (see Figure 4.14a and 4.14b). For the Compton edge at 340 keVee, before the χ^2 optimization phase is mandatory to subtract the Compton shoulder due to the Compton edge at 1062 keVee. The shift of the Compton edge associated to the σ was used to calibrate the detector. Values are shown in Table 4.4.

The obtained calibration function is:

$$E(\text{qlong}) = a \cdot \text{qlong} + b \qquad a = 0.05 \text{ keVee/qlong}, \; b = -5 \text{ keVee} \tag{4.3}$$

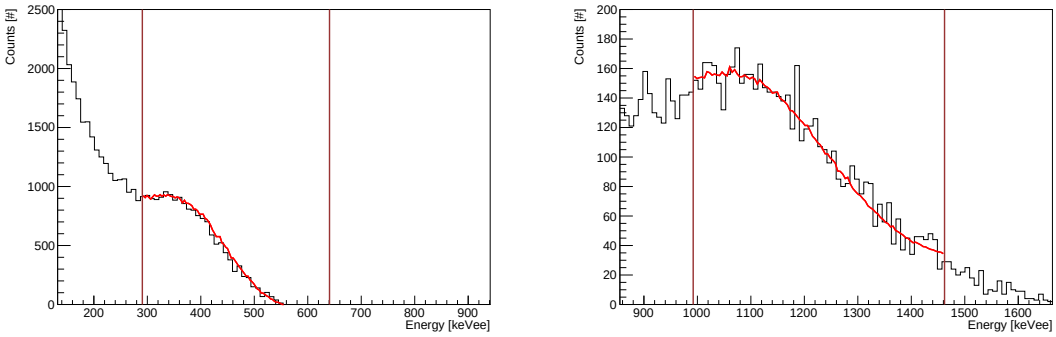

(a) (b)

Figure 4.14: ^{22}Na spectrum acquired with EJ-299-33A. (a) Spectrum around the 340 keVee Compton edge (black line) togheter with the smeared spactra corresponding to the minimum of χ^2 (red line) having a $\sigma = 75$ keVee. (b) Spectrum around the 1062 keVee Compton edge (black line) togheter with the smeared spactra corresponding to the minimum of χ^2 (red line) having a $\sigma = 128$ keVee.

Photon Energy [keVee]	σ [keVee]	Resolution	C.E. shifting [keVee]
511	68	20%	88
1275	128	13%	142

Table 4.4: σ, Resolution and C.E. shift for EJ-299-33A.

4.3.1 Calibration monitoring

Since the system has to acquire data continuously for more than a month, energy calibration should be monitored in order to rule out possible changes in the system gain. This is important because by changing the gain events associated with γ-rays, in the energy PSD plane, approach the neutrons region. Since discrimination polynomials are fixed this effect can lead to misclassifications (see Fig. 3.5).

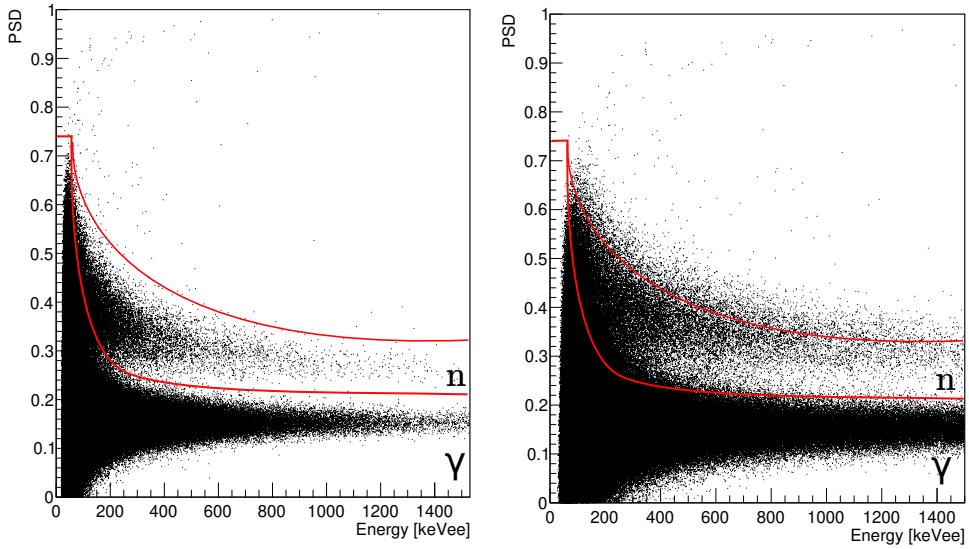

Figure 4.15: (Left) Under nominal gain conditions, neutrons and gamma are within their respective regions of belonging. (Right) A gain change can lead neutrons and gamma events out of their respective regions distorting fast neutron counts.

Since is not feasible to use a calibration source during field tests, is possible to use the environmental ^{40}K Compton edge to monitor the calibration status.In Figure 4.16 is plotted the environmental gamma spectrum given an hour of acquisition time where the ^{40}K Comtpon edge is highlighted. In order to extract the position of the ^{40}K Compton edge was used a ROOT [Antcheva et al., 2011] function, called `Background`. This function, based on the Sensitive Non-Linear Iterative Peak clipping algorithm (SNIP) [Morháč and Matoušek, 2008] allow for a linear background estimation based on a set of parameters. In Figure 4.17 is shown the result of the ROOT background subtraction, the average of this histogram was taken as Compton edge position.

A source of the aforementioned changes in the system gain is the thermal dependence of the photomultiplier. This effect can be seen in Figure 4.18 where the correlation between the ^{40}K Compton edge peak energy and the temperature is showed.

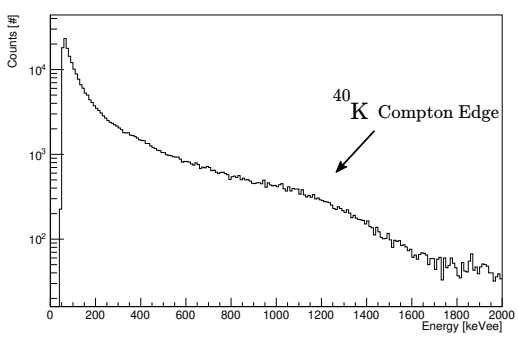

Figure 4.16: Environmental γ spectrum.

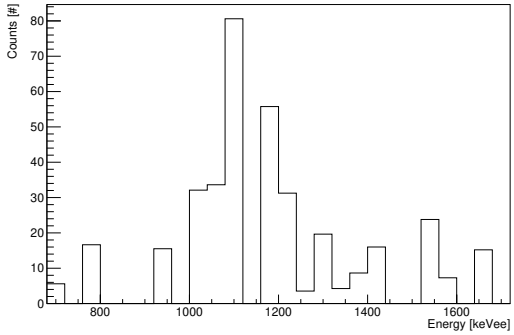

Figure 4.17: Environmental γ spectrum after background subtraction in the ^{40}K Compton edge region.

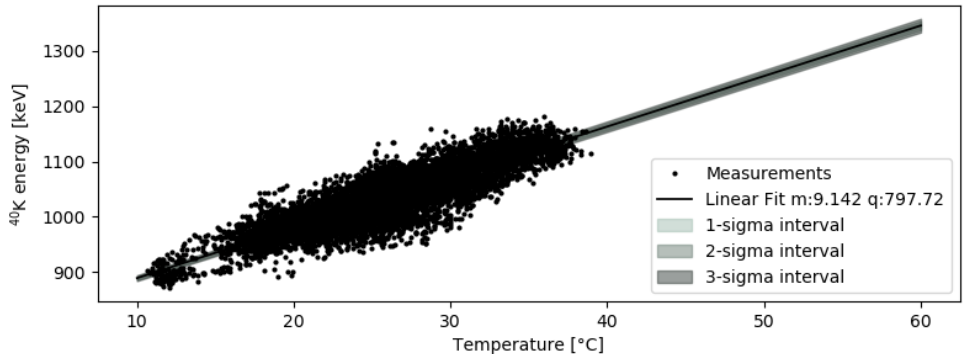

Figure 4.18: Correlation between ^{40}K and environmental temperature.

In order to minimize this effect it is therefore necessary to introduce corrections that make the position of the ^{40}K Compton edge stables, thus eliminating the variation due to temperature. The first order correction has to account for the temperature dependence. Nevertheless, since the photomultiplier has a certain thermal inertia, a proper filtering on the raw temperature measurement has to be done.

Temperature measurements were low-pass filtered using a moving average filter, which can be described by the following finite difference equation:

$$y[n] = \frac{1}{M} \sum_{k=0}^{M-1} x(n-k) \tag{4.4}$$

where $y[n]$ represent the filtered signal, $x[n]$ the input one and M the so-called *average window width*. By computing the $\mathcal{Z}$ - transform of the finite difference equation is possible to retrieve the transfer function behavior:

$$H(z) = \frac{1}{M} \sum_{k=0}^{M-1} z^{-k} = \frac{1}{M} \frac{1-z^{-M}}{1-z^{-1}} \tag{4.5}$$

which correspond to the following frequency response:

$$H(e^{j\theta}) = \frac{1}{M} e^{-j\frac{M-1}{2}\theta} \frac{\sin\left(\frac{\theta}{2}M\right)}{\sin\left(\frac{\theta}{2}\right)} \tag{4.6}$$

As can be seen in Figure 4.19 and 4.20 magnitude and phase depend on the average window width. Thus, the shift introduced by the filter depends also on this parameter. The maximum achievable correlation between the two observables is obtained when the shift introduced by the filter match the thermal inertia of the photomultiplier. With the

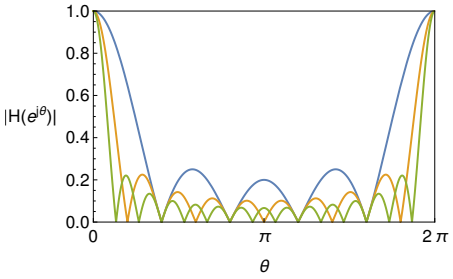

Figure 4.19: Module.

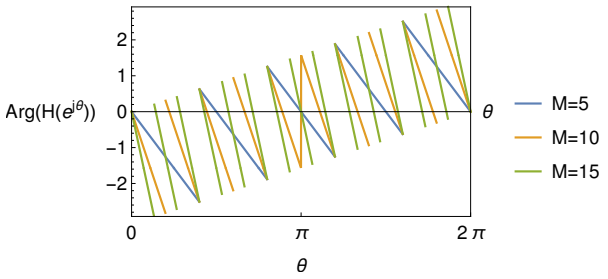

Figure 4.20: Phase.

Figure 4.21: Module and phase of the moving average filter for three different value of M.

aim of finding the optimal window width a grid-search was performed using the Pearson correlation coefficient between the filtered temperature signals and ^{40}K Compton edge energy as a figure of merit (see Fig. 4.22). The Pearson coefficient gives a measure of the correlation between two observables and is defined as follow:

$$\rho_{X,Y} = \frac{\mathrm{cov}(X,Y)}{\sigma_X \sigma_Y} \tag{4.7}$$

where $\mathrm{cov}(X, Y)$ is the covariance between the two variables and σ is the standard deviation. The result is plotted in Figure 4.22, the optimal width correspond to 40 samples (i.e. 3 hours). Pearson coefficient drops about 7-8% using instantaneous temperature.

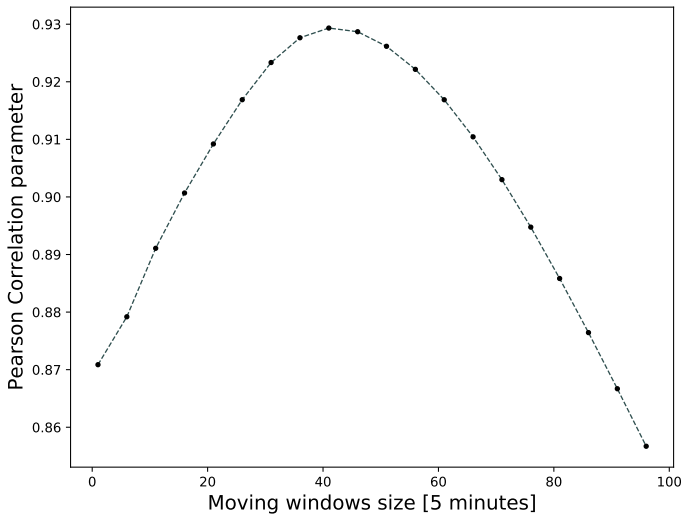

Figure 4.22: Moving average of three different cases.

In Figure 4.23 is showed the effect of such correction on the ^{40}K Compton edge position. The red line is the uncorrected series which exhibit an oscillation due to day to night temperature excursion, the orange line, instead, is the temperature corrected position.

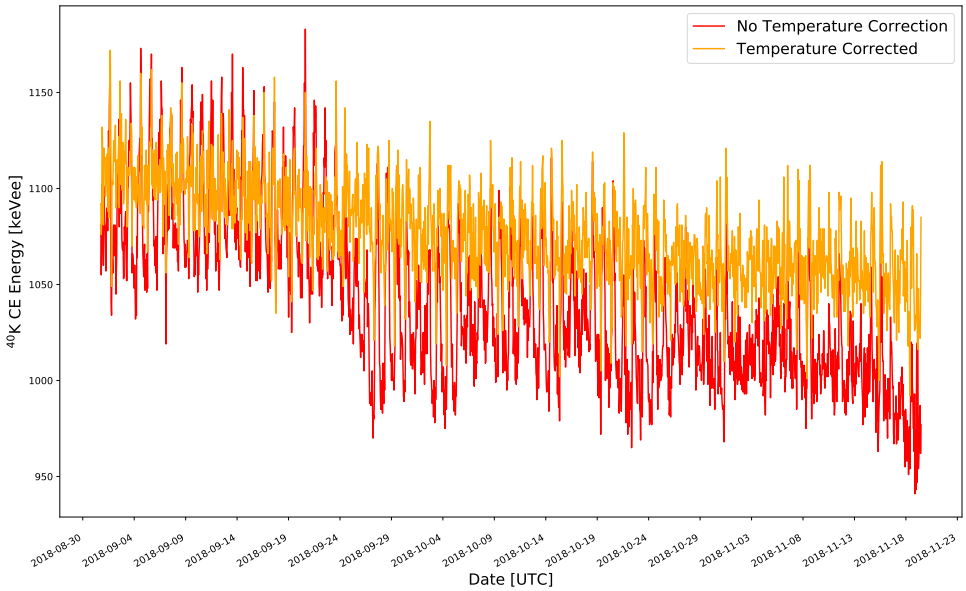

Figure 4.23: Comparison between raw estimation of the ^{40}K Compton edge (Red Line) and the temperature corrected one (Orange Line).

Nevertheless, from the plot is clearly visible a degradation in the Compton edge energy position which proceeds linearly with a slope of 0.03 keVee/hour that has to be corrected. This effect could be attributed to dynodes degradation due to long period of acquisition under harsh operating condition. Indeed, the operating stability of the dynodes is an important factor that affects the stability over time of the PMT [Hamamatsu, 2007]. With this objective, every ten minutes the environmental gamma spectrum acquired in the previous hour is updated in order to track the position of the ^{40}K peak and realign the peak position by multiplying for a normalization parameter defined as:

$$\text{normK} = \frac{\text{Theoretical } ^{40}\text{K peak position}}{\text{Measured } ^{40}\text{K peak position}} \tag{4.8}$$

The effect of this correction is showed in Figure 4.24 where the orange line is the temperature corrected position and the purple line is corrected both for temperature and normK.

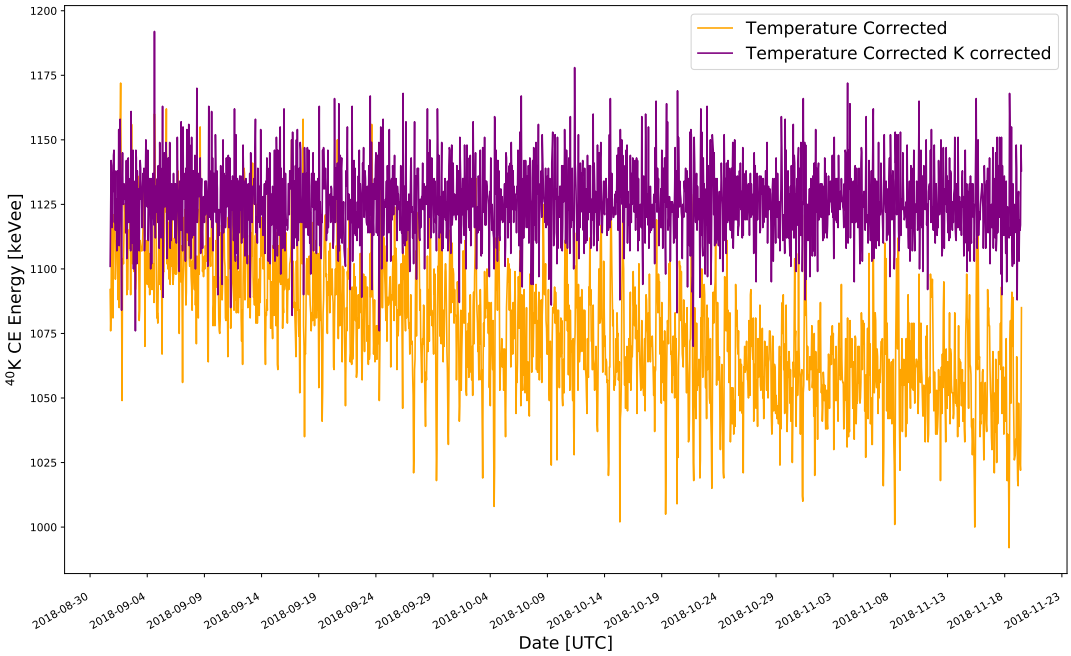

Figure 4.24: Comparison between temperature corrected estimation of ^{40}K Comtpon edge and temperature (Orange Line) and normK corrected (Purple Line).

To summarize, each correction step is plotted in Figure 4.25, where is clearly visible the difference between the corrected and uncorrected energy calibration. Without any correction, (red line) energy calibration is affected by temperature variation which lead to a broad distribution of the Compton edge distribution ($\sim$ 100 keV); accounting for the temperature correlation (orange line) lead to an improvement of the full-width at half-maximum of about 39% ($\sim$61 keV).

Finally, adding the Compton edge tracking (purple line) lead to a further improvement of the full-width at half-maximum of 44% (∼34 keV) (see Figure 4.26).

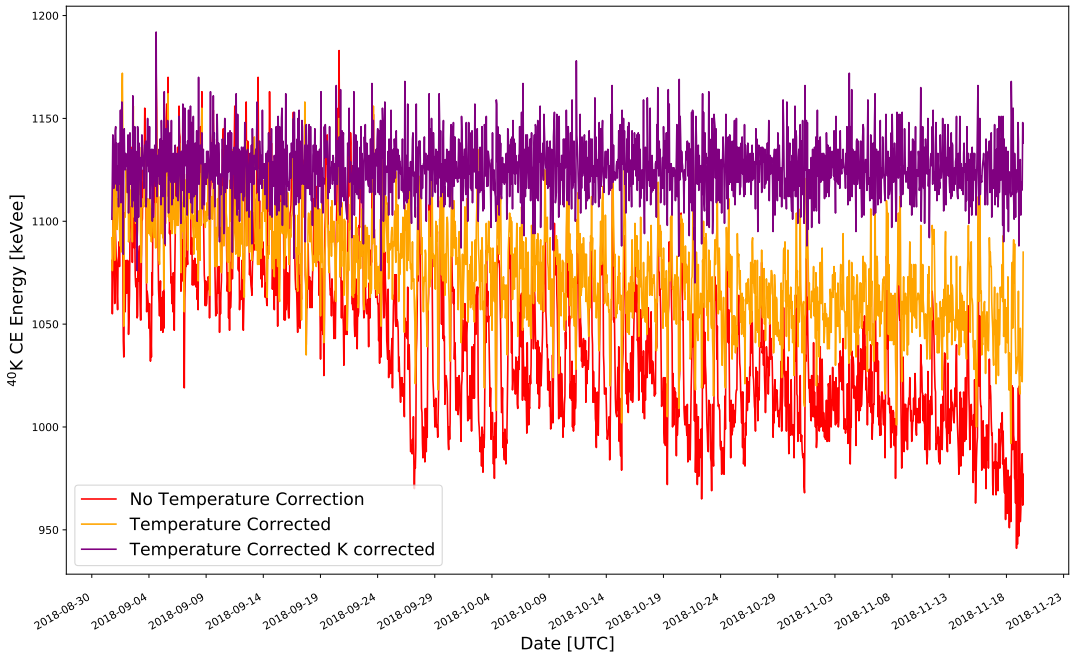

Figure 4.25: ^{40}K Compton edge energy estimate after each correction. Raw (Red Line), Temperature corrected (Orange Line) and Temperature and normK corrected (Purple Line).

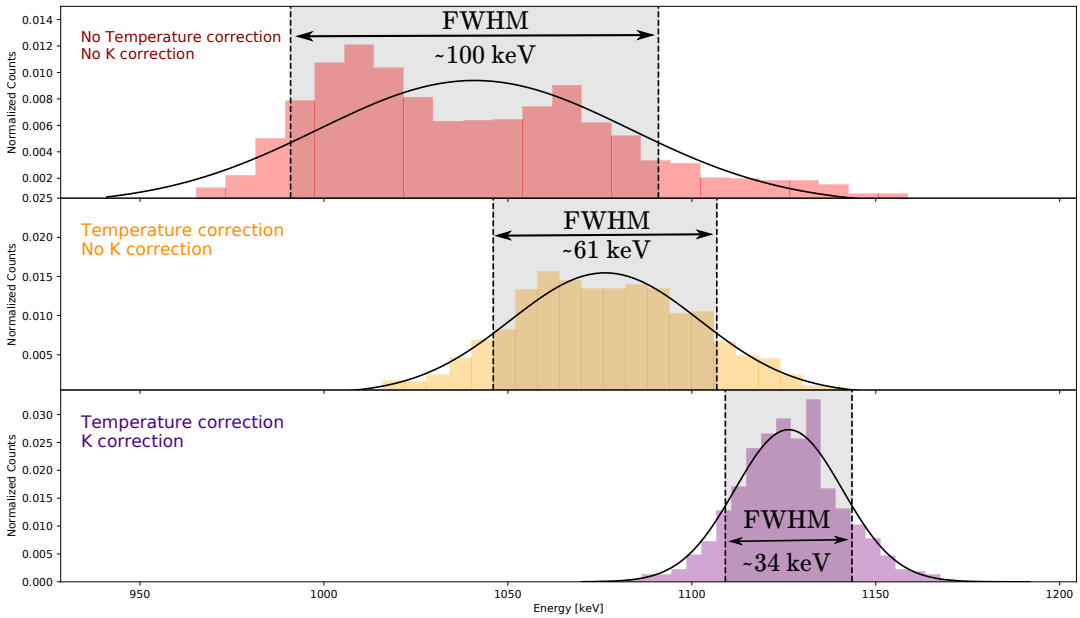

Figure 4.26: Effect of temperature correction and Comtpon edge traking corrections on the ^{40}K peak position distribution.

4.4 Experimental test

4.4.1 Experimental site

The probe was installed for a three months data acquisition campaign, between August 8th to November 11th 2018, with the aim of comparing the new assembly detectors with commercial probes. The probe was hosted by the Porto Felloni agricultural company, which is active in precision agriculture practices, located in Lagosanto, Emilia Romagna. The experimental site is located a few kilometers from the sea characterized by warm climate and by dry summer period with annual rainfall of about 600 mm. The probe was located near a walnut trees orchard with a footprint represented by an area with diameter of about 300 m, which is highlighted by the red circle in Figure 4.27a. In Figure 4.27b there is a photo of the installation.

Figure 4.27: (Left) Field site (N 44.752756, E 12.134761), red point is where the Finapp probe was installed, the red circle is the footprint, the orange point represents where the five Sentek probes are installed at different depths, and the light blue line is the drainage canal. (Right) Picture of the installation.

At 90 meters from the probes there were installed five Sentek point-scale probes at different depths (10,20,30,40 and 50 cm) while weather data were taken from a station located less than 1 kilometers from the test field. The experimental area has also a homogeneous soil with a sandy loamy texture and about 2% of organic matter (see Table 4.5 for soil properties).

Soil drainage promotes infiltration requiring frequent irrigation. The plant is vulnerable to dehydration and the soil must therefore always be kept damp avoiding water stagnation that would lead to the rot of the fruit.

Loam	Clay	Sand	Organic Matter	ρ_{bulk}
42.1%	38.5%	19.4%	2.1%	1.4 g/cm^3

Table 4.5: Soil physical properties.

In Figure 4.28 soil moisture measurements over the data acquisition period are plotted. The oscillation that can be seen in the first two proximal probes are due to the drip irrigation that was provided during the summer months.

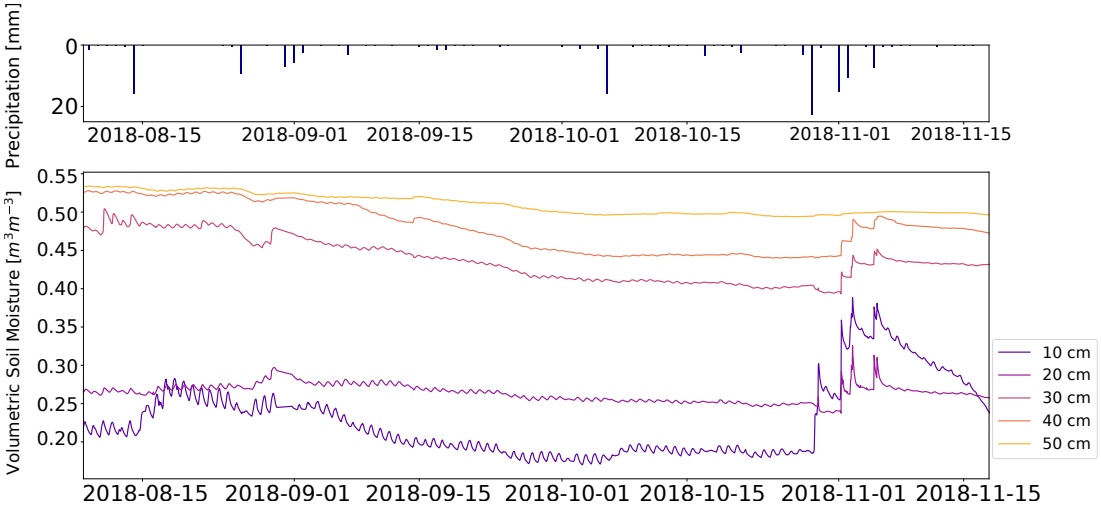

Figure 4.28: (Top panel) Comulative precipitation. (Bottom panel) Sentek soil moisture measurements at five different depths over the data acquisition period.

A particularity of this site is the presence of a very shallow saturated zone. The territory is a reclamation area, kept dry thanks to water pumps that operate 24 h a day. This creates a very shallow saturated zone that reaches 50 cm deep. This is clearly visible from Figure 4.28, where the soil moisture sensors from the Sentek probes reaches 50% of the water equivalent at a depth of 50 cm. Furthermore, the owner of the property has underlined how the nearby reclamation canal (identified in Figure 5a with the light blue line) creates infiltrations in the field and this creates problems of asphyxiation of the plants due to too much water in the soil. The end of the vegetative season for the orchard is in September and the irrigation drip was stopped on September 1. September and October were relatively dry months with a rainfall of 60 mm. From October 27$^{\text{th}}$ a rainy period significantly increased the soil moisture.

4.4.2 Particles counts

The acquisition software discriminates between neutrons (thermal and fast), gamma-rays and muons integrating counts every hours. A moving average of 12 hours was done in order to avoid high frequency variation. The obtained time-series are plotted in Figure 4.29.

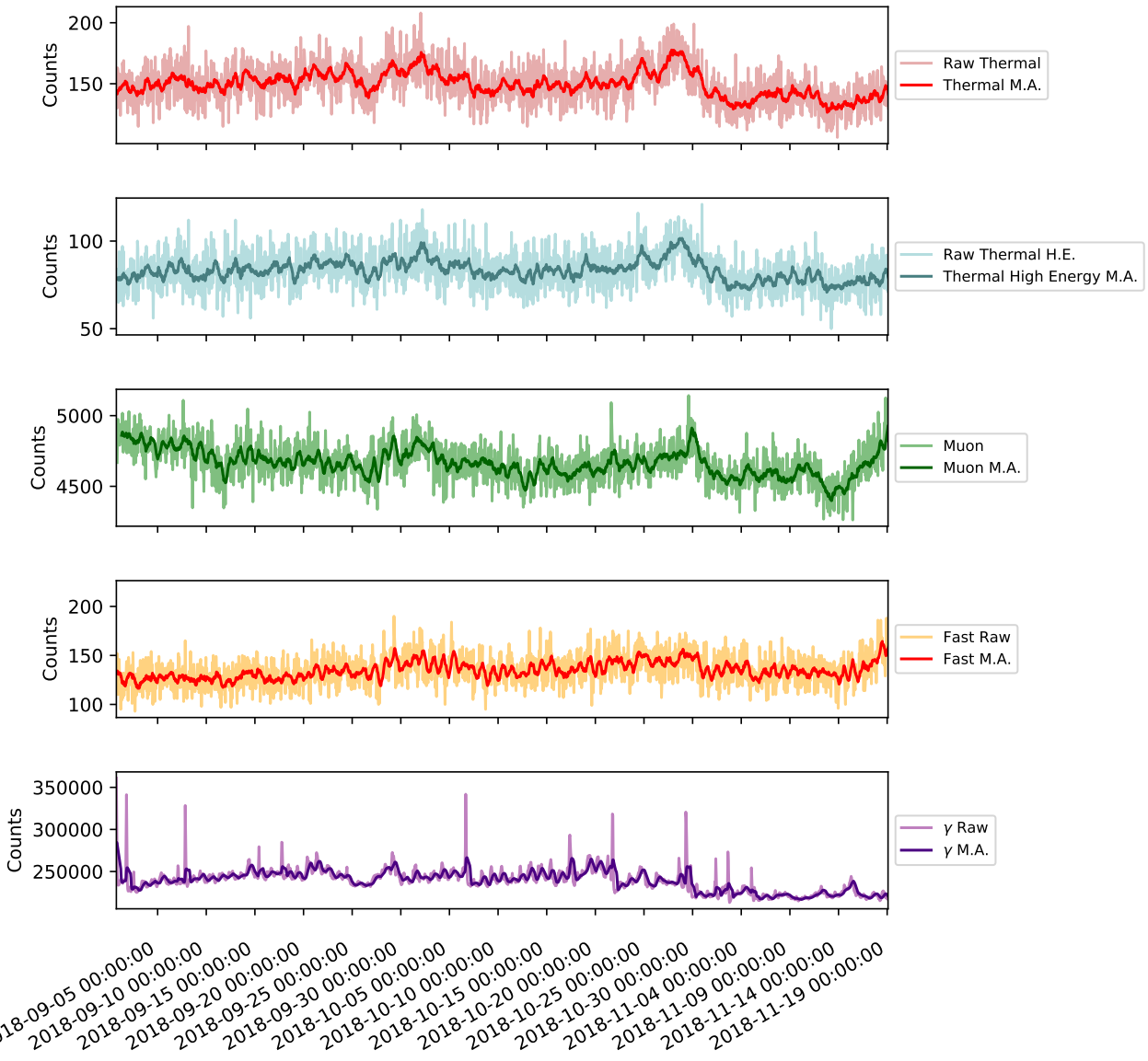

Figure 4.29: Particle counts between September and November 2018.

4.4.3 The comparison procedure

As stated before the goal of the experiment was to compare CRNS estimate using this new detector assembly with point-scale measurement. Since CRNS is able to measure the water content in the first 20–70 cm of the soil depending on soil moisture; higher the water content and less is the depth sensitivity, because wet soil has a larger moderation power for neutrons. Since five different probes are available a weighted average has to be done in order to follow CRNS depth sensitivity. This can be accomplished following a weighting procedure proposed by [Schrön, 2017]. When having different soil profiles P at various distances r_P from the CRNS probe and each of them has different soil moisture measurements at different length L of depth d_L. Let's call $\mathrm{wt}(\theta_{P,L}, w)$ the weighted average:

$$\mathrm{wt}(\theta_{P,L}, w) = \frac{\sum_i \theta_i w_i}{\sum_i w_i} \tag{4.9}$$

The weighted procedure is defined by the following algorithm:

1. Set the initial guess for the weighted soil moisture $\langle\theta\rangle$ by averaging over all depth and profiles setting all weights to 1: $\langle\theta\rangle = \mathrm{wt}(\theta_{P,L}, 1) \equiv \langle\theta\rangle^{\mathrm{equal}}$.
2. Computing the penetration depth D_p for each profile following what seen in Section 2.8: $D_P \equiv z^*(\langle\theta\rangle) = \frac{5.8}{\langle\theta\rangle + 0.0829}$.
3. Vertical average the soil moisture over layers L in order to get a weighted average for each profile P.
4. Horizontally average the profile θ_P.
5. Use the new value for $\langle\theta\rangle$ and reiterate 1-4 until convergence.

Since only one profile was available the weighting procedure has to be carried out only for the different depths. The penetration depth D_p can be computed following the approach proposed seen in Section 2.8. The obtained value for $\langle\theta\rangle$ can be compared with the $\theta(N)/\rho_{\mathrm{bulk}}$ estimated via CRNS.

4.4.4 Results

Raw thermal neutrons counts were first corrected by atmospheric pressure. In Figure 4.30 thermal neutrons counts are plotted togheter with the atmospheric pressure and the precipitations during the whole acquisition period.

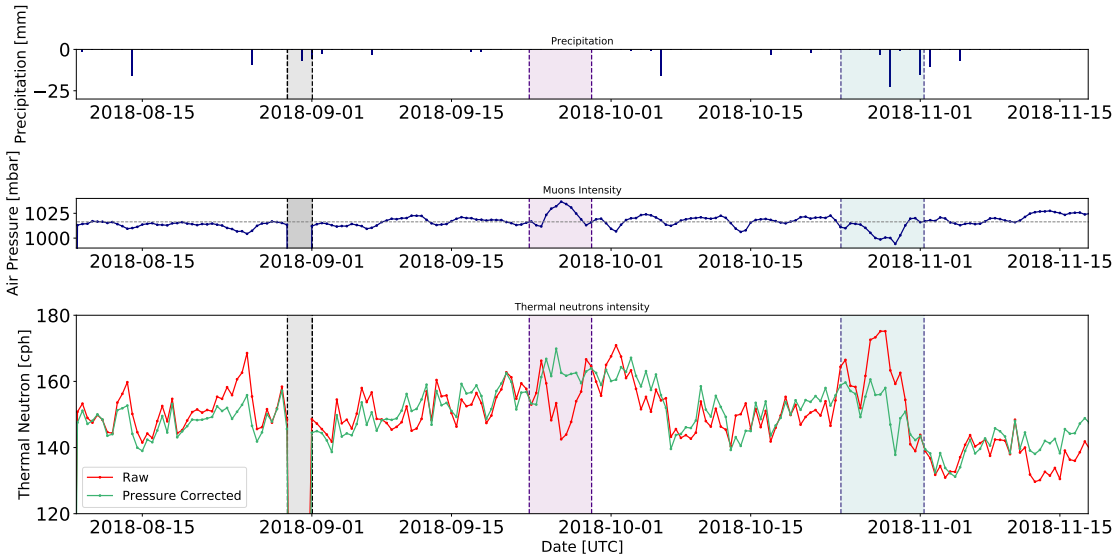

Figure 4.30: Effect of air pressure correction on thermal neutrons counts.Time series over the measurements period: (Upper panel) Precipitations, (Middle Panel) Air pressure (the reference p_{ref} value is highlighted by the gray dashed line), (Bottom Panel) raw and pressure corrected thermal neutrons counts. Black shaded area refer to a stop in the acquisition system of a day between August 30^{th} and 31^{st} while the purple and the blue shaded areas highlight regions where the correction is important (see text).

The importance of this correction can be seen when looking at the purple and the blue highlighted region of the plot. In the purple one, raw thermal neutrons (red line) counts, exhibit a drop . Nevertheless, by looking at the precipitation this drop in the counts is not related to a rainfall event but is the effect of a variation in the air pressure of 2% with respect to the reference value which were set to $p_{\text{ref}} = 1016.4$ mbar. On the other hand, looking at the region highlighted in blue,is possible to see that raw counts are increasing. This increase is due, as in the previous case, to a change in pressure that would lead to a decrease in estimated soil moisture. As we can see from the figure, however, in the highlighted region there are rainy events that have certainly led to an increase in soil moisture. Once corrected (green line) these spurious effects are removed. Later on we refer to this pressure corrected signal as:

$$N_p = N_{raw} \cdot C_p \tag{4.10}$$

where C_p is defined in Equation (2.8). The barometric coefficient used was $\beta = 0.0076$ [Schrön et al., 2018].

Subsequently, counts were corrected for air humidity (orange line) obtaining:

$$N_{p,h} = N_{raw} \cdot C_p \cdot C_h \tag{4.11}$$

where C_h is defined in Equation (2.11). Reference value used by correction functions were set to $h_{\text{ref}} = 12$ g/m^3. In Figure 4.31 N_p and $N_{p,h}$ are plotted togheter with the air humidity from the nearby weather station.

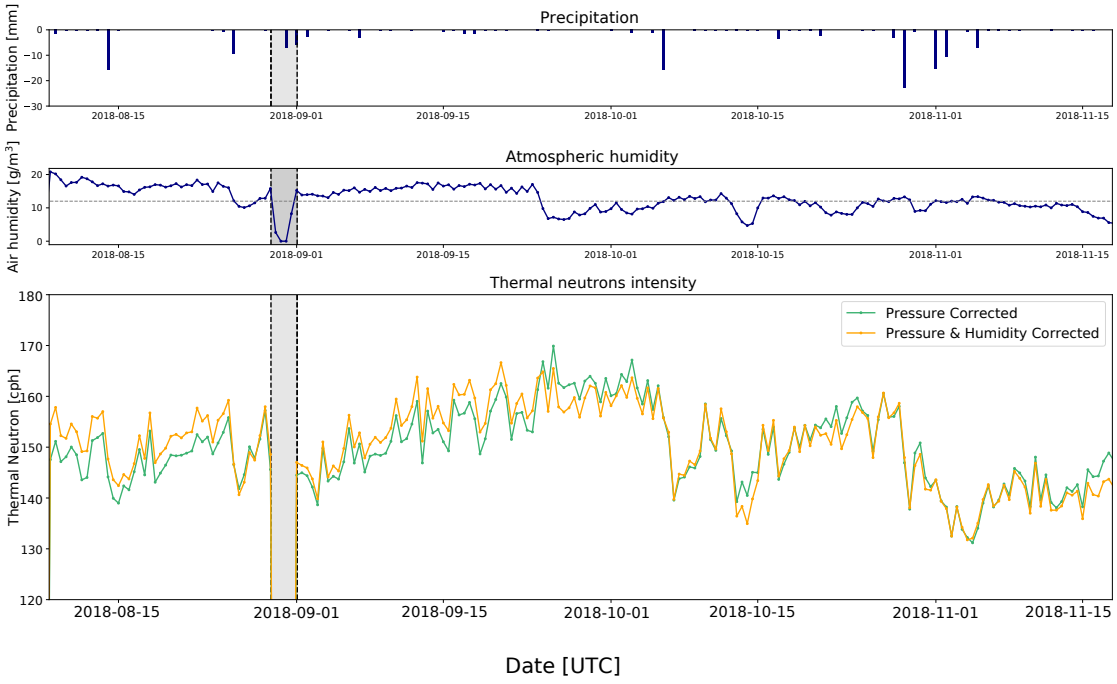

Figure 4.31: Effect of air humidity correction on thermal neutrons counts. Time series over the measurements period: (Upper panel) Precipitations, (Middle Panel) Air humidity (the reference p_{ref} value is highlighted by the gray dashed line), (Bottom Panel) N_p and $N_{o,h}$. Black shaded area refer to a stop in the acquisition system of a day between August 30$^{\text{th}}$ and 31$^{\text{st}}$.

Finally the primary cosmic-rays incoming variation correction was done, using Equation (2.10), obtaining:

$$N_{p,h,I} = N_{raw} \cdot C_p \cdot C_h \cdot C_I \tag{4.12}$$

where inside the correcting function for the incoming, muons were used, instead of neutrons monitor data, as a proxy for primary cosmic-rays flux variations [De Mendonça et al., 2016]. This is an huge advantage with respect to traditional ^{3}He counters which require offline analysis in order to estimate soil moisture; measuring muons, instead,

allow for continuosly monitoring of soil water content making this new detector appealing for precision agriculture application.

However, before could be used for such correction, raw muons counts have to be pressure corrected following the same procedure seen for thermal neutrons. The barometric coefficient, although, is different for muons.

This can be seen in Figure 4.32 where fluxes, for cosmic-rays particles, where plotted as functions of the altitude. Withing the first 10 kilometers the CRs flux is dominated by muons. From this figure it is important to note the difference between the slope of the of muons neutrons fluxes in the first kilometers of altitude. The attenuation length, which is the inverse of the barometric coefficient, is different for muons and neutrons. Thus, since the barometric coefficient, β, is the inverse of the attenuation length, the one used for correcting muon counts should be smaller than the value used for the correction of thermal neutrons.

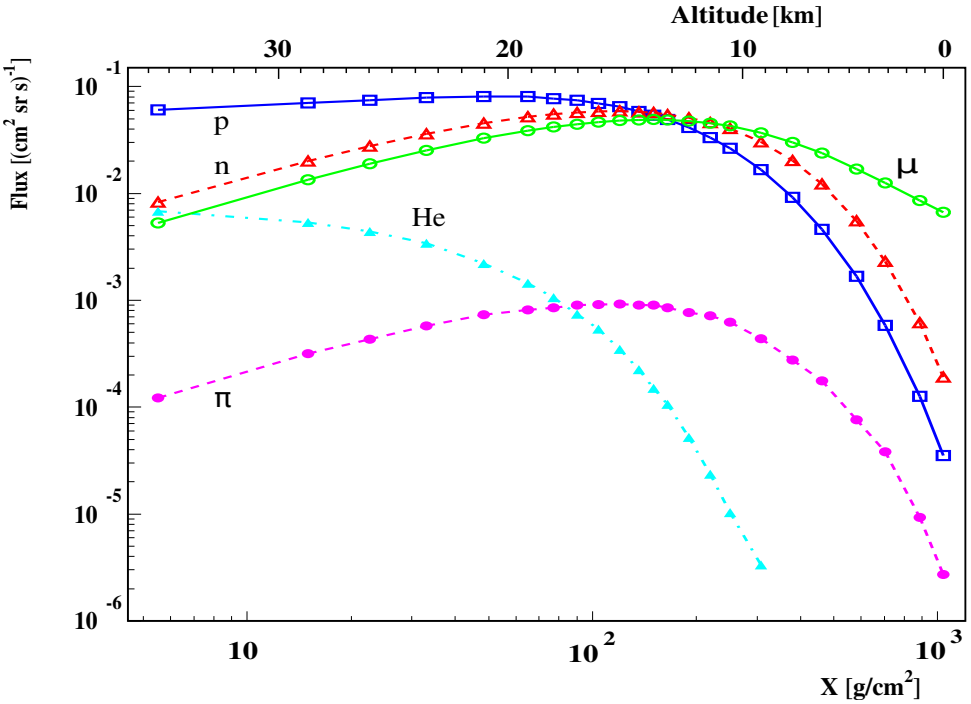

Figure 4.32: Total fluxes of muons, pions, protons, neutrons and helium nuclei as a function of atmospheric depth and altitude above sea level.From [Hansen et al., 2003]

Following [Paschalis et al., 2013], the change in the muon counts is related, through the barometric coefficient, to a change in the local pressure:

$$M = M_0 e^{-\beta(P-P_0)} \tag{4.13}$$

where P_0 is the reference pressure corresponding to a muons counts of M_0.This can be written in the logarithmic form:

$$\ln\left(\frac{M}{M_0}\right) = -\beta\,(P - P_0) \tag{4.14}$$

that can be used to obtain the barometric factor for muons. An important remark is that Equation (4.14) is valid only if primary incoming variation is negligible [Paschalis et al., 2013]. For this reason, muons counts acquired during August, in which the primary incoming is almost stable[1], were used for computing the barometric coefficient. A $\beta = 0.0019 \pm 0.0002$ was obtained, result is plotted in Figure 4.33.

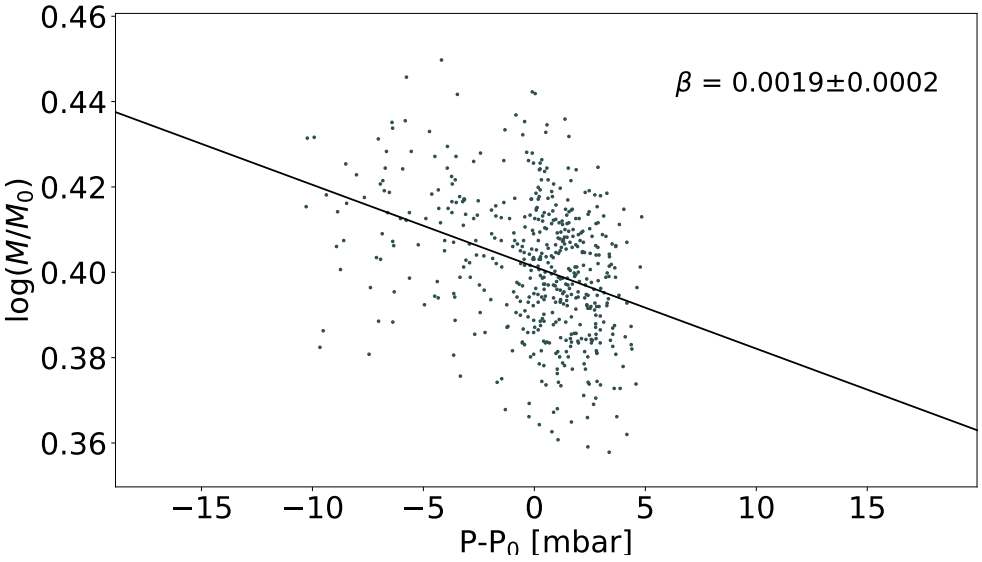

Figure 4.33: Correlation between muons counts and atmospheric pressure.

[1]This can be seen from JUNG primary incoming data. Data can be found at the Neutron monitor dataBase website `http://www.nmdb.eu`

The comparison between Finapp's muon counts and the neutron monitor housed on top of the Sphinx Observatory Jungfraujoch is plotted in Figure 4.34 [Steigies, 2009]. Data from this station were chosen since is the closest and with the highest efficiency respect to the installation point.

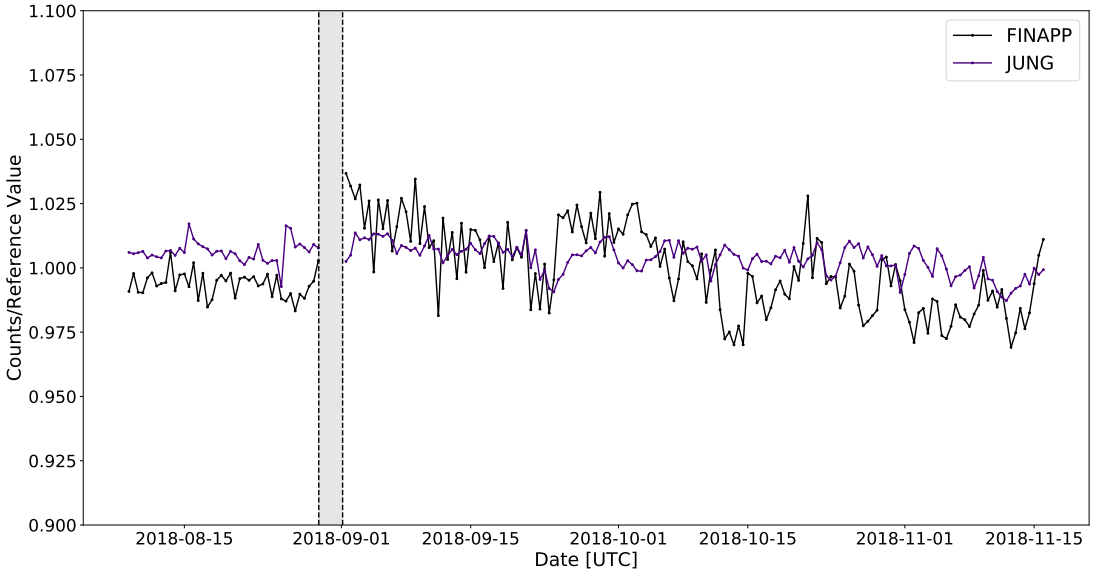

Figure 4.34: Comparison between integrated measured obtained by Jungfraujoch counts and the Finapp muon counts. The detector at Jungfraujoch is a standard 18-IGY neutron monitor and is placed at 46.55° N,7.98° E with an altitude of 3570m asl.

In Figure 4.35 $N_{p,h,I}$ is plotted using muons flux measured by Finapp and data from neutron monitor station. The two different correction have an average variation of the 1% with occasional peaks of 2.5%. Further studies on this type of correction are underway.

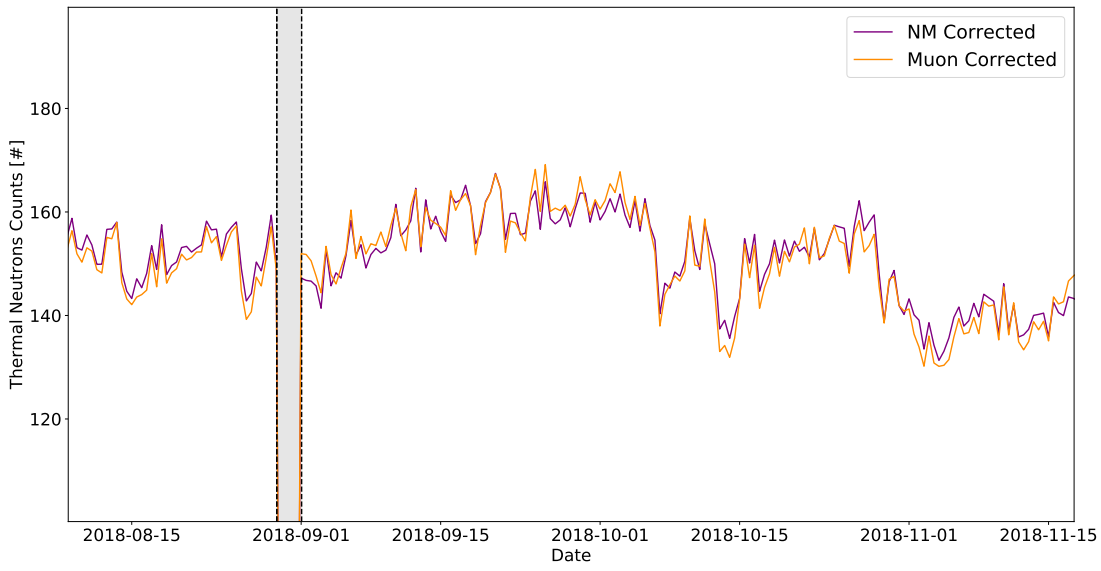

Figure 4.35: Comparisong between $N_{p,h,I}$ obtained using Muons and Neutron Monitor data (NM).

In Figure 4.36 $N_{p,h}$ and $N_{p,h,I}$ are plotted togheter with the muons flux which was almost stable during the measuring period with fluctuation of order of 2%. The reference value was set to $I_{\text{ref}} = 4667$.

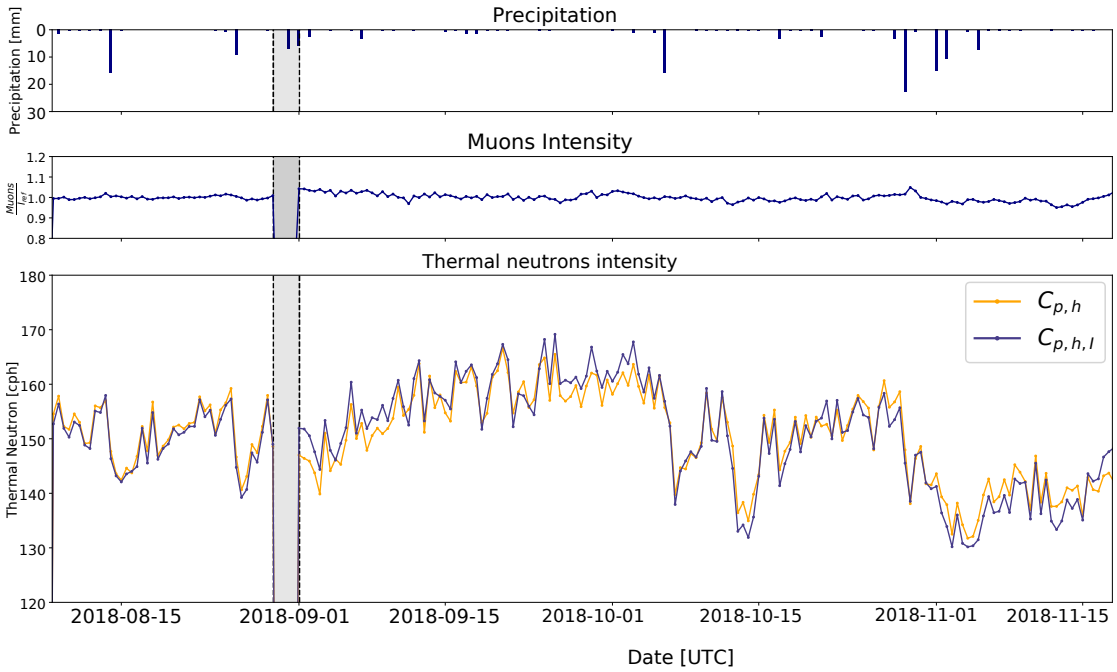

Figure 4.36: Effect of primary cosmic-rays variations correction on thermal neutrons counts.Time series over the measurements period: (Upper panel) Precipitations, (Middle Panel) Finapp muons intensity, (Bottom Panel) N_p and $N_{o,h}$. Black shaded area refer to a stop in the acquisition system of a day between August 30^{th} and 31^{st}.

Using $N_{p,h,I}$ was possible to retrieve the soil moisture information via the empirical formula:

$$\theta(N) = \left(\frac{0.0808}{\frac{N}{N_0} - 0.372} - 0.115 - \theta\text{offset} \right) \cdot \rho_{\text{bulk}} \tag{4.15}$$

Figure 4.37 shows the averaged soil moisture from the Sentek probe and the neutron derived soil moisture from Finapp; the lower part of the figure shows the cumulated precipitation with a 24 h interval. Focusing attention on the Finapp data, it is possible to notice a very good agreement between precipitation and soil moisture. Every rain event corresponds to an increase in volumetric soil moisture. Only the events on October 13 report an increase of soil moisture without any precipitation. This increase is probably due to infiltration from the near reclamation canal, that increased soil moisture in the footprint of our probe, as suggested by the property owner. On the contrary, there are some differences if we compare Finapp with point-scale probes. First of all, during

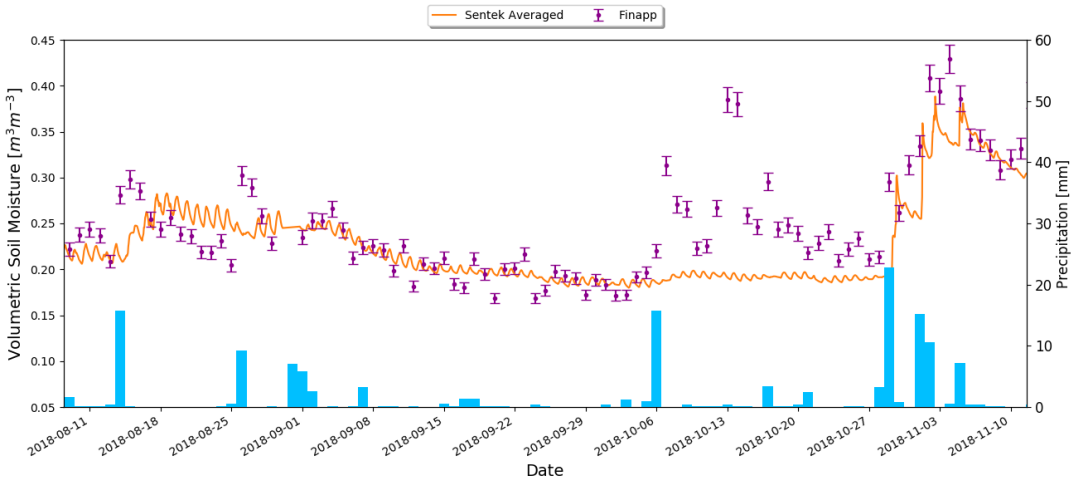

Figure 4.37: Volumetric soil moisture from Finapp (magenta) and average soil moisture from Sentek (orange); for details see the text. Daily rain is reported in the bottom part of the plot.

the irrigation period the point-scale measurements are less sensitive to precipitation because the drip irrigation biases the point measurement due to a heterogeneous water distribution. In September there is good agreement between the Finapp and Sentek probes; the soil moisture decreases in both cases due to the dry period. In October there is again some discrepancy, probably due to a malfunction of the Sentek probe. The property owner notes that in October the probes are no longer checked daily because the data is no longer used, and periods of malfunctioning occur due to various technical problems (power, batteries, data transmission, etc.). In November the agreement is good again and both the Sentek and CRNS probes respond to precipitation in the same way.

This experimental test showed how it is possible to use this new detector for CRNS-based applications. The efficiency as an epithermal neutrons counter is 55%, in respect to the commercial CRS-1000 from Hydroinnova and this is the major drawback with respect to ^{3}He proportional counters [Stevanato et al., 2019].

Chapter 5

Improving the Lagosanto system

In this chapter is described the characterization of a new plastic scintillator for fast neutrons/γ discrimination with the view of improving the detector described in the previous chapter. Moreover, a custom online analysis software were developed in order to make the analysis described in the previous section automatic.

5.1 Characterization of a new fast neutrons detector

5.1.1 The EJ-276

EJ-276 is a new plastic scintillator with improved fast neutrons/γ discrimination. This detector has an excellent physical hardness superior to that of standard plastic scintillators and is characterized by a good stability of scintillation and optical characteristics (see Table 5.1).

Light output	56 (% Anthracene)
Wavelength of maximum emission	425 nm
No. of H Atoms per cm^3	4.546
No. of C Atoms per cm^3	4.906
No. of Electrons per cm^3	3.533
Density	1.096 g/cm^3
Approx. mean decay times of first 3 components	Gamma Excitation 13,35,270 ns
	Neutrons Excitation 13,59,460 ns

Table 5.1: EJ-276 Properties.

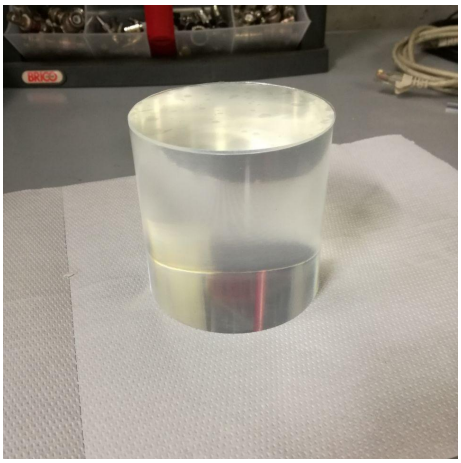

Figure 5.1: EJ-276 plastic scintillator.

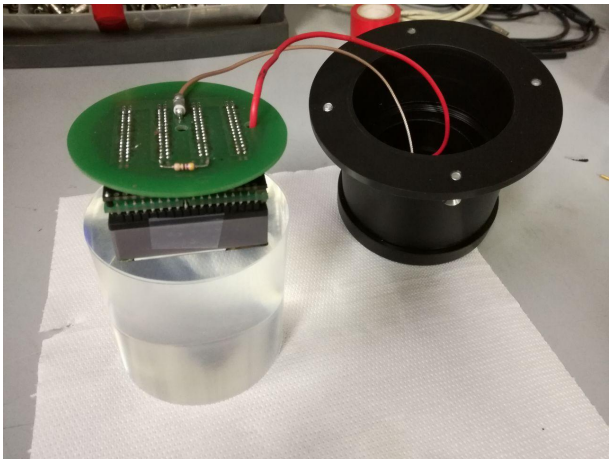

Figure 5.2: EJ-276 assembled for characterization.

5.1.2 Experimental procedure

The calibration of the energy response of the detector, was performed using a ^{22}Na γ source. The main goal was to compare the PSD capabilities of this new scintillator with respect to the previous one. With this aim PSD parameters, qshort and qlong, were optimized in order to search for that particular set among them, which maximizes the capacity of neutron-γ discrimination of the detector. This optimization was carried out using measurements in presence of a ^{252}Cf source place at about 30 cm from the detector for half an hour.

Energy calibration

The calibration was done following the same procedure seen for EJ-299-33A. The optimal Gaussian smeared spectra are plotted in Figure 5.3 and 5.4 for both 240 and 1062 keVee Compton edges. The shift of the Compton edge associated to the σ was used to calibrate the detector. Values are shown in Table 5.2. It is worthing to notice that resolution is slightly worse than the EJ-299-33A.

The obtained calibration function is:

$$E(\text{qlong}) = a \cdot \text{qlong} + b \qquad a = 0.019 \text{ keVee/qlong}, \; b = 4 \text{ keVee} \tag{5.1}$$

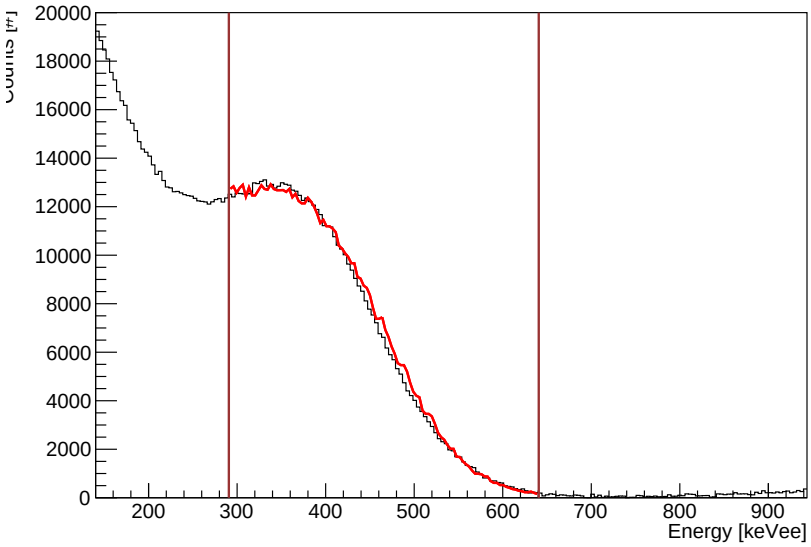

Figure 5.3: Compton edge at 340 keV.
The optimal σ is 75 keVee.

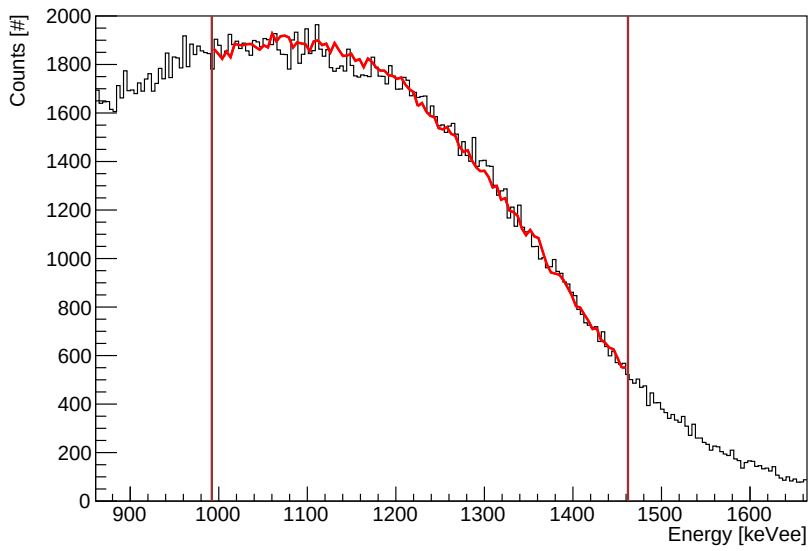

Figure 5.4: Compton edge at 1062 keV.
The optimal σ is 192 keVee.

Photon Energy [keVee]	σ [keVee]	Resolution	C.E. shifting [keVee]
511	75	22%	105
1275	192	18%	242

Table 5.2: σ, Resolution and C.E. shift for EJ-276.

PSD parameters optimization

In order to ensure optimal particle discrimination capabilities the integration gates parameters were optimized. With this aim a figure of merit parameter, called FoM, is defined:

$$\text{FoM} = \frac{S}{\Gamma_e + \Gamma_p} \tag{5.2}$$

where S is the difference between the two Gaussian centroid and $\Gamma_e + \Gamma_p$ is the sum of the two Gaussian full width at half maximum (FWHM). This parameter allows for a quantification of the discrimination capacity. An acquisition of about 15 minutes with ^{252}Cf was used. The first step is to select all the events with a PSD parameter lower than 0.6 between 200 and 700 keVee, in order to neglect noise signals. Using the selected event a set of PSD distribution, one for each configuration of qlong and qshort, was obtained (see Figure 5.5). The distribution was then fitted with a sum of two Gaussian function allowing for the computation of the FoM.

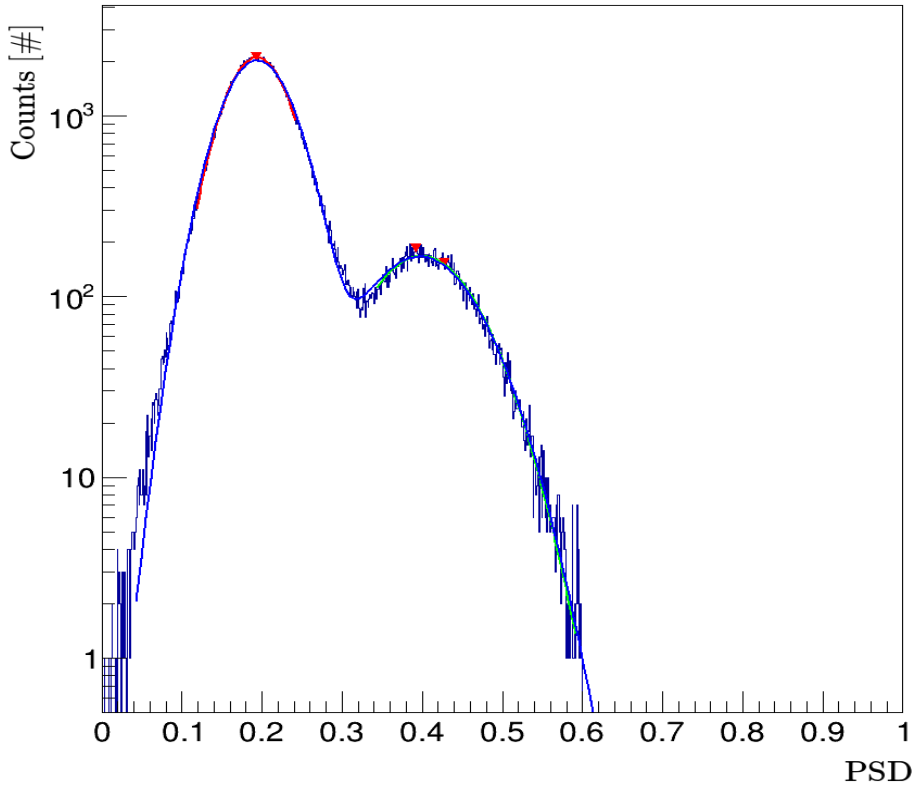

Figure 5.5: Figure of Merit for events with PSD< 0.6 and energy between 200 and 700 keVee.

In Figure 5.6 FoM is plotted as a function of the long gate for different short gate values The FoM was compute considering only events with an energy between 200 and 700 keVee. What is observed is that discrimination capacity increases with the increase of the long integration gate up to a certain value where saturation occurs. Observing a saturation in this plot is fundamental because, if not present, it indicates the incapacity of the total integral to collect the slow component of the signals. For fixed values of the long integration gate, on the other hand, the short gate influences the ability to discriminate, giving rise to these parallel distributions. The optimal short gate integration was found to be 19.

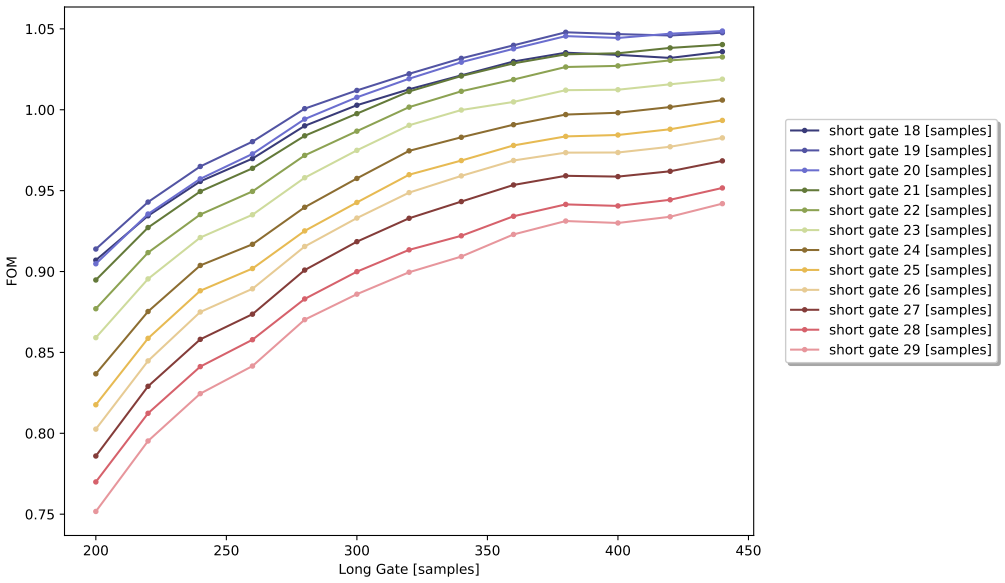

Figure 5.6: Figure of Merit as a function of long gate for different short gates.

In Figure 5.7 is shown the PSD plot for EJ-276 for ^{252}Cf source. The red segmented line is the discrimination line: if an event lie above this line is classified as neutron otherwise is classified as γ event. This line was built following the following procedure: first of all the bidimensional distribution is splitted in thin energy slices of 50 keVee. At each of these slices is associated a point of the red line.

Each slices are projected to the y axis obtaining a unidimensional distribution (see Figure 5.8). With this distribution a Gaussian fit, around the γ region, was done finding mean and σ. With these information is possible to compute the polinomial line:

$$p_i = \left(\frac{\mathrm{E_{max}} + \mathrm{E_{min}}}{2},\ M_i + k\sigma_i \right) \tag{5.3}$$

where M_i is the mean while σ_i is the standard deviation of the i^{th} slice. The parameter k controls the purity of the discrimination. The value of k was set to 3.

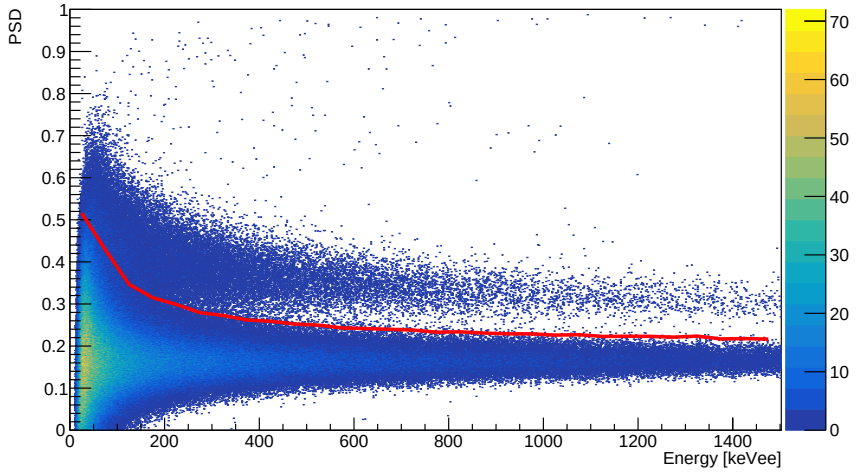

Figure 5.7: PSD-Energy plane distributions. Events collected with EJ-276 using a ^{252}Cf source.

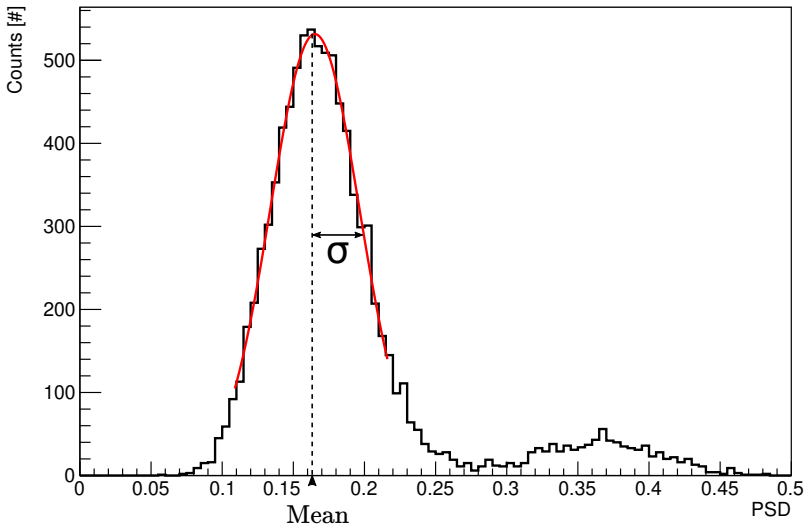

Figure 5.8: Unidimensional distribution of PSD for event within 350 and 400 keVee.

5.1.3 PSD Comparison

With the aim of comparing the discrimination capacity of EJ-276 and EJ-299-33A the FoM as a function of the energy threshold was computed. Before doing this is necessary to optimize the discrimination parameters for both detectors. Obtained results are plotted in Figure 5.9. From this plot it can be seen the discrimination performance gain below 700 keVee. The improvement is of 4% above 300 keVee of energy threshold. Although, FoM below 300 keVee is more important since is the point where the two distributions are mixing. EJ-299-33A has a better FoM under 300 keVee this means a higher efficiency in counting neutrons.

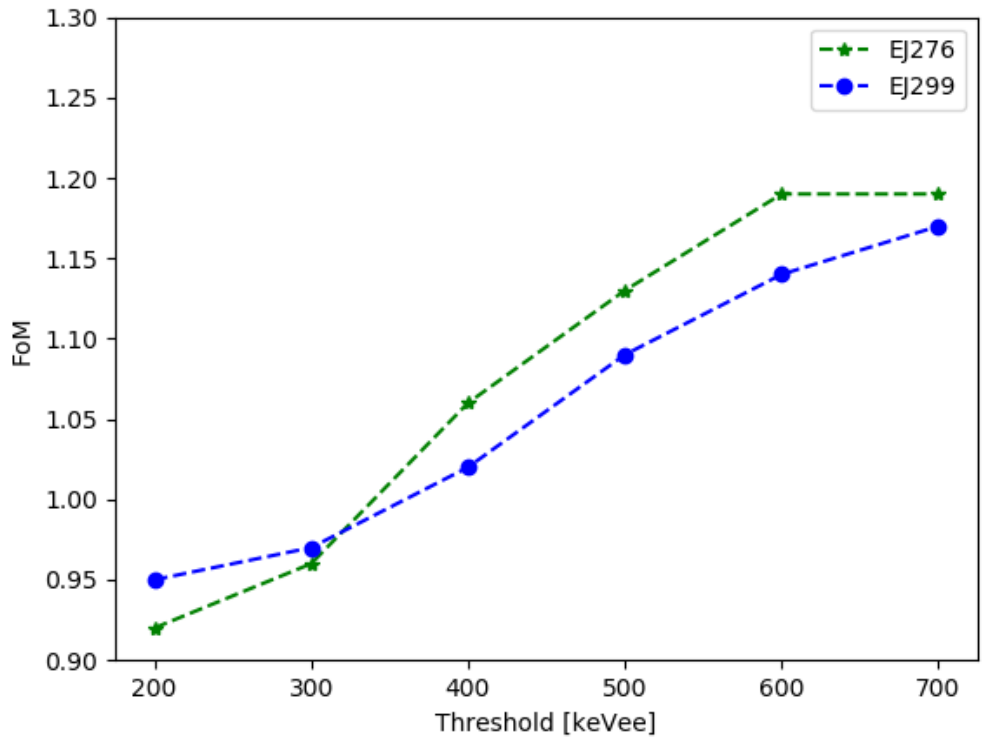

Figure 5.9: Comparison between the FoM as a function of the energy for EJ-276 and EJ-299.

5.2 Online analysis software

The other improvement to the Lagosanto system was the development of an online analysis software which has to reproduce the analysis described in Chapter 4.

5.2.1 Finapp Code

Finapp analysis code was developed, following the distributed computing approach[1], as a set of different programs each of them handling a different task. The communication between them relies on different type of sockets. Code was developed in C (following the C99 standard) and C++ (following the C++11 standard). Socket handling was done using a messaging library called ZeroMQ [Hintjens, 2013]. ZeroMQ is an open-source messaging library which make easier implement distributed system providing different messaging sockets that carry messages across TCP and other protocols. With this library is easy to connect sockets with different communication patterns[2] allowing for optimal information transfer.

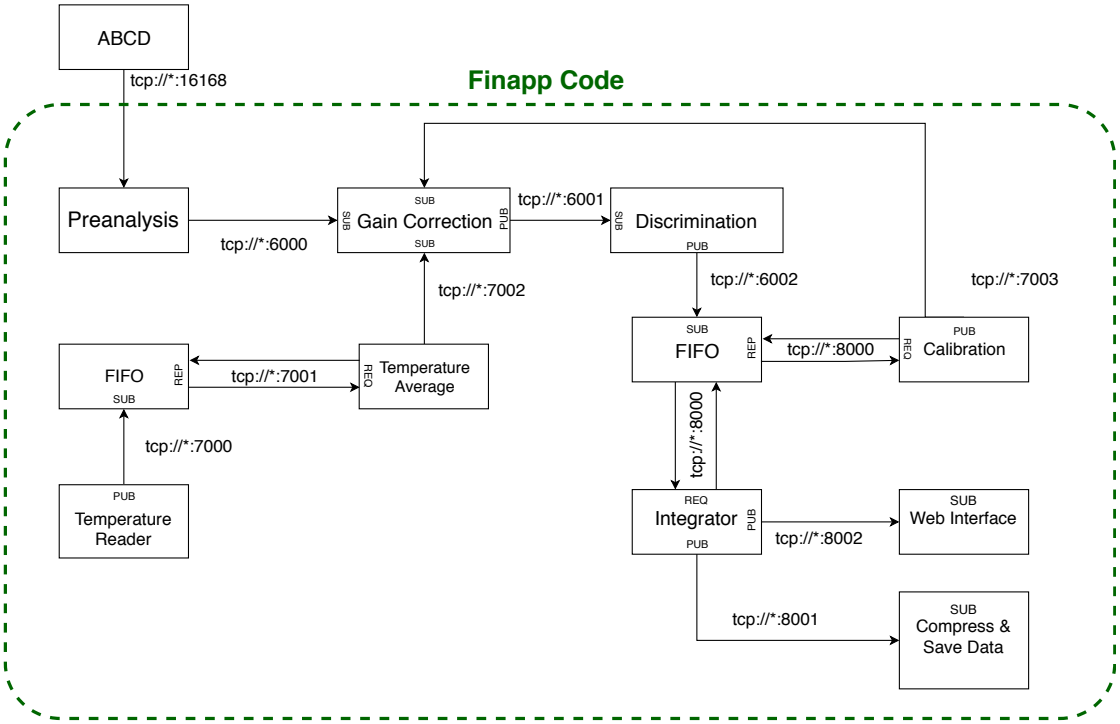

Figure 5.10: Finapp analysis distributed software.

[1] See Appendix A for more detail

[2] More information on the used patterns are reported in Appendix A

The developed system is represented in Figure 5.10 and is composed by the following components:

- **Preanalysis**. This module compute a set of features from the waveform which are used in order to discriminate between particles.
- **Temperature Reader.** Reads temperature values from a sensor. The read values are streamed towards a FIFO unit.
- **Temperature Average.** Averages temperatures between a given time window and stream the value to Gain correction unit.
- **Gain Correction.** Uses the temperature and the normAVG factor in order to corrected the gain as described in Section 4.3.
- **Discrimination.** This module use different filters in order to discriminate different radiation events.
- **FIFO.** Memory module able to store data within a given time window.
- **Calibration.** Implements the procedure described in Section 4.3.
- **Integrator**. Integrates counts every hour.
- **Web Interface.** Graphical user interface which allows for the real time visualization of particles counts.
- **Compress and save data.** Save data in a compress format to the local SD.

As showed in the code block diagram, Finapp code is binded to the acquisition software[3] [Fontana et al., 2018]. Acquired waveforms are streamed towards the preanalysis block which, in turn, extracts different features from the waveforms. Energy and PSD parameter are computed within this module. A set of other features are computed in order to discriminate between particles and noise events:

- Saturated. Boolean flag that check if the signal is saturated or not.
- Curve length.
- Risetime. Number of samples between 10% and 90%.
- Pile up. Pileup events are events in which etcetc.
- Bin future.
- Risetime.
- Minimum and Maximum of the signal.

[3]ABCD - a distributed data acquisition system : https://gitlab.com/cristiano.fontana/abcd

- Index of the Minimum and Maximum of the signal.
- Thermal neutron tail and front.

The next step is the **Gain Calibration** module which implements the corrections seen in Section 4.3. In order to do this it needs a properly average temperature measurement and a realignment parameter[4]. These two information are provided by **Temperature average** and **Calibration**, respectively. A temperature reader subroutine reads temperature measurements provided by a temperature sensor housed inside the probe enclosure. This module stream data to a memory element, FIFO (First In, First Out)[5]. In this type of memory the buffer is managed processing the oldest entry first. Other modules can interface with FIFO through a Request/Reply socket asking for data within a certain time window. The module is developed as a finite state machine A.6. Calibration module mimic the procedure seen during Lagosanto data analysis; every ten minute this module send a request, through a dedicated port, to the FIFO in which events are stored demanding for data within the last hour. With these events, environmental γ spectrum is built allowing for ^{40}K Compton edge tracking. Finally the parameter is send to the gain correction module. As can be seen from the figure this calibration module introduce a control feedback in the system. After being corrected events are ready to be discriminate by the apposite module which use the features computed within the preanalysis one in order to classify events. Once discriminated events are sended to a FIFO memory. The **Integrator** module, once an hour, send a request to the event FIFO asking for events acquired in the last hour and computes the counts for each particle type reproducing time series in Figure 4.29.

Calibration and Integrator module are developed as FIFO clients following the finite state machine paradigm. Their underlying structure is the same (see Figure A.7), after connection handling states (Create context, Create Sockets,Bind Sockets) the client start a timer and go in idle mode. When timer reach a given time set by the user the client send to the FIFO a request waiting for data. Once data is received client reach the Compute state, which is the state which differentiate Calibration and Integrator module. When the Compute task is done data are streamed to the respective output sockets and state return to Idle.

[4]This parameter is the so-called *normK* which account for dynodes degradation.
[5]This memory module is part of the ABCD software distribution.

Chapter 6

Conclusions

This thesis aimed to study the possible use of an innovative sensor based on scintillation detectors for the estimation of soil moisture using the Cosmic-rays neutron sensing method. This probe is proposed as an alternative to the current ^{3}He proportional counters used in this context. Because ^{3}He is mainly produced in artificial settings by the decommissioning of nuclear weapons, its price is high, relegating the spread of this technique to research centers.

The first part of the work was to analyze the data collected at the Porto Felloni agricultural company in Lagosanto, between August and November 2018. The experimental campaign aimed to reconstruct the behavior of soil moisture and compare it with the precise measurements provided by the electromagnetic probes. To extract the hourly counts of the various particles, it was first necessary to follow a recalibration procedure to eliminate the variations in the gain of the photomultiplier. These variations, if not removed, lead to an incorrect classification of the particles invalidating the soil moisture estimates. The response was then corrected using temperature and a correction factor that takes into account the position of the Compton edge of ^{40}K. The counts obtained for the various particles have been adjusted using correction functions to eliminate atmospheric variations and primary flow of cosmic rays variations. Thermal neutron counts (relative to the epithermal part of the spectrum) were then translated into soil moisture using the model proposed by [Zreda et al., 2008]. We have therefore reconstructed the trend of the soil moisture which is well correlated with the rainy events; moreover, the data show the limits of the measurements carried out through point-scale probes which are strongly influenced by the soil heterogeneity. The large footprint of the CRNS probe, on the other hand, allows this difficulty to be overcome, making the use of this instrument ideal in the hydrological, meteorological and precision farming fields. FINAPP's ability to measure gamma, muons, slow and fast neutrons is also an

advantage over traditional ^{3}He probes. It has been seen how muon counts can be used, instead of the data provided by neutron monitors, to correct variations in the primary flow of cosmic rays. Moreover, the information on the gamma-rays has recently been shown to be also correlated with humidity but with a smaller footprint cit. [Baldoncini et al., 2019], the analysis of this information will be analyzed in future studies.

Subsequently, to improve the probe, a new plastic detector for γ/Fast neutron discrimination was characterized. The new detector, named EJ-276, produced by Eljen Technology (Sweetwater, TX, USA) was characterized and its discrimination capability compared with the model used in the detector previously analyzed, EJ-299-33A. The characterization part included the calibration in energy through Gaussian smearing and the subsequent optimization of the PSD parameters. Finally, the FoMs of discrimination for the two detectors as a function of energy were compared. The new detector shows an improvement in PSD capabilities over 300 keV, while under this value the former is better. The new detector was assembled, replacing the EJ-299-33A. The new sensor installed for a second experimental campaign, at Casalserugo (PD), in a vineyard (Figure 6.1 and 6.2).

Figure 6.1: Field site (45° 17' 21" N, 11° 54' 13" E).

Figure 6.2: Picture of the assembly.

Finally, the data analysis software was developed. The software was developed as a distributed system consisting of several independent servers that exchange information through dedicated sockets. Each server performs a specific task making it easy to identify any problems and add new features, thanks to the high modularity. Moreover, since it has to be run on a single-board computer, particular attention has been paid to the choice of libraries dependence and performance.

Appendix A

Online Analysis Software

A.1 Distributed computing

The software was developed following a distributed computing approach. This brief review on distributed software follow closely that reported in [Ghosh, 2014]. The logical distribution is based upon the following set of criteria:

- **Multiple processes**. The system is composed by more than one sequential process. Each of these processes should have an independent thread of control.
- **Interprocess communication**. Processes share information between each other through messages exchange. The physical characteristics of the message links will determine the delay between each communication message.
- **Disjoint address spaces**. Processes have disjoint address spaces. This is one characteristic that parallel systems do not have.
- **Collective goal**. Processes usually interact with one another in order to achieve a common goal.

This approach has several advantages which have contributed in recent years to its large-scale deployment. The principal are:

1. **Speed up**. Usually monolithic codes can be speed up by introducing parallelism but this approach do not scale well. With distributed system usually the main problem is subdivided into smaller sub-problems and a different computing node is assigned at each of these sub-task. Following this approach the system is inherently concurrent leading to an enhancing of the computing speed.
2. **Scalability**. This kind of systems scale well since their segmented structure.

3. **Modularity**. Since each computing unit solve only a sub-task the code is easy to maintain. Moreover, the modularity makes easy adding new features.

An important difference to highlight is that between *distributed* and *parallel* systems (see Figure A.1 and A.2). Usually when referring to parallel systems we refer to system in which different processes share information between each other through a shared memory, while, on the other hand, distributed systems are made up of different processes, each of which with its own memory. Is also important to remark the fact that usually, given their private address space, no process is expected to have global knowledge about either the network topology or the system state [Ghosh, 2014].

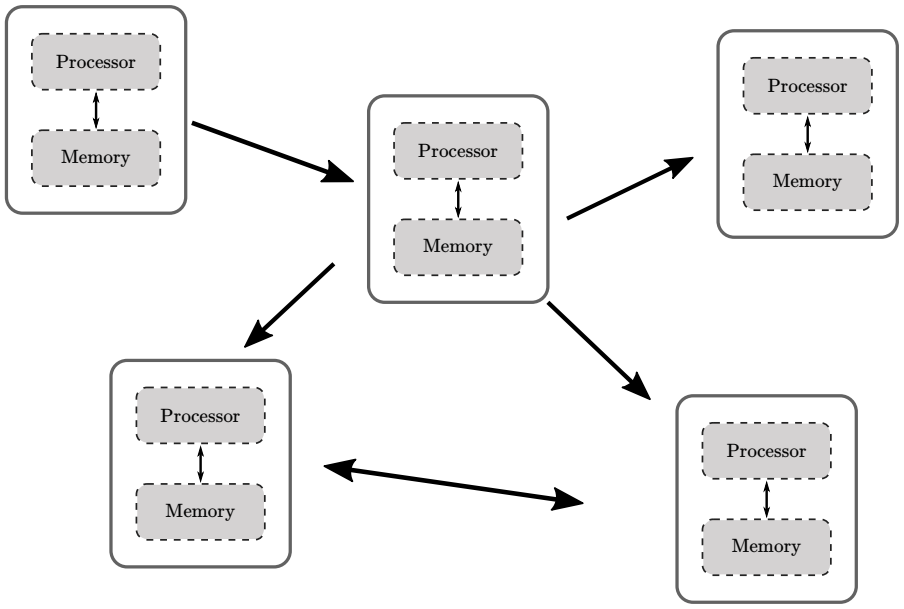

Figure A.1: A distributed system. Each arrow represent a communication link, that can be directed or undirected.

A.2 Communication Links

Communication between each logic unit is the fundamental aspect of distributed systems. Usually the communication can be separeted in two different parts:

- **Networking**. Deals with how processes communicate with one another via the

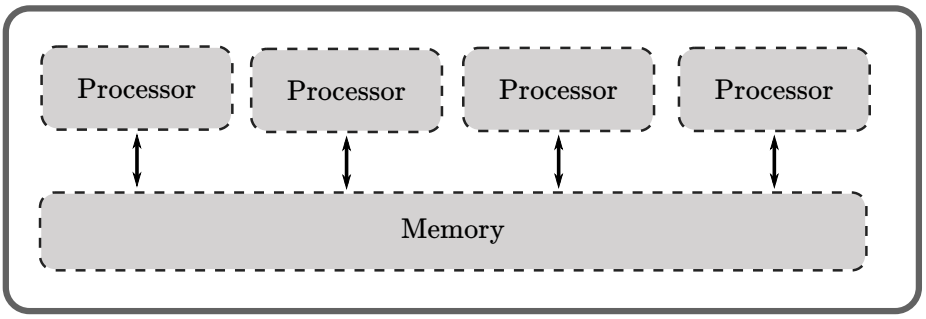

Figure A.2: A parallel system.

different protocol layers.

- **User view**. Abstract high-level view of the interprocess communication medium.

The most diffuse model for developing distributed architectures is the so called *Client-Server Model*. In this model a unit called *Client* request for a certain service and another unit called *Server* reply providing the requested service.

A.2.1 Transport layer protocols

The two most used trasport layer are UDP and TCP:

- **UDP**. User datagram protocol uses IP in order to send and receive data. An important remark is that data packet may not follow transmission order.
- **TCP/IP**. This protocol is responsible for overseeing the reliable and efficient delivery of data between a sender and a reciver. Data lost is possible during the transit. Unlike UDP TCP/IP is a connectionà-oriented protocol so data communication is preceded by a connection establishment phasse and terminated by a connection termination phase. The error handling idea rely on adding a sequence of numbers to the packets before the data transmission and then monitoring the acknowledgement message received for each packet from the destination processes. If the acknowledge message is not received after a certain time delay the message is re-transmitted.

Sockets

Sockets are endpoint that allow for receiving and sending data packets within a node inside a network. They are integrated inside the I/O part of the operative systems like BSD UNIX. Stream sockets use TCP/IP while datagram sockets use UDP. In the course of the years different messages patterns have been developed in order to optimize the

exchange of information between the various nodes of a network. Different situation may require different type of connection and due to this different sockets are available.

Publish/Subscribe pattern

In this type of socket a server, called publisher, is linked to a given IP address specifying its port (e.g. 127.0.0.1:9000). Through this port, messages related to different topics can be sent from the server. The client, called subscriber, can connect to the address associated with the server by subscribing to a specific topic so that when a message related to that topic is sent, the subscriber receives it. Different subscribers can then subscribe to different topics without any problem. As we will see below, the first block of the analysis software subscribes to the *waveforms* topic of the acquisition software, thus, receives only messages containing the digitized waveforms.

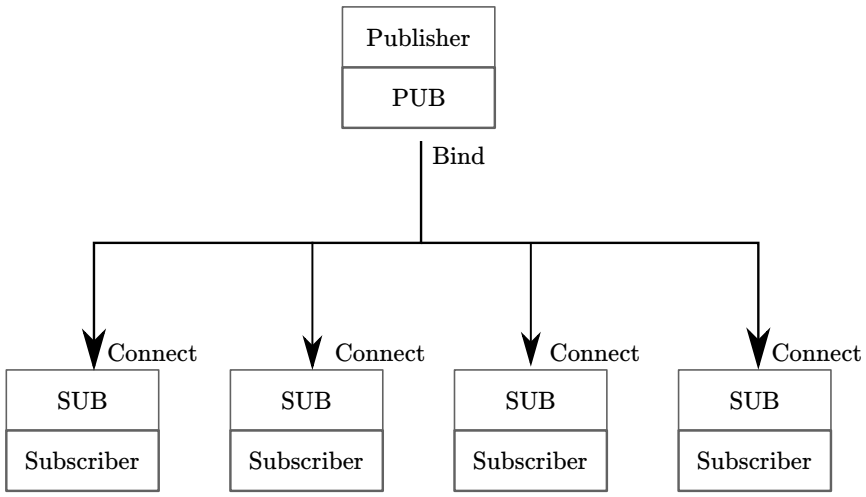

Figure A.3: Pusblish/Subscribe pattern.

Request/Reply pattern

Through this pattern a block can send a request to another requesting a certain service, once received, the request is processed by the destination block. The requesting block waits until a reply is received. In this case, unlike the publisher/subscriber pattern, there is no continuous streaming of data but it must be explicitly requested. This pattern was used to communicate with the system's memory element (the FIFO block).

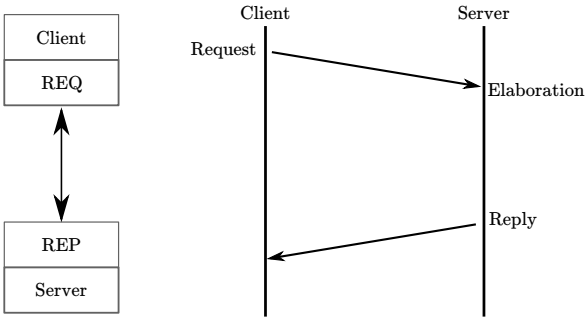

Figure A.4: Request/Reply pattern.

A.3 ABCD

Within ABCD data is transferred using the ZeroMQ messaging library, as it is an agnostic mean of transportation ABCD implements its own serialization protocols. ABCD opted to use PUB-SUB sockets for the data streams and statuses streams, and push-pull sockets for commands streams. High-level data, such as commands and statuses, are deliver using JSON. Moreover ABCD uses custom binary formats for the digitizers data streams. Each PSD event is a 16 bytes binary word with:

- Time stamp - 64 bit unsigned integer;
- Charge short - 16 bit unsigned integer;
- Charge long - 16 bit unsigned integer;
- Baseline - 16 bit unsigned integer;
- Channel number - 8 bit unsigned integer;
- PUR flag - 8 bit unsigned integer, unused.

A waveform has a 14 bytes header with:

- Time stamp - 64 bit integer.
- Channel number - 8 bit integer.
- Samples number (N) - 32 bit integer.
- Gates number (M) - 8 bit integer.

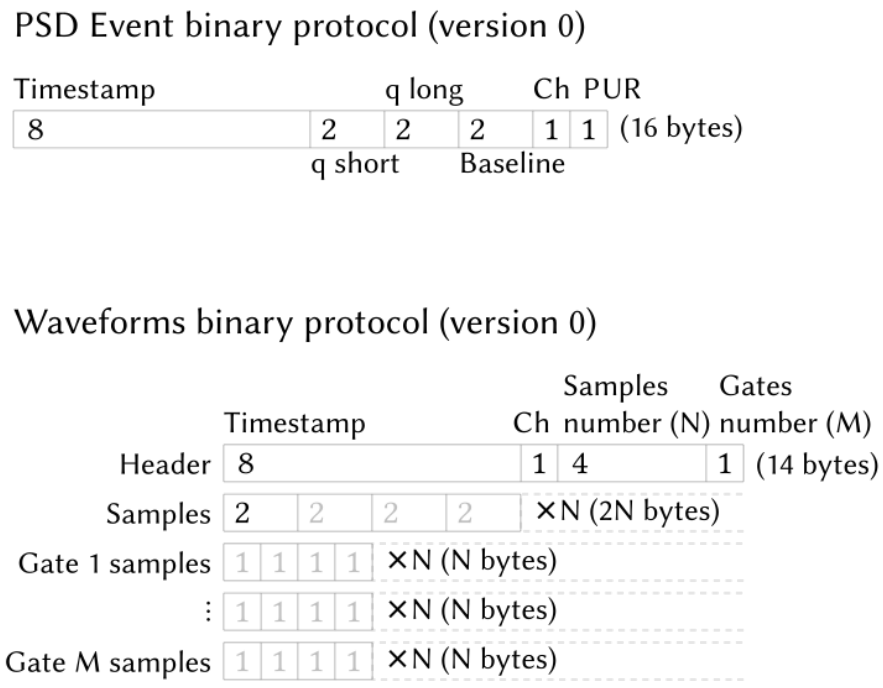

Figure A.5: PSD event and Waveform binary protocols.

Following the header there is a binary buffer of N times 16 bits integers. This buffer contains the digitized signals. After the samples buffer there are M binary buffers, each with N times 8 bits integers. These buffers are the digitizer's integration gates.

A.4 FIFO State Diagram

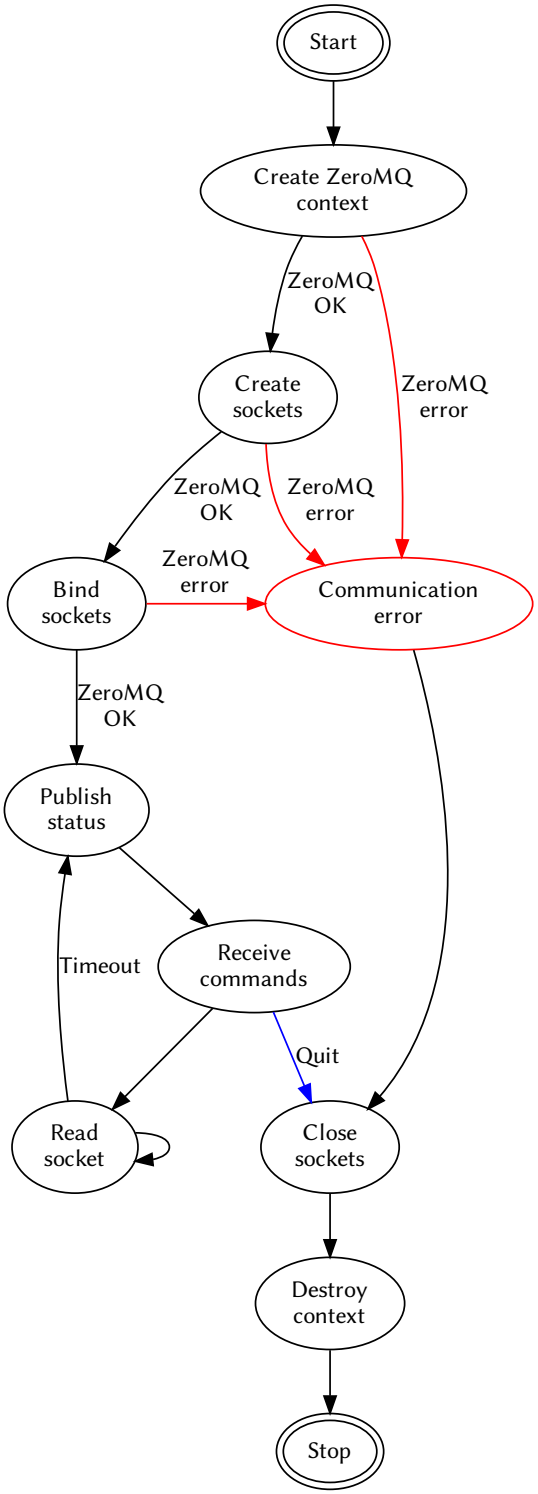

Figure A.6: FIFO finite state machine.

A.5 Calibration and Integrator State Diagram

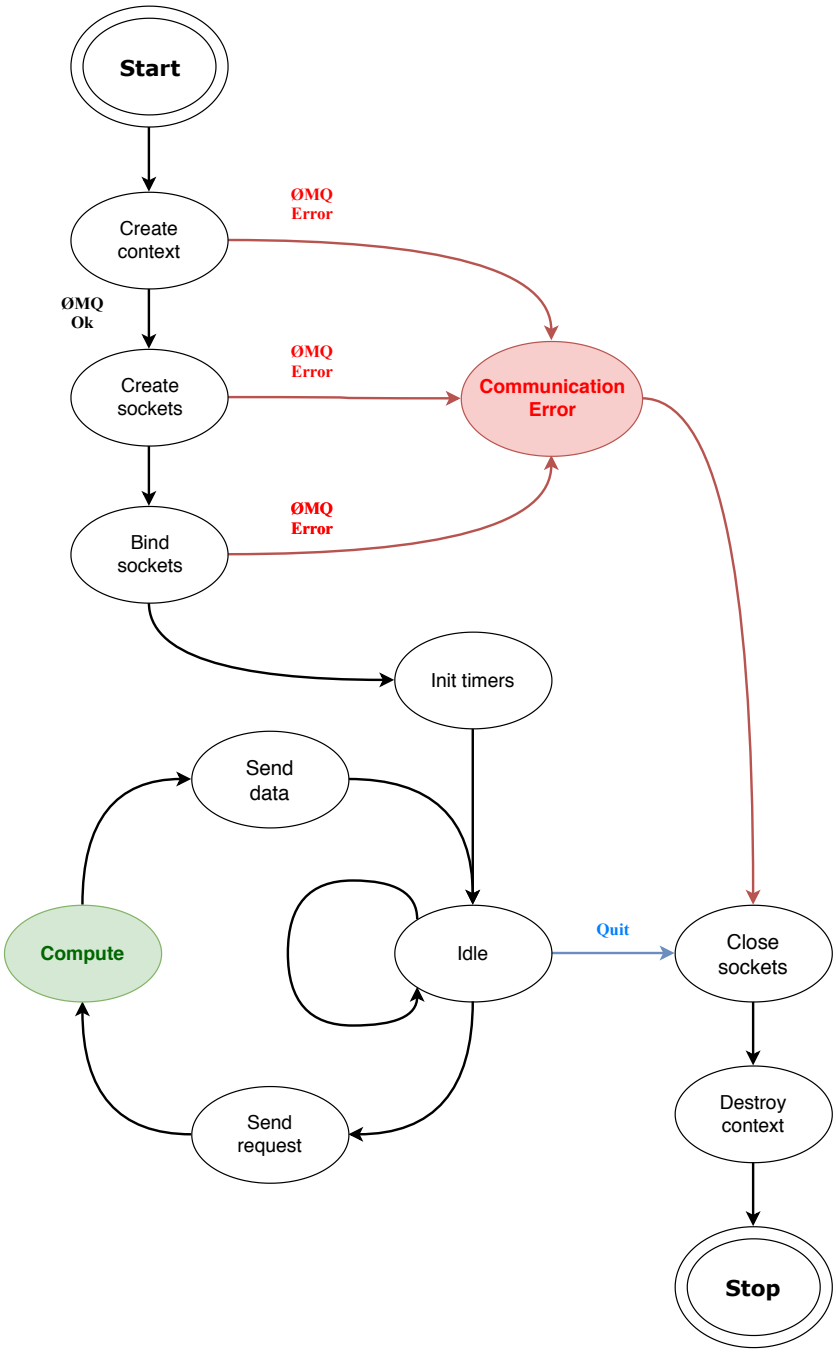

Figure A.7: FIFO Client finite state machine.

A.6 Web interface

Web interface was developed in Javascript using socket.io library [Rai, 2013]. With this library was possible to adapt from TCP socket to WebSocket. Then a server running locally provide to the user the graphical user interface. In Figure A.8 a screenshot of the particles counts dashboard is shown.

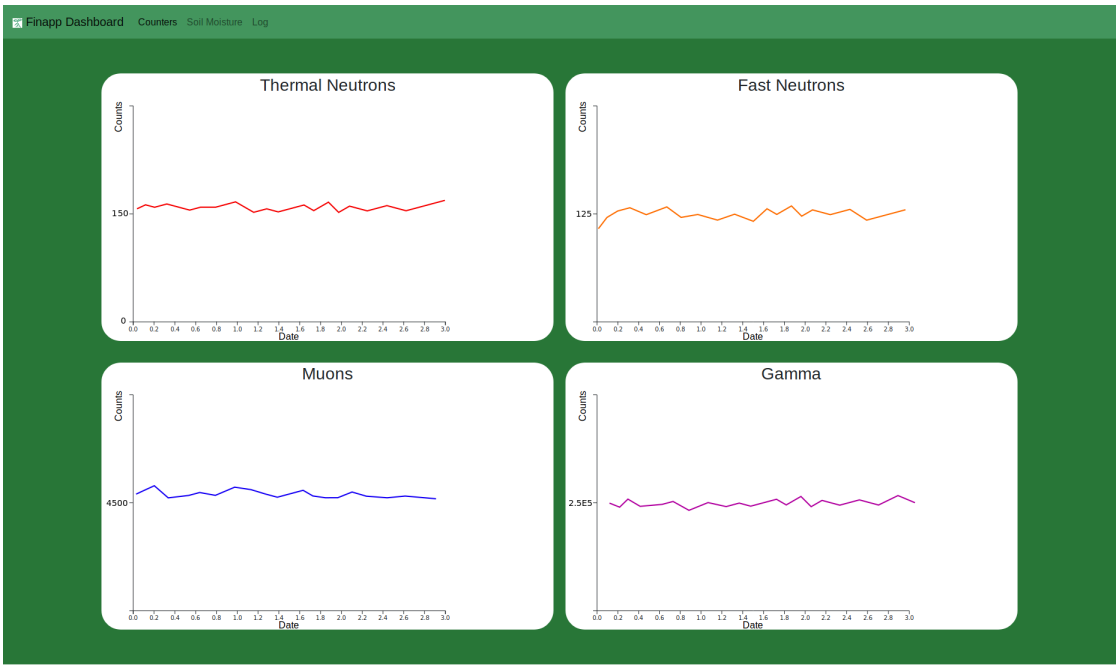

Figure A.8: Finapp dashboard showing particles counts. Each plot is updated online.

Bibliography

[Antcheva et al., 2011] Antcheva, I., Ballintijn, M., Bellenot, B., Biskup, M., Brun, R., Buncic, N., Canal, P., Casadei, D., Couet, O., Fine, V., et al. (2011). Root—a c++ framework for petabyte data storage, statistical analysis and visualization. *Computer Physics Communications*, 182(6):1384–1385.

[Arnó, 2013] Arnó, J. (2013). Escolà a., vallès jm, llorens j., sanz r., masip j., palacín j., rosell-polo jr leaf area index estimation in vineyards using a ground-based lidar scanner. *Precis. Agric*, 14:290–306.

[Baldoncini et al., 2019] Baldoncini, M., Albéri, M., Bottardi, C., Chiarelli, E., Raptis, K. G. C., Strati, V., and Mantovani, F. (2019). Biomass water content effect on soil moisture assessment via proximal gamma-ray spectroscopy. *Geoderma*, 335:69–77.

[Blasi, 2013] Blasi, P. (2013). The origin of galactic cosmic rays. *The Astronomy and Astrophysics Review*, 21(1):70.

[Blasi, 2014] Blasi, P. (2014). Recent results in cosmic ray physics and their interpretation. *Brazilian Journal of Physics*, 44(5):426–440.

[Bogena et al., 2015] Bogena, H. R., Huisman, J. A., Güntner, A., Hübner, C., Kusche, J., Jonard, F., Vey, S., and Vereecken, H. (2015). Emerging methods for noninvasive sensing of soil moisture dynamics from field to catchment scale: A review. *Wiley Interdisciplinary Reviews: Water*, 2(6):635–647.

[Brocca et al., 2017] Brocca, L., Ciabatta, L., Massari, C., Camici, S., and Tarpanelli, A. (2017). Soil moisture for hydrological applications: open questions and new opportunities. *Water*, 9(2):140.

[Cester et al., 2016] Cester, D., Lunardon, M., Moretto, S., Nebbia, G., Pino, F., Sajo-Bohus, L., Stevanato, L., Bonesso, I., and Turato, F. (2016). A novel detector assembly for detecting thermal neutrons, fast neutrons and gamma rays. *Nuclear Instruments and Methods in Physics Research Section A: Accelerators, Spectrometers, Detectors and Associated Equipment*, 830:191–196.

[Cester et al., 2014] Cester, D., Nebbia, G., Stevanato, L., Pino, F., and Viesti, G. (2014). Experimental tests of the new plastic scintillator with pulse shape discrimination capabilities ej-299-33. *Nuclear Instruments and Methods in Physics Research Section A: Accelerators, Spectrometers, Detectors and Associated Equipment*, 735:202–206.

[De Mendonça et al., 2016] De Mendonça, R., Braga, C., Echer, E., Dal Lago, A., Munakata, K., Kuwabara, T., Kozai, M., Kato, C., Rockenbach, M., Schuch, N., et al. (2016). The temperature effect in secondary cosmic rays (muons) observed at the ground: analysis of the global muon detector network data. *The Astrophysical Journal*, 830(2):88.

[Desilets et al., 2010] Desilets, D., Zreda, M., and Ferré, T. P. (2010). Nature's neutron probe: Land surface hydrology at an elusive scale with cosmic rays. *Water Resources Research*, 46(11).

[Dorman and Dorman, 2014] Dorman, I. and Dorman, L. (2014). How cosmic rays were discovered and why they received this misnomer. *Advances in Space Research*, 53(10):1388–1404.

[Entekhabi et al., 2004] Entekhabi, D., Njoku, E. G., Houser, P., Spencer, M., Doiron, T., Kim, Y., Smith, J., Girard, R., Belair, S., Crow, W., et al. (2004). The hydrosphere state (hydros) satellite mission: An earth system pathfinder for global mapping of soil moisture and land freeze/thaw. *IEEE Transactions on Geoscience and Remote Sensing*, 42(10):2184–2195.

[Famiglietti et al., 2008] Famiglietti, J. S., Ryu, D., Berg, A. A., Rodell, M., and Jackson, T. J. (2008). Field observations of soil moisture variability across scales. *Water Resources Research*, 44(1).

[Fontana et al., 2018] Fontana, C. L., Carnera, A., Lunardon, M., Pino, F. E., Sada, C., Soramel, F., Stevanato, L., and Moretto, S. (2018). A distributed data acquisition system for nuclear detectors. In *International Journal of Modern Physics: Conference Series*, volume 48, page 1860118. World Scientific.

[Franz et al., 2012] Franz, T. E., Zreda, M., Ferre, T., Rosolem, R., Zweck, C., Stillman, S., Zeng, X., and Shuttleworth, W. J. (2012). Measurement depth of the cosmic ray soil moisture probe affected by hydrogen from various sources. *Water Resources Research*, 48(8).

[Ghosh, 2014] Ghosh, S. (2014). *Distributed systems: an algorithmic approach*. Chapman and Hall/CRC.

[Hamamatsu, 2007] Hamamatsu (2007). *Photomultipliers tubes: basic and applications.* Hamamatsu.

[Hansen et al., 2003] Hansen, P., Carlson, P., Mocchiutti, E., Sciutto, S., and Boezio, M. (2003). Flux of atmospheric muons: Comparison between aires simulations and caprice98 data. *Physical Review D*, 68(10):103001.

[Harris and Stonard, 2018] Harris, N. R. and Stonard, A. (2018). A printed capacitance sensor for soil moisture measurement. In *Multidisciplinary Digital Publishing Institute Proceedings*, volume 2, page 705.

[Hillel, 1998] Hillel, D. (1998). *Environmental soil physics: Fundamentals, applications, and environmental considerations.* Elsevier.

[Hintjens, 2013] Hintjens, P. (2013). *ZeroMQ: messaging for many applications.* " O'Reilly Media, Inc.".

[Jakobi et al., 2018] Jakobi, J., Huisman, J., Vereecken, H., Diekkrüger, B., and Bogena, H. (2018). Cosmic ray neutron sensing for simultaneous soil water content and biomass quantification in drought conditions. *Water Resources Research*, 54(10):7383–7402.

[Knoll, 2010] Knoll, G. F. (2010). *Radiation detection and measurement.* John Wiley & Sons.

[Köhli et al., 2018] Köhli, M., Schrön, M., Zacharias, S., and Schmidt, U. (2018). Uranos-the cosmic ray neutron monte-carlo tool. In *EGU General Assembly Conference Abstracts*, volume 20, page 5394.

[Köhli et al., 2015] Köhli, M., Schrön, M., Zreda, M., Schmidt, U., Dietrich, P., and Zacharias, S. (2015). Footprint characteristics revised for field-scale soil moisture monitoring with cosmic-ray neutrons. *Water Resources Research*, 51(7):5772–5790.

[Kouzes, 2009] Kouzes, R. T. (2009). The 3he supply problem. Technical report, Pacific Northwest National Lab.(PNNL), Richland, WA (United States).

[Krüger et al., 2008] Krüger, H., Moraal, H., Bieber, J., Clem, J., Evenson, P., Pyle, K., Duldig, M., and Humble, J. (2008). A calibration neutron monitor: Energy response and instrumental temperature sensitivity. *Journal of Geophysical Research: Space Physics*, 113(A8).

[Lee and Ehsani, 2009] Lee, K. and Ehsani, R. (2009). A laser scanner based measurement system for quantification of citrus tree geometric characteristics. *Applied Engineering in Agriculture*, 25(5):777–788.

[Longair, 2011] Longair, M. S. (2011). *High energy astrophysics.* Cambridge university press.

[Marinello et al., 2017] Marinello, F., Pezzuolo, A., Meggio, F., Martínez-Casasnovas, J. A., Yezekyan, T., and Sartori, L. (2017). Application of the kinect sensor for three dimensional characterization of vine canopy. *Advances in Animal Biosciences*, 8(2):525–529.

[Marinello et al., 2014] Marinello, F., Schiavuta, P., Cavalli, R., Pezzuolo, A., Carmignato, S., and Savio, E. (2014). Critical factors in cantilever near-field scanning optical microscopy. *IEEE Sensors Journal*, 14(9):3236–3244.

[Morháč and Matoušek, 2008] Morháč, M. and Matoušek, V. (2008). Peak clipping algorithms for background estimation in spectroscopic data. *Applied spectroscopy*, 62(1):91–106.

[Noborio, 2001] Noborio, K. (2001). Measurement of soil water content and electrical conductivity by time domain reflectometry: a review. *Computers and electronics in agriculture*, 31(3):213–237.

[Nuske et al., 2014] Nuske, S., Gupta, K., Narasimhan, S., and Singh, S. (2014). Modeling and calibrating visual yield estimates in vineyards. In *Field and Service Robotics*, pages 343–356. Springer.

[Pajares et al., 2013] Pajares, G., Peruzzi, A., and Gonzalez-de Santos, P. (2013). Sensors in agriculture and forestry.

[Palleja and Landers, 2017] Palleja, T. and Landers, A. J. (2017). Real time canopy density validation using ultrasonic envelope signals and point quadrat analysis. *Computers and electronics in agriculture*, 134:43–50.

[Paschalis et al., 2013] Paschalis, P., Mavromichalaki, H., Yanke, V., Belov, A., Eroshenko, E., Gerontidou, M., and Koutroumpi, I. (2013). Online application for the barometric coefficient calculation of the nmdb stations. *New Astronomy*, 19:10–18.

[Petropoulos, 2013] Petropoulos, G. P. (2013). *Remote sensing of energy fluxes and soil moisture content*. CRC Press.

[Petropoulos et al., 2015] Petropoulos, G. P., Ireland, G., and Barrett, B. (2015). Surface soil moisture retrievals from remote sensing: Current status, products & future trends. *Physics and Chemistry of the Earth, Parts A/B/C*, 83:36–56.

[Pino et al., 2015] Pino, F., Stevanato, L., Cester, D., Nebbia, G., Sajo-Bohus, L., and Viesti, G. (2015). Study of the thermal neutron detector zns (ag)/lif response using digital pulse processing. *Journal of Instrumentation*, 10(08):T08005.

[Rai, 2013] Rai, R. (2013). *Socket. IO Real-time Web Application Development*. Packt Publishing Ltd.

[Reginato and Van Bavel, 1964] Reginato, R. and Van Bavel, C. (1964). Soil water measurement with gamma attenuation 1. *Soil Science Society of America Journal*, 28(6):721–724.

[Robinson et al., 2008] Robinson, D., Campbell, C., Hopmans, J., Hornbuckle, B. K., Jones, S. B., Knight, R., Ogden, F., Selker, J., and Wendroth, O. (2008). Soil moisture measurement for ecological and hydrological watershed-scale observatories: A review. *Vadose Zone Journal*, 7(1):358–389.

[Rosell and Sanz, 2012] Rosell, J. and Sanz, R. (2012). A review of methods and applications of the geometric characterization of tree crops in agricultural activities. *Computers and electronics in agriculture*, 81:124–141.

[Rosolem et al., 2013] Rosolem, R., Shuttleworth, W. J., Zreda, M., Franz, T., Zeng, X., and Kurc, S. (2013). The effect of atmospheric water vapor on neutron count in the cosmic-ray soil moisture observing system. *Journal of Hydrometeorology*, 14(5):1659–1671.

[Rufat et al., 2014] Rufat, J., Villar, J. M., Pascual, M., Falguera, V., and Arbonés, A. (2014). Productive and vegetative response to different irrigation and fertilization strategies of an arbequina olive orchard grown under super-intensive conditions. *Agricultural Water Management*, 144:33–41.

[Sato and Niita, 2006] Sato, T. and Niita, K. (2006). Analytical functions to predict cosmic-ray neutron spectra in the atmosphere. *Radiation research*, 166(3):544–555.

[Schrön, 2017] Schrön, M. (2017). Cosmic-ray neutron sensing and its applications to soil and land surface hydrology.

[Schrön et al., 2018] Schrön, M., Zacharias, S., Womack, G., Köhli, M., Desilets, D., Oswald, S. E., Bumberger, J., Mollenhauer, H., Kögler, S., Remmler, P., et al. (2018). Intercomparison of cosmic-ray neutron sensors and water balance monitoring in an urban environment. *Geoscientific Instrumentation, Methods and Data Systems*, 7(1):83–99.

[Seneviratne et al., 2010] Seneviratne, S. I., Corti, T., Davin, E. L., Hirschi, M., Jaeger, E. B., Lehner, I., Orlowsky, B., and Teuling, A. J. (2010). Investigating soil moisture–climate interactions in a changing climate: A review. *Earth-Science Reviews*, 99(3-4):125–161.

[Steigies, 2009] Steigies, C. T. (2009). Nmdb: towards a global neutron monitor database. In *AGU Fall Meeting Abstracts*.

[Stevanato et al., 2019] Stevanato, L., Baroni, G., Cohen, Y., Cristiano Lino, F., Gatto, S., Lunardon, M., Marinello, F., Moretto, S., and Morselli, L. (2019). A novel cosmic-ray neutron sensor for soil moisture estimation over large areas. *Agriculture*, 9(9):202.

[Stevanato et al., 2011] Stevanato, L., Fabris, D., Hao, X., Lunardon, M., Moretto, S., Nebbia, G., Pesente, S., Sajo-Bohus, L., and Viesti, G. (2011). Light output of ej228 scintillation neutron detectors. *Applied Radiation and Isotopes*, 69(2):369–372.

[Strati et al., 2018] Strati, V., Albéri, M., Anconelli, S., Baldoncini, M., Bittelli, M., Bottardi, C., Chiarelli, E., Fabbri, B., Guidi, V., Raptis, K., et al. (2018). Modelling soil water content in a tomato field: proximal gamma ray spectroscopy and soil–crop system models. *Agriculture*, 8(4):60.

[Su and Zhang, 2010] Su, X. and Zhang, Q. (2010). Dynamic 3-d shape measurement method: a review. *Optics and Lasers in Engineering*, 48(2):191–204.

[Tian et al., 2016] Tian, Z., Li, Z., Liu, G., Li, B., and Ren, T. (2016). Soil water content determination with cosmic-ray neutron sensor: Correcting aboveground hydrogen effects with thermal/fast neutron ratio. *Journal of Hydrology*, 540:923–933.

[Verstraeten et al., 2008] Verstraeten, W., Veroustraete, F., and Feyen, J. (2008). Assessment of evapotranspiration and soil moisture content across different scales of observation. *Sensors*, 8(1):70–117.

[Western et al., 2002] Western, A. W., Grayson, R. B., and Blöschl, G. (2002). Scaling of soil moisture: A hydrologic perspective. *Annual review of earth and planetary sciences*, 30(1):149–180.

[Zhuo and Han, 2016] Zhuo, L. and Han, D. (2016). The relevance of soil moisture by remote sensing and hydrological modelling. *Procedia Engineering*, 154:1368–1375.

[Zreda et al., 2008] Zreda, M., Desilets, D., Ferré, T., and Scott, R. L. (2008). Measuring soil moisture content non-invasively at intermediate spatial scale using cosmic-ray neutrons. *Geophysical research letters*, 35(21).

[Zreda et al., 2012] Zreda, M., Shuttleworth, W., Zeng, X., Zweck, C., Desilets, D., Franz, T., and Rosolem, R. (2012). Cosmos: The cosmic-ray soil moisture observing system. *Hydrology and Earth System Sciences*, 16(11):4079–4099.